NASA Contractor Report 4115

Numerical Simulation of Axisymmetric Turbulent Flow in Combustors and Diffusers

Chain Nan Yung

NASA

NASA Contractor Report 4115

Numerical Simulation of Axisymmetric Turbulent Flow in Combustors and Diffusers

Chain Nan Yung
University of Toledo
Toledo, Ohio

NASA

National Aeronautics
and Space Administration

Scientific and Technical
Information Division

1988

ACKNOWLEDGEMENT

I wish to express my deepest gratitute to my
co-advisors, Drs. K. J. De Witt and T. G. Keith, for their
support, advice and encouragement. They were always
patient and optimistic about the research. It has been a
pleasure working under their guidance. Thanks are also due
to Dr. D. R. Jeng for the benefits I received from him
during the course of my study.

CONTENTS

NOMENCLATURE

Symbols

a	coefficient for the inlet turbulence kinetic energy, Eq. (2-40)
A_E A_W A_N A_S	coefficients in the general finite difference equations, Eq. (5-5)
C_e C_w C_n C_s	convective coefficients in the finite difference expressions, Eq. (5-3)
C_p	pressure recovery coefficient
C_1 C_2 C_μ	constants in the turbulence model equations
D	inlet diameter
D_e D_w D_n D_s	diffusive coefficients in the finite difference expressions, Eq. (5-4)
D^u D^v	coefficients in the finite difference momentum equations, Eq. (5-14)
E	roughness parameter in the log law
F_ξ F_η	convective terms normal to control volume boundaries
G	rate of production of the turbulence kinetic energy
g	flux through zonal boundary
J	Jacobian of the transformation
k	turbulence kinetic energy
$\vec{k}$	unit normal perpendicular to the (ξ, η) plane
l	turbulence length scale
m	swirl intensity
m_p	mass source of a control volume
$\vec{n}_\xi$ $\vec{n}_\eta$	unit vector normal to a constant ξ line and a constant η line
P p	instantaneous and mean pressure
p'	corrective vaule of p, Eq (5-10), or pressure

vii

	fluctuation, Eq (2-15)
Pe	Peclet number
Q R	source terms in grid generation equations
Re	Reynolds Number
r	position vector of a point on the coordinate line
S_ϕ	volumetric source term of the general variable
s	arc length along a line
t t_o	time and time interval
U_i u_i u_i'	tensor notation of the instantaneous velocity, mean velocity and fluctuating velocity
u, v, w	velocity components in x, r, θ directions
u_{in}	average inlet velocity
u^*	friction velocity
V_p	velocity at point p
x r θ	cylindrical coordinates
x y	two dimensional coordinates
x_i	tensor notation of the coordinate
y_p	distance from the wall to point p
y_p^+	dimensionless distance from the wall to point p

Greek Letters

α β γ	coordinate transformation parameters
δ	Kronecker function
ε	turbulence energy dissipation
κ	Von Karman constant in the log law
λ	coefficient in Eq (2-41)
μ μ_t μ_{eff}	molecular, turbulent and effective viscosity
μ'	viscosity fluctuation

ξ η	curvilinear coordinates
ρ	density
Γ_ϕ	effective diffusivity for general variable
σ_k σ_ε	effective Prandtl number for turbulence kinetic energy and dissipation energy
τ_{ij} σ_{ij}	tensor notation of the shear stress
τ_w	shear stress on the wall
Φ ϕ ϕ'	general dependent variable: instantaneous value, mean value and fluctuating value
χ ψ	grid spacing control parameters

Subscripts

E W N S	east, west, north and south grid point
e w n s	east, west, north and south boundary of a control volume
p	center grid point
ϕ	general dependent variable

Superscripts

c	coarse grid
f	fine grid
p	pressure
u	u velocity component
v	v velocity component
—	average value
*	preliminary value
'	corrective value

CHAPTER 1

INTRODUCTION

1-1 Motivation and Purpose of Research

Turbulent recirculating flows occur in many engineering and industrial applications. For example, such flows are found in hydraulic channels, power plant furnaces and in gas turbine engine combustors. To improve performance in such applications, an accurate description of the flow patterns are required. Because it is both difficult and costly to make detailed flow measurements under real operating conditions, numerical simulation becomes an extremely valuable tool for visualizing the flow. Basically, the simulation is required to solve the time averaged Navier-Stokes equations along with a turbulence model equation or equations for the detailed patterns of the flow.

Over the years, numerical computation of turbulent recirculating flows has been an active research subject. Significant development has taken placed since the introduction of the turbulence k-ε model [1] in 1974. The solution procedure [2] has steadily evolved and now uses the finite volume approach to discretize the differential equations and employs the SIMPLE algorithm to solve for the velocities and the pressure. Recently, efforts have been principally directed towards improving the accuracy and efficiency of

the computation.

The finite volume approach requires that a proper finite difference operator be available to represent the convection transport terms. This operation is necessary in order to prevent oscillatory solutions. It has been found that implementation of one-sided (upwind) differencing will generally give stable solutions. However, it is also realized that this scheme augments the diffusive effect in the crossflow direction and reduces the numerical accuracy of the results. Finite difference methods that have been developed for the purpose of suppressing the diffusion error include the skew upwind scheme [3], the quadratic upwind scheme [4], and other higher order methods [5]. These higher order schemes, while very promising, are in many cases controversial because they produce questionable resuls, particularly for complex flows.

Until a few years ago, most turbulent flow studies dealt with flow in regular shaped geometries in which the boundaries coincided with the coordinate lines of either a Cartesian or cylindrical coordinate system. For irregularly shaped flow domains, since mesh points may not fall on the boundaries, a relatively large amount of computation in the form of interpolation was required.

Numerical grid generation has been developed to tackle flow problems in irregular geometries. By this technique, a grid system is numerically generated which permits the governing equations to be computed on a uniform mesh without

2

using interpolation for the boundary points. When the grid is generatd by locating points along the boundary surfaces, it is termed a body-fitted coordinate procedure.

Applications of the body-fitted coordinate transformation to turbulent flow problems have appeared in the recent literature. But comparison between predicted results and measured values is still quite limited. In addition, many factors, such as the differencing method and the grid distribution, both of which have a vital effect on the numerical solutions of complex flows, have not been thoroughly investigated. Thus, one objective of the present research was to develop and test various numerical methods for calculating the properties of turbulent flows in irregular geometries.

Grid generation does help to simplify problems having arbitrarily shaped boundaries. It is obvious that as the geometry becomes more complex, the grid generation also becomes a tougher task. Construction of a single grid system that covers the entire flowfield would be very difficult for complicated flows such as the flow passing over an aircraft or through a gas turbine combustor with several passages. In such cases, a better approach would be to divide the field into several subregions and generate an independent grid for each subregion. Grid generation would therefore be a much easier process. This method has been referred to as a zonal approach or a grid patching technique and is gradually attracting attention in computational fluid

3

dynamics pursuits. With the zonal approach, the grid in some regions can be refined to obtain better quality solutions without affecting the calculation in other regions. Moreover, this approach permits the use of different computational methods more suited to each of the zones.

Application of the zonal approach has been implemented in Euler equation calculations, but has not yet been reported for turbulent flows. Recently, Shyy [7] underscored the need for using zonal grid methods in turbulent flow computations. Shyy simulated turbulent flow in an annular dump diffuser. He found that a single grid system, generated over the whole domain, caused the grid density in the annular tube to be much larger than that in the dump region. Moreover, he experienced difficulty in refining the grid in wall regions. This problem could be alleviated using a zonal grid approach that divides the dump diffuser into two regions: a dump region with a fine mesh and an annular region with a coarse grid.

The division of a given field into subregions introduces grid boundaries in the calculation domain. Since either grid lines or transformation metrics may not be continuous at the interface of any two zones, care must be exercised in treating interface points in order to transfer information accurately. In fact, proper zonal boundary treatment is a key ingredient for successful application of this technique.

4

1-2 Previous Work

There have been several attempts to solve turbulent flow problems by using coordinate transformation and grid generation. A diffuser flow was analyzed by Pope [8]. He presented the transport equations in an orthogonal coordinate system. However, the dependent variables were maintained in their Cartesian coordinate form rather than expressing them in the contravariant form of curvilinear coordinates. This representation enabled the formulation to be cast into a strong conservation form. Since no additional terms arose due to stretching the coordinates, the same solution procedure as used in Cartesian coordinates could be employed.

Demirdzic et al. [9] used a different approach in which the equations were expressed in a general form with contravariant velocities and the metric tensors of the coordinates. This presentaion had more flexibility in handling the boundary conditions. However, the transformed equations became lengthy and complicated due to the appearance of curvature source terms. Also, the formulation was found to be non-conservative, i.e., was not written in divergence form. The flow in a reciprocating internal combustor engine was studied, but the results were only explained qualitatively.

Quantitative analyses of turbulent flow with various swirl conditions in diffusers were carried out by Habib and Whitelaw [10] and by Hah [11]. Habib and Whitelaw calculated the flow pattern and turbulence intensity for different configurations of wide angle diffusers. The momentum

5

equations and the k-e turbulence model equation were formulated in orthogonal coordinates, the same approach as used by Pope [8]. For non-swirling conditions, the predictions for the mean velocity compared very well with experimental measurements, but predictions of the turbulence kinetic energy were not in good agreement. The results for swirling flows were not as accurately predicted as in non-swirling flows. Both mean velocity and turbulence energy were underestimated and the size of the central recirculation bubble was overpredicted.

Hah [11] investigated the flowfield in small angle diffusers. The equations were expressed in the same manner as Demirdzic et al. [9], i.e., in general curvilinear coordinates. The turbulent properties were simulated by the algebraic Reynolds stress model with corrections on the coefficients to account for the effect of streamline curvature. In addition to the hybrid scheme, Hah used the quadratic upwind scheme and the skew upwind scheme to test for numerical diffusion. Comparing predictions with measurements, Hah concluded that only the quadratic upwind and the skew upwind schemes could give reliable predictions. The hybrid scheme generated excessive numerical diffusion and underpredictd the central bubble size by almost 30%.

Shyy and Correa [12] studied the impact of numerical schemes and grid systems on the solution accuracy and stability. They used different methods, including first order upwind, second order upwind, skew upwind, quadratic upwind,

and central difference schemes, to interpolate the convective terms in simple advection problems. The results indicated that the hybrid method had a large spreading rate in the crossflow direction and induced substantial errors in the solution. For other schemes, the accuracy was dependent upon the particular problems studied and upon the form of the boundary conditions. Calculations were also presented for turbulent flow in a two-dimensional gas turbine combustor. The influences of grid distribution and the differencing method on results were demonstrated.

Syed et al., [5] and [6], investigated numerical diffusion in a variety of flow problems. They found that numerical accuracy was dependent upon the flow field and mesh placement. The flow angle also had an effect on the accuracy for a given computational scheme.

A further investigation of turbulent flow in a dump diffuser was conducted by Shyy [7]. He performed calculations on two levels of grid points and found that a coarse grid produced better agreement between the numerical predictions and the experimental data than did a fine mesh. Also, a lower order hybrid difference scheme produced better results than did higher order schemes.

In view of the published results, it may be concluded that consistent turbulent flow predictions are still far from routine. The influence of grid systems or computational methods remains unresolved and continues to be a worthwhile subject for exploration. One such area that has

not received much attention is the used of structured grids in which the flow field is partitioned into zones. Some zones may have a coarse grid while others a fine mesh structure. It is believed that this provides better ultization of the grid.

The idea of zonal grids is not new; however, it has not been applied to turbulent flows. Hessenius & Pulliam [13] applied the zonal grid method to the solution of Euler equations. Their results stressed the need of a conservative treatment at the zone interface. Rai, [14] and [15], later developed a conservative zonal boundary scheme using integration and interpolation methods to update the values of grid points at the zonal interface. The scheme was applied to Euler equation calculations for the case of supersonic flow over a cylinder, blast wave diffraction by a ramp and one dimensional shock-tube flow. Atta and Vadyak [16] solved a three dimensional potential flow over an isolated wing and a noninteracting wing/pylon/nacele configuration. They generated an overlapped grid region and let the flow-field information be transfered through this region. An interpolation technique was employed to approximate the zonal boundary values.

Transonic flow over an airfoil was analyzed by Berger and Jameson [17]. Instead of grid patching, they used an automatic adaptive grid refinement method. The residual at any control volume was monitored after each iteration. If the residual was found to be large, grid refinement was

8

imposed on that control volume and the control volume was divided into four smaller cells. This procedure created an interface between the fine grid and the coarse grid. Berger and Jameson studied a number of methods for treating the interface and concluded that a conservation approach that involved an interpolation for the value at the cell center and the summation/integration for the flux at the cell boundaries represented the best choice of the methods investigated. They also found that when a non-conservation form was used for the interfacial treatment, the predicted drag coefficient differed by as much as 20% from the value found by using a conservation approach.

1-3 Outline Of The Thesis

This study is aimed at the development and verification of numerical methods which include a zonal grid approach for turbulent flow computations in combustor geometries. The effort is to be accomplished by solving a set of non-linear partial differential equations which include the continuity, momentum, and turbulence equations in a general curvilinear coordinate system for both a single grid and a zonal or partitioned grid.

In the next chapter the formulation of the governing equations together with their boundary conditions is presented. A short discussion of turbulence models is also included. Chapters 3 to 6 are devoted to the solution method for the flowfield calculation. Chapter 3 presents

the method of grid generation while the transformation of the governing equations and the boundary conditions is discussed in Chapter 4. The computational procedure will be depicted in chapter 5. The finite volume approach and the SIMPLE algorithm are used to facilitate the pressure computation. Chapter 6 deals with zonal grid boundary treatment. The proposed method contains the generation of an overlap region between two grid zones and an interface operator that permits numerical information to be transferred accurately while preserving the conservation principle. The presentation of the results of the computation for both single grid and zoned grid systems is given in Chapter 7. Results were compared against experimental measurements. Finally, the conclusions of this study and recommendations for further work are discussed in Chapter 8.

CHAPTER 2

GOVERNING EQUATIONS AND TURBULENCE MODEL

2-1 Time Averaged Continuity and Momentum Equations

The partial differential equations governing instantaneous turbulent flow are given in general Cartesian form as:

Continuity $\quad \dfrac{\partial \rho}{\partial t} + \dfrac{\partial}{\partial x_i} \rho U_i = 0$ $\hspace{3cm}$ (2-1)

Momentum $\quad \dfrac{\partial}{\partial t} \rho U_j + \dfrac{\partial}{\partial x_i} \rho U_i U_j = - \dfrac{\partial}{\partial x_i} \Gamma_{ij}$ $\hspace{1.5cm}$ (2-2)

where $\quad \Gamma_{ij} = P\delta_{ij} - \mu \left(\dfrac{\partial U_i}{\partial x_j} + \dfrac{\partial U_j}{\partial x_i} \right) + \dfrac{2}{3} \mu \dfrac{\partial U_1}{\partial x_1} \delta_{ij}$ $\hspace{0.5cm}$ (2-3)

and δ_{ij} is the Kronecker function, which equals 0 for $i \neq j$, and 1 for $i = j$.

Due to the very small scale of turbulent motion and its rapid movement, direct simulation of the above equations would require an enormous amount of computer time and storage, and is, more than likely, not possible. A turbulent flow property, Φ, can be identified in terms of its mean component, ϕ, and its fluctuating component, ϕ'. This is known as Reynolds decomposition and is written as:

11

$$\phi = \phi + \phi' \tag{2-4}$$

where
$$\phi = \frac{1}{t_0} \int_0^{t_0} \phi \, dt \tag{2-5}$$

In this expression, t_0 is a time interval which is large when compared to the time of the turbulent oscillations. The introduction of Reynolds decomposition allows the governing equations to be expressed in the more desirable time-averaged form where the variables appear as mean values instead of as instantaneous values. For an incompressible flow, the time-averaged equations of continuity and momentum take the form:

Continuity
$$\frac{\partial}{\partial x_i} \rho u_i = 0 \tag{2-6}$$

Momentum
$$\frac{\partial}{\partial x_i} \rho u_i u_j = -\frac{\partial}{\partial x_i} \sigma_{ij} - \frac{\partial}{\partial x_i} \overline{\rho u_i' u_j'} \tag{2-7}$$

where
$$\sigma_{ij} = p\delta_{ij} - \mu \left(\frac{\partial u_i}{\partial x_j} + \frac{\partial u_j}{\partial x_i}\right) + \frac{2}{3} \mu \frac{\partial u_1}{\partial x_1} \delta_{ij}$$

$$- \overline{\mu'\left(\frac{\partial u_i'}{\partial x_j} + \frac{\partial u_j'}{\partial x_i}\right)} + \frac{2}{3} \overline{\mu' \frac{\partial u_1'}{\partial x_1}} \delta_{ij} \tag{2-8}$$

Neglecting the fluctuations in the laminar viscosity, i.e., terms containing μ', the expression for σ_{ij} has the same

12

form as Γ_{ij} in Equation (2-3), but with all the variables time-averaged.

The process of time averaging produces additional terms, $\overline{u_i' u_j'}$, in the momentum equations. These terms, called the Reynolds stresses or the turbulent stresses, represent the additional·momentum transport due to turbulent motion. Equations (2-6) and (2-7) can be solved for mean values of velocity only when the Reynolds stresses are known. This is called the closure problem. Many articles have been written in which the Reynolds stresses have been modeled in terms of known quantities or mean flow values. The suggested models range from simple algebraic expressions to sophisticated partial differential equations. They not only give mathematical expressions to calculate the stresses but also provide physical information about the turbulence. However, the more information the model contains, the more complex it becomes. Because the choice of the model is vital to the resulting predictions, a brief review of turbulence models will be presented in the following section.

2-2 Turbulence Models

2-2-1 Preview
Basically, turbulence models can be divided into two catagories according to whether the Reynolds stresses are derived from an eddy viscosity concept or determined from the transport equations for the stresses themselves.

The eddy viscosity concept was introduced by Boussinesq [18] in 1877. He assumed, in analogy to molecular viscosity for laminar flow, that the turbulent stresses are proportional to the mean velocity gradient. The proportionality constant is termed the eddy viscosity μ. A general form of this concept may be expressed as:

$$- \overline{\rho u_i' u_j'} = \mu_t \left(\frac{\partial u_i}{\partial x_j} + \frac{\partial u_j}{\partial x_i} \right) - \frac{2}{3} \rho k \delta_{ij} \qquad (2-9)$$

where k is the normal stress or the turbulence kinetic energy defined by:

$$k = \frac{1}{2} \overline{u_i' u_i'} \qquad (2-10)$$

The turbulence normal stresses act like pressure, so when Equation (2-9) is used to eliminate $\overline{u_i' u_j'}$ in the momentum equations, the normal stresses can be absorbed into the pressure term and need not be calculated explicitly.

Boussinesq's concept, however, does not resolve the closure problem for there remains an unknown: the eddy viscosity. Eddy viscosity, unlike the molecular viscosity, is not a property of the fluid, but depends upon the flow conditions. It is a function of factors that influence the detailed patterns of turbulence and deviating velocities, and it is sensitive to the intensity and the length scale of

the turbulence. Molecular viscosity can be measured on an isolated sample of fluid; eddy viscosity can only be obtained by experiments on the flow itself or through calculations based on certain hypotheses. Consequently, turbulence modelling following this approach concentrates on determining the variation of viscosity.

The first important advance in the determination of eddy viscosity was Prandtl's mixing length theory [19]. The basis of this theory was that certain characteristics of a turbulent flow resembled those found in molecular interactions. Thus, he used the kinetic theory of gases as a model to describe local turbulent exchanges. He assumed that eddy viscosity, like molecular viscosity, was a function of density, length scale and velocity. However, Prandtl introduced a length scale he called the mixing length into the derivation for eddy viscosity. The mixing length parallels the mean free path for molecular viscosity and physically represents the distance a packet of fluid moves before giving up its momentum to the surrounding fluid. Further, he assumed that the turbulent velocity was a product of mixing length and mean velocity gradient. Accordingly, Prandtl obtained the following expression for the eddy viscosity:

$$\mu_t = \rho l^2 \left| \frac{\partial u}{\partial y} \right| \tag{2-11}$$

where l is the mixing length and $\frac{\partial u}{\partial y}$ is the mean flow veloc-

ity gradient. It has been found that the mixing length theory applies very well in turbulent shear flows which have a single length scale, but it is not suitable for most tru-bulent flows. Tennekes and Lumley [20] have presented a very critical examination of the mixing length theory. An obvious limitation occurs when attempting to calculate flow in the center of a pipe, where the velocity gradient is zero. At this location, mixing length theory gives a zero eddy viscosity. This is clearly incorrect because turbulent mixing does not vanish in this region of the flow.

To overcome the more obvious limitations with the mixing length theory, turbulence models were developed which account for the transport of turbulence quantities. These quantities can be determined from the solution of their corresponding partial differential equations.

In general, a turbulent field can be characterized by two parameters: turbulence intensity and the size or length scale of the turbulent eddies. Turbulence intensity is measured by the root mean square of fluctuating velocities and refers to the energy contained in an eddy. The length scale of an eddy is obtained from integration of velocity correlation functions. The equations for both quantities can be derived from the Navier-Stokes equations by making appropriate assumptions. The length scale equation, how-ever, can not be presented in a closed form and consquently can not be applied directly.

Examining the process affecting the length scale of

eddies suggests that the dissipation rate of turbulence energy is an important parameter in turbulent exchanges. The dissipation of energy destroys small eddies and thus effectively increases the average eddy size. From an energy balance of the rate of supply and dissipation over small scale eddies, the size of an eddy can be obtained as a function of turbulence energy and its dissipation rate; hence, [20],

$$l \sim \frac{k^{1.5}}{\varepsilon} \tag{2-12}$$

where ε is the dissipation rate of turbulence kinetic energy, defined by

$$\varepsilon = \frac{\mu}{\rho} \overline{\left(\frac{\partial u_i'}{\partial x_j}\right)^2} \tag{2-13}$$

Equation (2-12) effectively removes the length scale from the problem, replacing it with the dissipation rate. The latter has been found to be more readily estimated than is the former. A turbulence model based on the solution of the differential equations above for one or two quantities has been proposed by many researchers, e.g., Prandtl [53] and Rodi [54]. These models are now widely referred to as one or two equation models. The model in terms of both quantities, k and ε , developed by Harlow and Nakayama [23] and

Jones and Launder [24], has received broad recognition and is now commonly known as the k-ε model.

Another approach, which does not use the eddy viscosity concept, attempts to determine the Reynolds stresses from the solution of partial differential equations or from the solution of algebraic equations. The latter are obtained by modelling the convective and diffusive terms in the Reynolds stresses equations with an algebraic form, if the variation of the turbulence stresses are small across the flow. These methods, called Reynolds stress models or algebraic stress models have been reported by Launder et al. [25], Bradshaw et al. [26] and Rodi [55]. Reynolds stress models employ transport equations for the individual stresses. They are more elaborate than viscosity-based models. In some cases, e.g., [25], the Reynols stress models have shown better predictions than the more widely used k-ε model. However, due to the complexity of these models and the fact that they are computationally more expensive, the Reynolds stress models are thought to be less versatile than the k-ε model for most pratical applications.

2-2-2 Turbulence k-ε Model

The transport equations governing the turbulence properties, k and ε , can be obtained from the Navier-Stokes equation. To derive the kinetic energy equation, the Navier-Stokes equation is first multiplied by the instantaneous velocity U_i. The time average of all terms is then taken, and the

equation which governs the kinetic energy of the mean flow is subtracted. The resulting equation becomes

$$\frac{\partial}{\partial x_i} \rho u_i k = -\frac{\partial}{\partial x_i} [\overline{\rho u_i' (k+p')} - \mu \frac{\partial k}{\partial x_i}]$$

$$(I) \qquad\qquad\qquad (II)$$

$$- \overline{\rho u_i' u_j'} \frac{\partial u_i}{\partial x_j} - \mu \overline{(\frac{\partial u_i'}{\partial x_j})}^2 \qquad\qquad (2\text{-}14)$$

$$(III) \qquad\quad (IV)$$

The term labeled (I) is the rate of change of kinetic energy and is seen to be due to the turbulent transport term (II), the rate of turbulent production term (III) and the rate of dissipation term (IV). The turbulent transport term contains fluxes arising from velocity fluctuations and viscous action. Analogous to the handling of the diffusion transport, the flux due to the velocity fluctuation can be cast into the following form:

$$\overline{\rho u_i' (k+p')} = - \frac{\mu_t}{\sigma_k} \frac{\partial k}{\partial x_i} \qquad\qquad (2\text{-}15)$$

where σ_k is the Prandtl number of the turbulent kinetic energy. Making use of Equation (2-15), the final form of the kinetic energy equation is:

$$\frac{\partial}{\partial x_i} \rho u_i k = \frac{\partial}{\partial x_i} [(\frac{\mu_t}{\sigma_k} + \mu) \frac{\partial k}{\partial x_i}] - \overline{\rho u_i' u_j'} \frac{\partial u_i}{\partial x_j} + \mu \overline{(\frac{\partial u_i'}{\partial x_j})}^2 \quad (2\text{-}16)$$

19

or $\quad \dfrac{\partial}{\partial x_i} \rho u_i k = \dfrac{\partial}{\partial x_i} \mu_{eff} \dfrac{\partial k}{\partial x_i} + G - \rho \varepsilon$ $\qquad$ (2-17)

where μ_{eff} is the effective viscosity $= \mu + \dfrac{\mu_t}{\sigma_k}$ $\qquad$ (2-18)

G is the rate of production $= -\overline{\rho u_i' u_j'} \dfrac{\partial u_i}{\partial x_j}$ $\qquad$ (2-19)

and ε is the dissipation $= \dfrac{\mu}{\rho} \overline{\left(\dfrac{\partial u_i'}{\partial x_j}\right)^2}$ $\qquad$ (2-20)

Development of the equation for the dissipation of energy is tedious. To obtain the equation, the momentum equation is differentiated with respect to x_1 , then it is multiplied by $2\nu \dfrac{\partial u_j}{\partial x_j}$, and finally time averaged. The result of these operations may be written as follows [27]:

$$\dfrac{\partial}{\partial x_i} \rho \varepsilon u_i = 2\mu \overline{\dfrac{\partial u_i'}{\partial x_1} \dfrac{\partial u_j'}{\partial x_1} \dfrac{\partial u_i}{\partial x_j}} - 2\mu \overline{\dfrac{\partial u_i'}{\partial x_1} \dfrac{\partial u_i'}{\partial x_j} \dfrac{\partial u_j'}{\partial x_1}} - \dfrac{2\mu}{\rho}^2 \overline{\dfrac{\partial^2 u_i'}{\partial x_j^2} \dfrac{\partial^2 u_i'}{\partial x_1^2}}$$

$$- 2\mu \overline{u_j' \dfrac{\partial u_i'}{\partial x_1} \dfrac{\partial^2 u_i}{\partial x_j \partial x_1}} - 2\mu \overline{\dfrac{\partial u_1'}{\partial x_i} \dfrac{\partial u_j'}{\partial x_1} \dfrac{\partial u_i'}{\partial x_j}}$$

$$- \dfrac{\partial}{\partial x_i} [\rho \overline{u_i' \varepsilon'} + 2\mu \overline{\dfrac{\partial \rho'}{\partial x_1} \dfrac{\partial u_i'}{\partial x_1}} - \mu \dfrac{\partial \varepsilon}{\partial x_i}] \qquad (2\text{-}21)$$

To make this equation tractable, various assumptions must be

20

introduced. Generally, the first five terms on the right hand side of the equation are combined to represent the production term and the term in the last bracket is treated as the diffusion term. According to Launder and Spalding [1], the workable form of the dissipation equation is

$$\frac{\partial}{\partial x_i} \rho \varepsilon u_i = \frac{\partial}{\partial x_i} \frac{\mu_{eff}}{\sigma_\varepsilon} \frac{\partial \varepsilon}{\partial x_i} + \frac{\varepsilon}{k}(C_1 G - \rho C_2 \varepsilon) \qquad (2\text{-}22)$$

The eddy viscosity is then given by:

$$\mu_t = C_\mu \rho \frac{k^2}{\varepsilon} \qquad (2\text{-}23)$$

Equations (2-17), (2-22) and (2-23) constitute the k-ε model, which together with the continuity and momentum equations (Equation (2-6) and Equation (2-7)), form a closed set of equations describing turbulent flows.

The k-ε model contains five empirical constants. They are determined either from experiments or from computer optimization [21]. In grid turbulence, diffusion and production of kinetic energy and dissipation energy are negligible, so that C_2 is the only constant appearing in Equations (2-17) and (2-22). Therefore, C_2 can be determined from the measured rate of decay of kinetic energy behind a screen grid. The value of C_2 was found to lie in the range 1.8 to 2.0. The constant C_μ is determined from experiments

21

of shear layer flows. In such flows, the convective and diffusive transport of the kinetic energy are negligible. The production of kinetic energy is equal to the dissipation and the turbulence is in a state of local equilibrium. Equations (2-17) and (2-23) combine to give $C_\mu = (\overline{uv}/k)^2$. Measurement in this flow [26] yielded $\overline{uv}/k = 0.3$, so that $C_\mu = 0.09$. C_1 is determined from the following:

$$C_1 = C_2 - \frac{\kappa^2}{\sigma_\varepsilon \sqrt{C_\mu}} \qquad (2-24)$$

This equation is derived from the dissipation equation by considering the flow in the wall region, where the logarithmic velocity profile prevails and where convection of dissipation is negligible. The above relation fixes the value of the constant C_1 when the other constants have been chosen. The Prandtl numbers of the kinetic energy, σ_k, and the dissipation erergy, σ_ε, are assumed to be close to unity and they are adjusted by computer optimization. The following values are recommended by Launder and Spalding [1] based on extensive examination of free turbulent flows:

C_μ	C_1	C_2	σ_k	σ_ε
0.09	1.44	1.92	1.00	1.30

Although these constants are adequate for many flows, it has

22

been found that streamline curvature effects, which strongly influence turbulent transport in shear layers, are not described by the k-ε model with the above constants. A modification of the constants, therefore, has been introduced to achieve the inclusion of curvature effects, e.g., by Launder et al. [56] and by Leschziner and Rodi [57]. However, these corrections are of an ad hoc nature, and future research is required to provide a more rigorous framework for the incorporation of a curvature correction into the turbulence model.

2-2-3 Wall Function

In general, the k-ε model is valid for high Reynolds number flow. In the region close to the wall, viscous effects dominate and the turbulence model can not be expected to apply. There are two methods of treatment for the wall region in numerical computation: the wall function method and a low Reynolds number modelling method.

The wall function method assumes that, at a point P located a distance above the wall and outside the viscous sublayer (refer to Figure 1), the velocity vector is parallel to the wall and described by the logarithmic law of the wall. With this assumption, the wall boundary conditions, such as for the shear stress, are connected to the mean flow properties at the point P. The computation thus skips over the region of the laminar sublayer where, because of steep gradients in the dependent variables, a large number of grid

23

points are required.

The low Reynolds number model uses the original turbulence model as a basis and employs a damping effect and other functions on the viscosity and the turbulence equations to account for the variation of flowfield quantities near the wall. This method permits the calculation to extend to the solid wall, so that velocities and other quantities within the laminar sublayer can be described. A recent review of the performance of the low Reynolds number model was given by Patel et al. [28]. They examined the results of several boundary layer type flows and found none of these models could be used with confidence in the region near the wall.

In the present work, the flowfield in the main flow region is of principle concern. To avoid excessive grid points in the laminar sublayer, as mentioned above, the wall function method was adopted. The first grid point in the flow next to the wall is placed just outside the viscous layer. At that point, the resulting velocity, V_p, parallel to the wall, is given by

$$\frac{V_p}{u^*} = \frac{1}{\kappa} \ln E\, y_p^+ \qquad (2\text{-}25)$$

where u^* and y_p^+ are the friction velocity and the dimensionless wall distance defined, respectively, by:

24

$$u^* = \left(\frac{\tau_w}{\rho}\right)^{0.5} \tag{2-26}$$

$$y_p^+ = \frac{\rho y_p u^*}{\mu} \tag{2-27}$$

τ_w is the shear stress at the wall κ and E are the von-Karman constant and the roughness parameter, respectively, with the corresponding values of 0.4 and 9.7. Equation (2-25) is applied in the range of nondimensional wall distance, y_p^+, between 30 and 200, where the first grid point P must be located. This range lies between the viscous layer and the turbulent inner layer. In this range, advection and diffusion of $\overline{u_i' u_j'}$ are negligible and local equilibrium prevails. Under this condition, the turbulence energy equation for a two dimensional boundary layer situation reduces to

Production = Dissipation

or

$$\frac{\mu_t}{\rho}\left(\frac{\partial u}{\partial y}\right)^2 = \varepsilon \tag{2-28}$$

Equation (2-28), together with Equation (2-26), and the assumption that the shear stress at the point P is approximately equal to the wall shear stress, leads to

$$k = \frac{u^{*2}}{\sqrt{C_\mu}} \tag{2-29}$$

25

Additionally, substituting $\dfrac{\partial u}{\partial y}$ computed from the log law into Equation (2-28) will give the relation for ε:

$$\varepsilon = \frac{u^{*3}}{\kappa y} \qquad (2\text{-}30)$$

$$\text{or} \quad \varepsilon = \frac{C_\mu^{0.75} k^{1.5}}{\kappa y} \qquad (2\text{-}31)$$

Equations (2-29) and (2-31) give the values of k and ε at the point P without solving the transport equations.

2-3 Basic Equations For Steady, Incompressible, Axisymmetric, Turbulent Swirling Flow

The transport equations for the conservation of mass, momentum, turbulence energy, and dissipation have been presented above in general form. For the present study, the steady state equations for incompressible, axisymmetric, turbulent swirling flow may be written:

Continuity

$$\frac{\partial}{\partial x}\,\rho u + \frac{\partial}{r\partial r}\,\rho v r = 0 \qquad (2\text{-}32)$$

x-Momentum

$$\frac{\partial}{\partial x}\,\rho u u + \frac{\partial}{r\partial r}\,\rho v r u - \frac{\partial}{\partial x}\,\mu_{eff}\frac{\partial u}{\partial x} - \frac{\partial}{r\partial r}\,r\mu_{eff}\frac{\partial u}{\partial r}$$

26

$$= -\frac{\partial p}{\partial x} + \frac{\partial}{\partial x}\,\mu_{eff}\,\frac{\partial u}{\partial x} + \frac{\partial}{r\partial r}\,r\mu_{eff}\,\frac{\partial v}{\partial x} \qquad (2\text{-}33)$$

r-Momentum

$$\frac{\partial}{\partial x}\,\rho uv + \frac{\partial}{r\partial r}\,\rho vrv - \frac{\partial}{\partial x}\,\mu_{eff}\,\frac{\partial v}{\partial x} - \frac{\partial}{r\partial r}\,r\mu_{eff}\,\frac{\partial v}{\partial r}$$

$$= -\frac{\partial p}{\partial x} + \frac{\partial}{\partial x}\,\mu_{eff}\,\frac{\partial u}{\partial r} + \frac{\partial}{r\partial r}\,r\mu_{eff}\,\frac{\partial v}{\partial r} + \frac{\rho w^2}{2} - \frac{2\mu v}{r^2} \qquad (2\text{-}34)$$

θ-Momentum

$$\frac{\partial}{\partial x}\,\rho uw + \frac{\partial}{r\partial r}\,\rho vrw - \frac{\partial}{\partial x}\,\mu_{eff}\,\frac{\partial w}{\partial x} - \frac{\partial}{r\partial r}\,r\mu_{eff}\,\frac{\partial w}{\partial r}$$

$$= -\frac{\rho vw}{r} - \frac{w}{r^2}\,\frac{\partial}{\partial r}\,r\mu_{eff} \qquad (2\text{-}35)$$

Turbulence energy

$$\frac{\partial}{\partial x}\,\rho uk + \frac{\partial}{r\partial r}\,\rho vrk - \frac{\partial}{\partial x}\,\frac{\mu_{eff}}{\sigma_k}\,\frac{\partial k}{\partial x} - \frac{\partial}{r\partial r}\,r\,\frac{\mu_{eff}}{\sigma_k}\,\frac{\partial k}{\partial r}$$

$$= G - \rho\epsilon \qquad (2\text{-}36)$$

Dissipation energy

$$\frac{\partial}{\partial x}\,\rho u\epsilon + \frac{\partial}{r\partial r}\,\rho vr\epsilon - \frac{\partial}{\partial x}\,\frac{\mu_{eff}}{\sigma_\epsilon}\,\frac{\partial \epsilon}{\partial x} - \frac{\partial}{r\partial r}\,r\,\frac{\mu_{eff}}{\sigma_\epsilon}\,\frac{\partial \epsilon}{\partial r}$$

$$= \frac{\epsilon}{k}\,(C_1 G - C_2\rho\epsilon) \qquad (2\text{-}37)$$

where G is the production term given by

$$G = \mu_{eff} \left\{ 2\left[\left(\frac{\partial u}{\partial x}\right)^2 + \left(\frac{\partial v}{\partial r}\right)^2 + \left(\frac{v}{r}\right)^2 \right] + \left(\frac{\partial u}{\partial r} + \frac{\partial v}{\partial x}\right)^2 \right.$$

$$\left. + \left[r \frac{\partial}{\partial r} \left(\frac{w}{r}\right) \right]^2 + \left(\frac{\partial w}{\partial x}\right)^2 \right\} \qquad (2-38)$$

Examination of the above equations reveals that each contains terms for convection, diffusion, and source of the dependent variables. Consquently, the complete set of equations can be written compactly in a single general form for an arbitrary dependent variable ϕ:

$$\frac{\partial}{\partial x} \rho u \phi + \frac{1}{r} \frac{\partial}{\partial r} \rho v r \phi - \frac{\partial}{\partial x} \Gamma_\phi \frac{\partial \phi}{\partial x} - \frac{1}{r} \frac{\partial}{\partial r} \Gamma_\phi r \frac{\partial \phi}{\partial r} = S_\phi \qquad (2-39)$$

where Γ_ϕ is the effective diffusion coefficient and S_ϕ denotes the source term.

2-4 Boundary Conditions

The governing equations by themselves do not yield a solution to a given problem. Additional boundary information is required at the inlet, outlet, the axis of symmetry, and the solid wall. Examination of the existing literature shows that inlet boundary conditions are generally not well defined. Previous investigations, [29] and [30], have found that predictions are very sensitive to distributions of velocities and turbulence quantities at the inlet.

28

Therefore, experimental measurements at the inlet boundary should be used, if at all possible. Lacking this information, the only resort is to make some reasonable estimation regarding the values. In most cases, the velocity profile at the inlet will be specified or the Reynolds number based on inlet properties is known and the velocity assumed to be uniform. The turbulence kinetic energy and its rate of dissipation are generally estimated from the assumption of local equilibrium of turbulence or according to the following expressions, see [31] and [58]:

$$k = au^2 \tag{2-40}$$

$$\varepsilon = \frac{k^{1.5}}{\lambda D} \tag{2-41}$$

where D is the inlet diameter and a and λ are constants. Although the choice of these constants is arbitrary, they may, nevertheless, have some effect on the solution. The constants were taken, for the present application, to be those of Lilly and Rhode [31]: a = 0.03 and λ = 0.005.

Outlet boundary conditions have been found to be less troublesome in practice. At the outlet plane, the dependent variable or its flux is assumed not to change further in the direction normal to the outlet plane. Either the first or second derivative of a dependent variable in the normal direction is set to zero. The exit plane is located far

29

enough downstream where the flow is strongly outward-directed and will not influence the upstream properties. The boundary values at the exit are obtained from an extrapolation of values existing at the inner nodes. The velocity components thus obtained must be adjusted to satisfy the overall mass balance with respect to the inlet mass flow.

Along the axis of symmetry, the gradient in the radial direction of all variables is set to zero, except for the radial velocity component v which is given a definite value of zero.

On the solid boundary, the no slip velocity boundary condition is applied. The wall shear stress is calculated from the log law or its alternative form

$$\tau_w = \frac{\rho \kappa \sqrt{k} C_\mu^{0.25} V_p}{\ln E y_p^+} \qquad (2\text{-}42)$$

A zero pressure gradient normal to the wall is often invoked and the pressure at the wall is approximated from extrapolation. Immediately at the wall, the turbulence energy vanishes, but the dissipation is finite. In practice, the turbulence energy and the dissipation at the point nearest to the wall are not computed from the equations but rather are determined from Equations (2-29) and (2-31) following the wall function concept.

CHAPTER 3

GENERATION OF GRID SYSTEM

In the development of a numerical procedure for solving the governing equations, the first step is to superimpose a grid distribution over the flow domain. For irregularly shaped flow domains, numerical methods of generating the grid have been widely used over the past several years. The underlying concept behind the method is to let the coordinates of the grid points emerge from the solution of a set of partial differential equations in the physical plane. The grid nodes thus generated will follow the shape of the flow configuration and part of the new coordinate lines will coincide with the boundary segments of the physical domain. This technique transforms an arbitrarily shaped physical plane into a square mesh in the computational domain. This not only eliminates the need for any interpolation at the irregular boundaries, but more importantly, allows the grid to be clustered in regions of sharp velocity gradients; thus, better resolution of the flow is provided. A typical coordinate transformation is shown in Figure 2.

Grid generation techniques have gained importance in the numerical solution of partial differential equations. Recent developments provide a variety of methods to generate and control the grid for better quality of solutions. A

comprehensive review of this subject can be found in references [32], [33] and [34].

In the present study, the method developed by Thomas and Middlecoff [35] was adopted. They solved a set of Poisson equations to generate the grid system. A source function was employed in each equation for controlling grid spacings. The proposed source functions contain adjustable parameters which are determined from the boundary values. As a result, the grid distribution was entirely controlled by an a prior selection of boundary grid points.

The equations for grid generation are given by:

$$\xi_{xx} + \xi_{yy} = R(\xi, \eta)$$

$$\eta_{xx} + \eta_{yy} = Q(\xi, \eta) \tag{3-1}$$

To obtain the coordinates of the transformed system, the dependent variables in the above equations must be inverted with the independent variables. This inversion yields

$$\alpha x_{\xi\xi} - 2\beta x_{\xi\eta} + \gamma x_{\eta\eta} = -J^2(R x_\xi + Q x_\eta)$$

$$\alpha y_{\xi\xi} - 2\beta y_{\xi\eta} + \gamma y_{\eta\eta} = -J^2(R y_\xi + Q y_\eta) \tag{3-2}$$

where $\alpha = x_\eta^2 + y_\eta^2$

$$\beta = x_\xi x_\eta + y_\xi y_\eta$$

$$\tag{3-3}$$

32

$$\gamma = x_\xi^2 + y_\xi^2$$

and J denotes the Jacobian of the transformation

$$J = x_\xi y_\eta - x_\eta y_\xi$$

The source functions R and Q are used to control the interior grid spacing. Following Thomas and Middlecoff, these are assumed to have the form:

$$R(\xi,\eta) = x(\xi,\eta)[\xi_x^2 + \xi_y^2]$$

$$Q(\xi,\eta) = \psi(\xi,\eta)[\eta_x^2 + \eta_y^2] \qquad (3\text{-}4)$$

where x and ψ are free parameters which are evaluated by the following equations:

$$x(\xi,\eta) = -\frac{x_{\xi\xi}x_\xi + y_{\xi\xi}y_\xi}{x_\xi^2 + y_\xi^2}$$

$$(3\text{-}5)$$

$$\psi(\xi,\eta) = -\frac{x_{\eta\eta}x_\eta + y_{\eta\eta}y_\eta}{x_\eta^2 + y_\eta^2}$$

On the boundaries, the (ξ,η) grid points and their locations are written in terms of the physical coordinates (x,y). Therefore, the derivatives of x and y with respect to ξ can be calculated on the constant η boundary lines. Similarly, the derivatives of x and y with respect to η can be calcu-

lated on the constant ξ boundary lines. The parameters χ and ψ are then evaluated on the η and ξ boundary lines, respectively, according to Equation (3-5). Once the parameter χ at each mesh point on the η boundary lines and the parameter ψ on the ξ boundary lines are obtained, their values at interior points can be approximated by using linear interpolation.

Upon introducing R and Q into Equation (3-2), the final form of the governing equations are

$$\alpha(x_{\xi\xi} + \chi x_{\xi}) - 2\beta x_{\xi\eta} + \gamma(x_{\eta\eta} + \psi x_{\eta}) = 0$$

$$\alpha(y_{\xi\xi} + \chi y_{\xi}) - 2\beta y_{\xi\eta} + \gamma(y_{\eta\eta} + \psi y_{\eta}) = 0 \qquad (3-6)$$

The pair of expressions in Equation (3-6) are solved simultaneously on a uniform, rectangular grid, having grid spacings $\Delta\xi$ and $\Delta\eta$ equal to one. Solution of these equations must account for the boundary conditions that specify the set of (x,y) values corresponding to the (ξ,η) points on the boundaries in the computational plane.

Figure 3 shows the relation between the grid that is generated for a bifurcated diffuser in the physical plane and that in the computational plane. It can be seen that the curved boundaries of the bifurcated diffuser are mapped into straight lines and the irregular grid in the physical plane is transformed into a square mesh in the computational plane.

CHAPTER 4

TRANSFORMATION OF BASIC EQUATIONS

Once the curvilinear coordinates are generated for a given flow domain, the governing equations and boundary conditions must be transformed in terms of these coordinates. There are two possible choices of performing the transformation: one retains the physical components of velocity, while the other uses contravarient velocity components of the new coordinate system. The former approach was used by Rhie and Chow [36] and by Shyy et al. [37]. The latter method was used by Demirdzic et al. [9]. Vinokur [38] has shown that for an axisymmetric flow, the governing equations based on contravariant velocity components, when discretized, will be cast into non-conservative form. Hindman [39] examined the results of an unsteady Euler equation in several conservative and non-conservative law forms. Based on his solutions, the conservative form was found preferable over the non-conservative form, especially when a shock wave was present. Hindman's result, though, is not definitely applicable to the current class of turbulent flow problems. However, it is expected that the conservative law form may eventually be more acceptable for numerical purposes.

According to general transformation rules, the partial derivatives of a function, say ϕ, in cylindrical coordinates

35

(x,r) can be transfromed to curvilinear coordinates (ξ, η) by means of following relations:

$$\frac{\partial \phi}{\partial x} = \frac{r_\eta}{J} \frac{\partial \phi}{\partial \xi} - \frac{r_\xi}{J} \frac{\partial \phi}{\partial \eta}$$

$$\frac{\partial \phi}{\partial r} = \frac{x_\xi}{J} \frac{\partial \phi}{\partial \eta} - \frac{x_\eta}{J} \frac{\partial \phi}{\partial \xi} \qquad (4-1)$$

Substituting Equation (4-1) into Equation (2-39), the flow-field in the new coordinate system will be governed by

$$\frac{1}{J} \frac{\partial}{\partial \xi} \rho F_\xi \phi - \frac{1}{J} \frac{\partial}{\partial \xi} \left[\frac{\Gamma_\phi}{J} \left(\alpha \frac{\partial \phi}{\partial \xi} - \beta \frac{\partial \phi}{\partial \eta} \right) \right]$$

$$\frac{1}{rJ} \frac{\partial}{\partial \eta} \rho r F_\eta \phi - \frac{1}{rJ} \frac{\partial}{\partial \eta} \left[\frac{\Gamma_\phi r}{J} \left(\gamma \frac{\partial \phi}{\partial \eta} - \beta \frac{\partial \phi}{\partial \xi} \right) \right] = S_\phi(\xi, \eta) \qquad (4-2)$$

where $\quad F_\xi = u r_\eta - v x_\eta$

$$F_\eta = v x_\xi - u r_\xi \qquad (4-3)$$

The geometric factors α, β, γ and J have been defined in the previous chapter and are all known as part of the grid generation procedure.

The physical significancs of several of the terms given above may be advanced: $F_\xi/\sqrt{\alpha}$ and $F_\eta/\sqrt{\gamma}$ are the covariant velocity components normal to lines of constant ξ and η, respectively; $\sqrt{\alpha}$ and $\sqrt{\gamma}$ represent the distances between two grid points in the η and ξ directions; β is the angle between ξ and η lines in the physical plane thus, β is a measurement of orthogonality. It vanishes when a ξ line and

36

an η line are orthogonal; and, finally, J denotes the area in the (ξ,η) plane.

Equation (4-2) has been used by Shyy [7] to solve for the flow in a dump diffuser. Further, a two dimensional form of this equation was used by Rhie and Chow [36] to determine flow past an isolated airfoil. Shyy et al. [37] also used it to determine the flow in a gas turbine combustor.

Along with the governing equations, the boundary conditions must also be transformed into curvilinear coordinates. If Dirichlet boundary conditions are applied, the dependent variables remain the same in both coordinates, so that

$$\phi(\xi,\eta) = \phi(x,y) \tag{4-4}$$

If Neumann boundary conditions are applied, the derivatives $\frac{\partial\phi}{\partial n}\Big|_{\xi}$ or $\frac{\partial\phi}{\partial n}\Big|_{\eta}$ must be written in terms of (ξ,η) coordinates. The unit vector normal to a ξ coordinate is given by

$$\vec{n}_{\xi} = \frac{d\vec{r} \times \vec{k}}{\left|\frac{dr}{ds}\right|} \tag{4-5}$$

where $\vec{r}$ = position vector of a point on the coordinate line;

  s = arc length along the line; and

  $\vec{k}$ = unit normal perpendicular to the (ξ,η) plane.

Now, since $\frac{d\vec{r}}{ds} = \frac{dx}{ds}\vec{i} + \frac{dy}{ds}\vec{j} = (x_{\eta}\vec{i} + y_{\eta}\vec{j})\frac{d\eta}{ds}$ (4-6)

37

and $\left| \dfrac{d\vec{r}}{ds} \right| = \sqrt{x_\eta^2 + y_\eta^2} \; \dfrac{\partial \eta}{\partial s} = \sqrt{\alpha} \; \dfrac{\partial \eta}{\partial s}$ (4-7).

substituting these into Equation (4-5) produces

$$\vec{n}_\xi = \dfrac{1}{\sqrt{\alpha}} \left(\dfrac{\partial y}{\partial \eta} \vec{i} - \dfrac{\partial x}{\partial \eta} \vec{j} \right)$$ (4-8)

The derivative of a function in the direction normal to a constant ξ line is obtained through the following scalar product:

$$\dfrac{\partial \phi}{\partial n} \Big|_\xi = \vec{n}_\xi \cdot \nabla \phi = \dfrac{1}{J\sqrt{\alpha}} \left(\alpha \dfrac{\partial \phi}{\partial \xi} - \beta \dfrac{\partial \phi}{\partial \eta} \right)$$ (4-9)

In a similar manner, the unit vector and the derivative of a function normal to an η coordinate line are obtained:

$$\vec{n}_\eta = \dfrac{1}{\sqrt{\gamma}} \left(- \dfrac{\partial y}{\partial \xi} \vec{i} + \dfrac{\partial x}{\partial \xi} \vec{j} \right)$$ (4-10)

and $\dfrac{\partial \phi}{\partial n} \Big|_\eta = \dfrac{1}{J\sqrt{\gamma}} \left(\gamma \dfrac{\partial \phi}{\partial \eta} - \beta \dfrac{\partial \phi}{\partial \xi} \right)$ (4-11)

The unit vectors $\vec{n}_\xi$ and $\vec{n}_\eta$ are illustrated as they appear in the physical plane in Figure 4.

38

CHAPTER 5

NUMERICAL TECHNIQUE AND SOLUTION PROCEDURE

Two main features of the solution method used herein are employment of the finite volume approach and the SIMPLE (Semi-Implicit Method for Pressure-Linked Equations) algorithm. The latter was proposed by Patankar et al. [40]. In this chapter the grid arrangement, the finite volume method, numerical differencing schemes and the solution algorithm are described.

5-1 Grid Arrangement

It is well known that when using primitive variable solvers, if the pressure and velocities are stored at the same nodal location, a pressure oscillation will occur which, in turn, gives rise to convergence difficulties. The accepted method for resolving this problem is to use a staggered grid system [41] in which some flow varialbls, e.g., velocities, are defined on one set of nodes, and the other variables, e.g., pressure, are defined on a mesh that is shifted by one half a nodal-space with respect to the other mesh. This arrangement enables the velocity field to detect a pressure difference over a single grid space. Hence, any pressure change between two nodal points will immediately be reflected by velocities in the momentum equations.

39

Figure 5 shows the dependent variables defined in a general curvilinear coordinate system. Grid nodes are numerically generated at the intersection of two coordinate lines. The quadrilateral bounded by four adjacent grid lines forms a control volume or cell. The velocity components u and v are placed at the midpoint of the cell faces, while the other flow properties are placed at the center of the cell.

5-2 The Finite Volume Method

5-2-1 A General Transport Equation

The finite difference counterpart of the governing equation, Equation (4-2), is derived by using the finite volume method. This method assumes that each variable is enclosed in its own control volume. For a grid point P surrounded by its neighbors E, W, N, and S, see Figure 2, the governing equation is integrated over the control volume, $Jd\xi d\eta r d\theta$:

$$\int \{ \frac{1}{J} \frac{\partial}{\partial \xi} \rho F_\xi \phi - \frac{1}{J} \frac{\partial}{\partial \xi} [\frac{\Gamma_\phi}{J} (\alpha \frac{\partial \phi}{\partial \xi} - \beta \frac{\partial \phi}{\partial \eta})]$$

$$+ \frac{1}{rJ} \frac{\partial}{\partial \eta} \rho r F_\eta \phi - \frac{1}{rJ} \frac{\partial}{\partial \eta} [\frac{\Gamma_\phi r}{J} (\gamma \frac{\partial \phi}{\partial \eta} - \beta \frac{\partial \phi}{\partial \xi})] \} Jd\xi d\eta r d\theta$$

$$= \int S_\phi (\xi, \eta) Jd\xi d\eta r d\theta \qquad (5-1)$$

By taking $\Delta \xi = \Delta \eta = 1$, and cancelling $d\theta$, the resulting

40

equation yields

$$\rho r F_\xi \phi \Big|_w^e - \frac{\Gamma_\phi r}{J} \alpha \frac{\partial \phi}{\partial \xi}\Big|_w^e + \rho r F_\eta \phi \Big|_s^n - \frac{\Gamma_\phi r}{J} \gamma \frac{\partial \phi}{\partial \eta}\Big|_s^n$$

$$= S_\phi J r - \frac{\Gamma_\phi r}{J} \beta \frac{\partial \phi}{\partial \eta}\Big|_w^e - \frac{\Gamma_\phi r}{J} \beta \frac{\partial \phi}{\partial \xi}\Big|_s^n \tag{5-2}$$

To discretize Equation (5-2), a central differencing form is used for the diffusion terms and a linear interpolation scheme is employed to approximate the convections terms. For example, at the west face of a control volume the convection and diffusion terms are expressed, respectively, as:

$$\rho r F_\xi \phi \Big|_w = (\rho r F_\xi)_w \frac{\phi_P + \phi_W}{2} = \frac{C_W}{2} (\phi_P - \phi_W) \tag{5-3}$$

$$\frac{\Gamma_\phi r}{J} \alpha \frac{\partial \phi}{\partial \xi}\Big|_w = \left(\frac{\Gamma_\phi r}{J} \alpha\right)_w \frac{\phi_P - \phi_W}{\Delta \xi} = D_W(\phi_P - \phi_W) \tag{5-4}$$

Upon introducing expressions of the type immediately shown above into Equation (5-2), a finite difference relation between the variable at point P and its neighboring values is obtained, viz.,

$$A_P \phi_P = A_E \phi_E + A_W \phi_W + A_N \phi_N + A_S \phi_S + S^\phi \tag{5-5}$$

where

41

$$A_E = D_e - \frac{C_e}{2} \qquad A_W = D_W + \frac{C_W}{2}$$

$$A_N = D_n - \frac{C_n}{2} \qquad A_S = D_S + \frac{C_S}{2} \qquad (5\text{-}6)$$

$$A_P = A_E + A_W + A_N + A_S$$

and $$S^\phi = S_\phi Jr - \frac{\Gamma_\phi r}{J} \beta \frac{\partial \phi}{\partial \eta} \Big|_w^e - \frac{\Gamma_\phi r}{J} \beta \frac{\partial \phi}{\partial \xi} \Big|_s^n \qquad (5\text{-}7)$$

Equations of this kind are formulated for each of the flow variables u, v, w, k, and ε. The equation for the pressure, the remaining unknown variable, is established in the following section.

5-2-2 Pressure Equation

The pressure equation is obtained by combining the continuity equation and the momentum equations. In the transformed domain, the continuity equation takes the following form:

$$\frac{r_\eta}{J} \frac{\partial}{\partial \xi} \rho u - \frac{r_\xi}{J} \frac{\partial}{\partial \eta} \rho u + \frac{x_\xi}{Jr} \frac{\partial}{\partial \eta} \rho v r - \frac{x_\eta}{Jr} \frac{\partial}{\partial \xi} \rho v r = 0 \qquad (5\text{-}8)$$

Integrating this equation over a control volume which encloses a center node labled P, gives

$$\rho r F_\xi \Big|_w^e + \rho r F_\eta \Big|_s^n = 0 \qquad (5\text{-}9)$$

42

If correct values of the velocities u and v, and hence F_ξ and F_η, are inserted into Equation (5-9), the equation represents conservation of mass. That is, the left hand side of Equation (5-9) will be exactly zero. However, velocities obtained from the momentum equations for an assumed pressure distribution will generally not satisfy the continuity equation exactly. The assumed pressure distribution thus must be corrected and the velocities altered as well.

The assumed pressure field is labeled p* and the corresponding velocity fields are labeled u* and v*. The correct pressure and velocities will be

$$p = p^* + p'$$

$$u = u^* + u' \tag{5-10}$$

$$v = v^* + v'$$

where p' is the pressure correction and u' and v' are velocity corrections. To obtain the equations that govern u' and v', Equation (5-5) for the velocity components is rewritten by removing the pressure gradient from the source term. This gives an alternative form as:

$$A_p^u u_p = \sum_{i=E,W,N,S} A_i^u u_i + S^u - rr_\eta \frac{\partial p}{\partial \xi} + rr_\xi \frac{\partial p}{\partial \eta}$$

$$\tag{5-11}$$

$$A_p^v v_p = \sum_{i=E,W,N,S} A_i^v v_i + S^v - rx_\xi \frac{\partial p}{\partial \eta} + rx_\eta \frac{\partial p}{\partial \xi}$$

43

The starred velocities are obtained from the above equations by replacing u*, v*, and p* with corresponding variables, i.e.,

$$A_p^u u_p^* = \sum_{i=E,W,N,S} A_i^u u_i + S^u - rr_\eta \frac{\partial p^*}{\partial \xi} + rr_\xi \frac{\partial p^*}{\partial \eta}$$

$$\tag{5-12}$$

$$A_p^v v_p^* = \sum_{i=E,W,N,S} A_i^v v_i + S^v - rx_\xi \frac{\partial p^*}{\partial \eta} + rx_\eta \frac{\partial p^*}{\partial \xi}$$

By subtracting Equation (5-11) from Equation (5-12), the relations for the velocity corrections are found in terms of the pressure correction:

$$A_p^u u_p' = \sum_{i=E,W,N,S} A_i^u u_i' - rr_\eta \frac{\partial p'}{\partial \xi} + rr_\xi \frac{\partial p'}{\partial \eta}$$

$$\tag{5-13}$$

$$A_p^v v_p' = \sum_{i=E,W,N,S} A_i^v v_i' - rx_\xi \frac{\partial p'}{\partial \eta} + rx_\eta \frac{\partial p'}{\partial \xi}$$

These correction equations are merely intermediate devices that led to the final results. Thus, the omission of some of the terms in these equations will have little effect on the correctness of the final solutions [40]. Accordingly, the pair of expressions in Equation (5-13) are simplified by dropping the terms $\Sigma A_i^u u_i$ and $\Sigma A_i^v v_i$, i.e.,

$$u_p' = D^u \left(- r_\eta \frac{\partial p'}{\partial \xi} + r_\xi \frac{\partial p'}{\partial \eta} \right)$$

$$v_p' = D^V \left(- x_\xi \frac{\partial p'}{\partial \eta} + x_\eta \frac{\partial p'}{\partial \xi} \right)$$

where $D^u = \dfrac{r}{A_p^u}$ $\qquad D^V = \dfrac{r}{A_p^V}$

The correct velocities are then obtained by the following formulae:

$$u_p = u_p^* + D^u \left(- r_\eta \frac{\partial p'}{\partial \xi} + r_\xi \frac{\partial p'}{\partial \eta} \right)$$

(5-15)

$$v_p = v_p^* + D^V \left(- x_\xi \frac{\partial p'}{\partial \eta} + x_\eta \frac{\partial p'}{\partial \xi} \right)$$

The partial differential equation that describes the pressure correction p' is derived by introducing Equation (5-15) into the continuity equation, Equation (5-8). After integration over a control volume and use of the definition for F_ξ and F_η, it is found that

$$\left(-\rho r\alpha' \frac{\partial p'}{\partial \xi} + \rho r\beta' \frac{\partial p'}{\partial \eta} \right)\Big|_w^e + \left(-\rho r\gamma' \frac{\partial p'}{\partial \eta} + \rho r\beta' \frac{\partial p'}{\partial \eta} \right)\Big|_s^n$$

$$= -\rho r F_\xi^* \Big|_w^e - \rho r F_\eta^* \Big|_s^n \qquad (5-16)$$

where $\alpha' = D^u r_\eta^2 + D^V x_\eta^2$

45

$$\beta' = D^U r_\xi r_\eta + D^V x_\xi x_\eta \qquad (5-17)$$

$$\gamma' = D^U r_\xi^2 + D^V x_\eta^2$$

and F_ξ and F_η are defined in Equation (4-3), only here in terms of starred velocities. It is noted that terms containing β are usually small and it was subsequently found that solutions obtained by omitting these terms were not greatly affected by the omission. Therefore, these terms were dropped and a central difference was used for the derivatives of p'. The final form of Equaton (5-16), similar to Equation (5-5), is then

$$A_P P'_P = \sum_{i=E,W,N,S} A_i^p p'_i + m_p \qquad (5-18)$$

where $A_E^p = \rho r \alpha'|_e \qquad A_W^p = \rho r \alpha'|_w$

$$A_N^p = \rho r \gamma'|_n \qquad A_S^p = \rho r \gamma'|_s \qquad (5-19)$$

$$A_P^p = A_E^p + A_W^p + A_N^p + A_S^p$$

and $\quad m_p = -\rho r F_\xi^*|_w^e - \rho r F_\eta^*|_s^n \qquad (5-20)$

The source term m_p is essentially the continuity equation,

Equation (5-9) , evaluated in terms of starred velocities u*
and v*. It represents the mass imbalance of a control vol-
ume.

Once the finite difference equations for the dependent
variables are established, the momentum equations, pressure
equation, and turbulence model equation are coupled and
ready to solve. As the solutions approach a converged
value, the mass imbalance, mp, becomes smaller and smaller,
tending toward zero. At that stage, then, p' = 0 at each
grid point, which is the solution of Equation (5-18). Thus,
pressure and velocities need not be corrected further and
the starred pressure and velocities are the final results.

5-3 Numerical Differencing Schemes

In deriving Equation (5-5), a simple linear interpolation
has been used for the convection terms at the cell bound-
aries. This form is actually a central difference scheme,
which has been found to cause numerical instability in the
solution process unless a very small Peclet number is used.
One remedy for this problem is to make use of upwind differ-
encing. By this method, the convective quantities at the
cell boundaries are set equal to the values upstream of the
cell face instead of the average of the values on both
sides. Upwind differencing has been widely used because of
its superior stability properties. However, this method
introduces a so-called artificial or false diffusion error
which emanates from two sources: a relatively large trunca-

47

tion error and the non-alignment of the coordinates with the flow direction. This diffusion error can severely reduce the accuracy of the solution, particularly when the flow is dominated by convection.

Two approaches have been used to suppress the artificial diffusion error: higher order finite differencing schemes and accounting for the flow direction. The former practice has lead to the development, for example, of the quadratic upwind scheme [4], and the latter has resulted in the development of the skew upwind scheme [3]. Previous investigations have shown that these schemes are capable of producing more accurate numerical predictions than those of the conventional upwind scheme [42], [43]. The improvement is significant for laminar flows, but for high Reynolds number turbulent flows, the effective viscosity is much larger than the laminar value and the improvement is not as great. It must be mentioned that higher order differencing schemes can generate solutions having undesirable under- or overshoot values which are, in some cases, beyond physically realistic results. In addition, higher order schemes have been found to possess greater instability problems. Recent analyses, [5], [12] and [44], have also indicated that the accuracy of the numerical results obtained from higher order schemes were problem dependent and none of these schemes would give completely satisfactory solutions for all test cases. Because of these difficulties, it was decided that higher order differencing would not be investigated herein.

In this study, three basic numerical schemes: the hybrid, the quadratic upwind, and the skew upwind, will be applied. The hybrid scheme is a combination of conventional upwind differencing and central differencing. The convective terms are approximated with central differences if the grid Peclet number lies between -2 and 2; otherwise, an upwind scheme is employed. When the upwind scheme was used, physical diffusion was neglected. For example, on the west face of a control volume, the convection and diffusion terms in a hybrid scheme are expressed as:

$$(\rho r F_\xi)_w - (\frac{\Gamma_\phi r}{J} \alpha \frac{\partial \phi}{\partial \xi})_w$$

$$= (\rho r F_\xi)_w (\frac{\phi_P + \phi_W}{2}) - (\frac{\Gamma_\phi r \alpha}{J})_w (\phi_P - \phi_W) \qquad |P_e| \leq 2$$

$$= (\rho r F_\xi)_w \phi_W \qquad\qquad P_e > 2 \qquad (5\text{-}21)$$

$$= (\rho r F_\xi)_w \phi_P \qquad\qquad P_e < -2$$

In the quadratic upwind scheme, a cell edge value is determined by a quadratic interpolation using two adjacent nodal values together with the value at the next upstream node. As illustrated in Figure 6a, this scheme requires nine adjacent points to formulate an expression for all faces of a control volume. For a west face property in the quadratic upwind scheme, the following are used:

49

$$\phi_W = \frac{1}{2}(\phi_P + \phi_W) - \frac{1}{8}(\phi_{WW} + \phi_P - 2\phi_W) \qquad u_W \geq 0$$

$$(5-22)$$

$$= \frac{1}{2}(\phi_P + \phi_W) - \frac{1}{8}(\phi_W + \phi_E - 2\phi_P) \qquad u_W < 0$$

Skew upwind differencing is essentially the same as the hybrid scheme, except that when $|Pe| \geq 2$, the upwind scheme is performed on the true streamlines so both the flow direction and the angle between the flow and the grid lines are taken into consideration. Again, using the west face of a control volume as an illustration, as in Figure 6b, the general dependent variable for a skew upwind system is given by

$$\phi_W = \phi_1 \qquad\qquad P_e > 2$$

$$(5-23)$$

$$\phi_W = \phi_2 \qquad\qquad P_e < -2$$

The concept behind this scheme is simple, but the formulation to interpolate ϕ_1 or ϕ_2 is algebraically very cumbersome since four distinct regions for each control face are involved. Implementation of the above three computational methods are detailed in the Appendix.

It should be mentioned that the diffusion terms are always represented by central differences regardless of the value of the Peclet number. Also, application of the quadratic upwind scheme and the skew upwind scheme is only used

50

on the momentum equations. For the turbulence model equation, or the equation for any of the scalar properties, the hybrid scheme was used throughout.

5-4 The Solution Algorithm

The finite difference equations (Equation (5-5) for the velocities and turbulence quantities, and Equation (5-18) for the pressure correction) are solved iteratively following the SIMPLE algorithm [40]. This algorithm is a series of steps of estimations and subsequent corrections of the pressure and velocities. Two iteration sequences are employed: an inner sequence and an outer sequence. The outer iteration contains the following cyclic operations:

1. The intermediate velocities, u^* and v^*, are obtained by solving the corresponding momentum equations using the previous pressure field, p^* (at the first iteration p^* is assumed zero);

2. The pressure correction equation for p' is solved. This is followed by the subsequent correction of the pressure field p and the velocity fields u and v through Equations (5-10) and (5-14), respectively;

3. The equations for the remaining variables (k, ε, w) are solved in turn and then the viscosity is updated by means of Equation (2-23);

4. The whole process is repeated until a converged solution for each variable is achieved.

   The inner iteration sequence is employed to solve the

equation for each variable. Execution of the sequence is either by a line-by-line iteration using a tridiagonal matrix algorithm (TDMA) or by point iteration using the Guass-Seidel method. When using the line-by-line TDMA method, complete convegence of the solution is not necessary and usually 2 to 7 sweeps of the field suffice for the iteration. Alternately, if the Gauss-Seidel method is used, a change of less than 20% of the results between two consecutive iterations is adequate to advance the calculation to next step in the sequence.

5-5 Convergence, Stability, And Accuracy

Solution of the finite difference equations for the turbulent flow problems considered in this study requires underrelaxation at each iteration in order to suppress divergence. The underrelaxation factor is arbitrarily assigned and ranges from 0.1 to 0.5 depending on flow types, grid systems, and numerical schemes. The convergence criteria may be established based on the residual of the finite difference equation or on an evaluation of the mass imbalance at each axial station, i.e., (ms - min) x 100% /min (ms is the mass flow rate through each axial plane and min is the mass flow rate at the inlet). The latter criteria is applied in the current work. By this approach it is claimed that converged results are obtained if the mass imbalance is less than 0.01% in comparison with the mass inflow.

There are several potential sources of error in the

52

numerical solution of a differential equation. One source is associated with the coordinate transformation while another is due to the finite difference representation of the equation. In regards to the coordinate system, numerical error is a function of the grid spacing, its rate of change across the mesh and the departure of grid lines from orthogonality. A previous analysis [45] has shown that the use of Equation (4-1) in a coordinate transformation and subsequent finite differencing would reduce the solution of the partial differential equation to that of first order accuracy. Also, nonorthogonality introduces a factor of $(\sin\theta)^{-1}$ into the truncation error. Obviously, the smaller the angle between the grid lines, i.e., the larger the nonorthogonality, the larger the truncation error.

Numerical error related to the finite difference representation of the equation is normally viewed from the standpoint of the highest truncated term. However, in convective dominated transport problems, the false diffusion error could be more severe than the truncation error and should be taken into account in the error analysis. If this were not done, the skew upwind scheme would exhibit the same numerical accuracy as the conventional upwind scheme. Unfortunately, there does not appear to be a method to exactly evaluate the magnitude of the error that stems from numerical diffusion.

In addition to the errors examined here, there remains an important factor that could affect the solution accuracy:

53

the turbulence model used. It is well known that the k-ε model has serious defects, but is used only because it outperforms other turbulence models when all types of problems are considered. Taking all these errors into account, it is easy to understand that the numerical solution of turbulent flows is strongly dependent upon the grid, differencing methods, and the turbience model used.

CHAPTER 6

A ZONAL GRID TECHNIQUE

In the use of a zonal grid approach, the mesh for various regions of the field is generated separately. Therefore, the grid lines extending across two adjoining regions may not align with each other, and the transformation metrics across the zonal interface may not be continuous. Computation using a zoned grid method is based on the idea that each region of the field may be treated independently as a boundary value problem. The required boundary conditions are obtained either from physical arguments or from information supplied from adjacent regions using proper zonal boundary schemes. Across zone interfaces, two considerations must be observed: continuity of the dependent variables and conservation of fluxes. In the present work, a conservation form is developed that uses an interpolation method to transfer data from a coarse grid region to a fine grid region and an integration method for the reverse process.

Consider the pair of discontinuous grids shown in Figure 7. The line AB represents the zonal boundary that separates the fine grid (zone 1) and the coarse grid (zone 2). Let the coordinates be ξ^f and η^f for zone 1 and ξ^c and η^c for zone 2. The pair of indices i, j are used for ξ^f and

η^f, respectively, in zone 1 while the pair k, l are used for ξ^c and η^c, respectively, in zone 2. Since line AB is the last line of zone 1, it corresponds to imax. Also, for zone 2, the line AB corresponds to the index k=2. Suppose the solution is to be advanced on the fine grid in the direction from i=1 to i=imax. The calculation of the dependent variables at the position i=imax then requires values at the downstream points i=imax+1. To obtain the values at these zonal boundary points from zone 2, an overlapped region is generated by extending the constant η^f lines of zone 1 into zone 2 to intersect the line CD (k=3). This overlapping forms extra control volumes at the outlet of zone 1, as shown in Figure 8. The intersections have indices (imax+1,j) when referenced to zone 1. These points also correspond to indices (3,1) when referenced to zone 2. Values of the dependent variables enclosed in these outer control volumes located either at the cell face or at its center are obtained by interpolation of values from the coarse grid. For example, a variable located at the cell face, marked x, of a control volume PRST in Figure 8, is found by interpolation of values from its coarse grid neighboring points, marked o. The values at the x locations are then adjusted in order to satisfy global conservation as calculated from the coarse grid at the same cross section. The global conservation property is satisfied by requiring that

$$\int_D^C g^f d\eta^f = \int_D^C g^c d\eta^c \qquad (6-1)$$

56

where g^f and g^c are the fluxes through the zonal boundary CD for zone 1 and zone 2, respectively, and $d\eta^f$ and $d\eta^c$ are the corresponding elements of area normal to the flow direction. In a similar manner, flow properties located at the cell center can also be updated. The accuracy of the results depends upon the order of the interpolation scheme. A third order Lagrange polynomial was used to interpolate the values of u, v, and p. However, due to the large variation in the radial direction, and to prevent unrealistic negative values from appearing, a linear scheme was used for turbulence quantities.

To update the zonal boundary points of the coarse grid, the overlapped region is constructed by extending the constant η^c lines of zone 2 into zone 1. Consquently, these lines will intercept the line EF, as shown in Figure 9. Line EF corresponds to i=imax-1 of zone 1 or to k=1 of zone 2. It can be seen that this extension forms control volumes outside zone 2. The dependent variables enclosed in these exterior control volumes are established by an integration method which preserves the conservation properties of flow across the cell boundaries. For a control volume in the coarse grid having the boundary PQ as shown in Figure 9a, the flux across this area must equal that crossing the corresponding boundaries of fine grid, or

57

$$g^c = \frac{1}{\Delta \eta^c} \int_P^Q g^f \, d\eta^f \qquad (6\text{-}2)$$

If a piecewise constant variation of g between two grid points is assumed, as in Figure 9b, where the horizontal direction represents the numerical values of the flux and the vertical direction represents the grid points, the above equation can be rewritten in discretized form as:

$$g^c = \frac{1}{\Delta \eta^c} \sum_{j=P}^Q g_j^f \, \Delta \eta_j^f \, N_j \qquad (6\text{-}3)$$

where N_j is the fraction of flux of each control volume in zone 1 that enters the corresponding control volume of zone 2. It is noted that when $\Delta \eta^c$ equals $\Delta \eta^f$, g^c will be equal to g^f, and the flow properties will vary continuously across the boundary.

The zonal boundary procedure was applied at each iteration. When the computation was advanced from one zone to another, the zonal boundary points were first updated and then the interior points were computed.

CHAPTER 7

RESULTS AND DISCUSSION

To verify the developed numerical methods, predicted results
are compared with existing experimental values for selected
flow configurations of combustors and diffusers. These
include a sudden expansion combustor, a 45° expansion combu-
stor, a small angle conical diffuser and a bifurcated dif-
fuser. Most of the calculations were performed on a 40x21
grid, or more than 800 grid points. The grid chosen repre-
sents a compromise between accuracy and available computer
time. Three finite difference methods: hybrid, quadratic
upwind, and skew upwind, were applied to test the influence
of numerical diffusion. However, in many cases the more
advanced methods failed to produce a converged solution due
to stability problems. The first section in what follows
will present results computed using a single grid system,
while the second section will present results from zonal
grid calculations.

7-1 Results Using a Single Grid System

7-1-1 Flow in Combustor Geometries

Flow in a confined sudden expansion duct has a wide range of
engineering applications. Investigations of this flow have

frequently appeared in the literature and have been used to test the performance of computational techniques.

To simulate this flow, the boundary conditions were taken from the experimental conditions used by Chaturvedi [46]. At the inlet, the velocity profile is assumed flat and the Reynolds number is 2.5×10^5. The duct expansion ratio is 2.0, i.e., outlet diameter = 2 x inlet diameter. The inlet conditions for turbulence kinetic energy and dissipation energy were not provided and were therefore estimated according to Equations (2-39) and (2-40). The grid was arranged as shown in Figure 10 for a 40x21 mesh system; grid points were clustered in the inlet area and near the solid wall for better resolution. Predictions of velocity, turbulence energy, and pressure were compared with existing experimental data.

Figure 11 presents predicted and measured axial velocity profiles at three downstream positions, x/D = 1, 3 and 8, where D is the diameter of the inlet section. It can be seen that the results of the hybrid scheme and the quadratic scheme are almost the same. The predictions agree very well with the experimental data for most of the flow. The poorest agreement occurs at X/D=3.0, where the largest error is about 10%. The velocity decay along the axisymmetric axis is shown in Figure 12 along with the experimental data of Chaturvedi [46] and Stevenson et al [49]. The comparison is seen to be reasonably good for the three differencing methods used. The turbulence energy is compared in Figure

13. Since $\overline{u'u'}$ was measured in the experiments, in order to make the comparison it was assumed that $u' = \sqrt{2k/3}$. Although all of the predicted distributions have the same shape as those found experimentally, the magnitudes of the energy are not accurately predicted. The variation of turbulence intensity at the center line is shown in Figure 14. The calculated values are, for the most part, well below the measured values. The reason for this discrepancy is the deficiency of the turbulence model, which does not account for the extra strain terms in the calculation of the Reynolds stresses and the dissipation rate, [10] [58]. Figure 14 also indicates that low turbulence intensity is appropriate for representing the inlet condition for the kinetic energy equation. Many analyses, e.g. [29] and [30], have reported that the inlet values of k and ε have a significant influence on the numerical accuracy of the solution. Albeit current tests did not reveal that kind of influence, different inlet conditions of k and ε were found to change the solution by less than 10%.

Typical plots of the flow streamlines and the velocity flowfield are depicted in Figures 15 and 16, respectively. The recirculation zone is clearly identifiable and the strength of the recirculation is reflected by the size of the velocity vectors. The reattachment lengths, normalized with the inlet diameter, are listed in Table 1 for the various finite difference methods. Generally, the lengths are underpredicted by 10 to 15%, as reported by other investiga-

tions.

To evaluate the influence of numerical diffusion, the quadratic upwind and the skew upwind differencing methods have been incorporated into the solution algorithm. The results from these advanced schemes, however, did not show improvement over results obtained with the conventional hybrid scheme. This conclusion agrees with that observed by Hackman et al. [47] and by Syed and Chiappetta [6]. Both of these studies were concerned with flow over a backward facing step for both laminar and turbulent conditions. Their predictions of the reattachment length, when compared with measured values, indicated that an improvement by using advanced differencing schemes was significant for laminar flows, but only a small gain was realized for turbulent flows. This is probably due to the rather large effective viscosity that exists in turbulent flow which in turn forces the source term in the governing equation to dominate in the calculation process.

The numerical methods were applied to a 45° expansion combustor. Lilley and Rhode [31] analyzed this flow using a staircase of cells to represent the inclined wall. This permitted the computations to remain in a Cartesian coordinate system. The current work uses a coordinate transformation and grid generation technique which provide more flexibility in distributing the grid. The computations were performed in curvilinear coordinates with two different types of grid systems. The grids were generated as shown in

Figure 17 for grid I and in Figure 18 for grid II. The difference between these two mesh systems is the treatment of the inclined wall, which is part of the radial coordinate in grid I and is part of the axial coordinate in grid II. The grid spacings are contracted in the radial direction and expanded in the axial direction with factors of approximately 0.9 and 1.06, respectively.

The predicted velocity distributions at different downstream locations are shown in Figure 19 for grid I and in Figure 20 for grid II. The inlet Reynolds number is the same as for the sudden expansion case, Re = 2.5×10^5. Also shown on these figures are the experimental results of Chaturvedi [46]. When computed on the grid II mesh, the skew upwind scheme did not converge very well, even for very small values of the relaxation factor; thus these results are not shown in Figure 20. From Figures 19 and 20, it can been seen that on both grid systems the advanced schemes produced comparable accuracy to that of the solution found by using hybrid differencing. The centerline velocities are presented in Figures 21 and 22. The predictions on grid II are closer to the experimental data, but the error is relatively large at x/D = 6.0. The kinetic energy distributions are shown in Figures 23 and 24. In the recirculation region, the predictions are not accurate, but at downstream locations they improve significantly. The reason for this behavior is thought to be connected to the turbulence model, for it is known that the k-ε model does not produce accurate

results in separated flow regions. The spacial distribution of turbulence intensity is shown in Figure 25 for grid I. It should be noted that high turbulence intensity is generated along the shear layer and on the outskirts of the recirculation zone. A peak value is located approximately three diameters downstream from the flow inlet. Beyond the recirculation zone, the turbulence intensity begins to decay and a fully developed flow is gradually formed. Comparing the results on different grid systems, the calculation on grid II appears to produce better solutions. This is thought to be due to the mesh being more orthogonal in grid II, particulary in the inlet area.

Figure 26 presents the flow streamlines in a 45° expansion combustor. The reattachment length is determined by measuring the horizonal distance from the flow inlet to the rear reattachment point. The computed reattachment lengths on different grid systems using various differencing methods are shown in Table 2. Also listed are the results from a 20x20 grid and a 46x29 grid, along with the experimentally determined reattachment length, (4.5 times of the inlet diameter) as reported by Chaturvedi [46]. The computed rear stagnation points on a 20x20 coarse grid are substantially underestimated for all three differencing methods. The predictions tend to improve as the number of grid points increases except for the case when using the skew upwind scheme. For the hybrid and the quadratic upwind schemes, nevertheless, there is about a 10% error in the predicted

values when compared with the experimental result. The velocity profiles at various axial locations obtained from two different levels of grids, a 20x20 and a 40x21, are compared in Figure 27. The results computed on a 46x29 grid are very close to those computed on a 40x21 grid, and are not shown here. As can be seen, in the portion of the duct containing the recirculation region ($0.0 \leq x/D \leq 4.5$), the velocity computed from a 20x20 grid is underpredicted in the center portion of the duct. This underprediction indicates that the spreading rate of the flow in the radial direction is too rapid. Coincidentally, the size of the recirculation zone and the reattachment length are reduced. Comparing the compuations from the various grids reveals that the results are grid dependent for the 20x20 coarse mesh and approach stationary values in a 40x21 grid.

Additional information concering the number of iterations required to achieve a solution and the computational times are listed in Table 3. The skew upwind method requires the most iterations and computer time because of the rather lengthy calculation procedure required to determine the coefficients. In addition, it exhibits less stability than the other two schemes and needs smaller relaxation factors which causes the number of iterations to increase.

7-1-2 Flow In Diffusers

Diffusers have been widely used in combustors for converting

velocity head into pressure, and thereby stablizing the flame. Two types of diffusers were investigated: a conical diffuser and a bifurcated annular diffuser. Computer runs involving the conical diffuser were based on the data reported by Senoo et al. [48] for a conical diffuser with a 12 degree total expansion angle and an outlet to inlet area ratio of 4.0. The inlet Reynolds number was 3.0×10^5. All computations were performed on the 40x20 grid shown in Figure 28. Inlet conditions of axial velocity, u, and circumferential velocity, w, were taken from measured values. The radial velocity, v, was assumed to be zero. The turbulence properties were estimated from Equations (2-39) and (2-40) for the kinetic energy and the dissipation rate, respectively. Four swirl intensities: 0.0, 0.07, 0.12, and 0.18 were tested. The swirl intensity, m, is defined as:

$$m = \frac{\int uwrdr}{R \int u^2 \, dr} \qquad (7-1)$$

where R is the inlet radius.

The velocity at the outlet of the diffuser and the pressure recovery coefficient along the solid surfaces were compared with the experimental data of Senoo et al. [48]. Figure 29 presents a comparison of the outlet axial velocity across the diffuser for the four swirl intensities. As seen, for the non-swirling condition, i.e., m=0, predicted values are in very good agreement with the experimental

data. On the other hand, some disagreement is observed as the swirling intensity is increased. The circumferential velocity at the outlet of the diffuser for different swirl intensities is shown in Figure 30. Although most of the predictions are adequate, the disagreement is as large as 50% at some portions of the duct. The variation of pressure recovery coefficient with swirl intensity is shown in Figure 31. The pressure recovery coefficient, a measure of the efficiency of the diffuser, is defined as the ratio of the difference of the static pressure at the inlet and outlet to the inlet dynamic pressure of the mean axial velocity. The predictions are in good agreement with the experimental data for lower values of swirl intensity. Beyond a swirl intensity of approximately 0.1, the computations give smaller values than those measured. Errors at high swirl intensities stem from several possibilities, e.g., inlet boundary condition data, the numerical method used in the calculation procedure, and perhaps, most importantly, the turbulence model. The pressure coefficient is very sensitive to the inlet velocity profile, particularly the thickness of the boundary layer. Experimental studies [50] have already shown that as the boundary layer thickness is increased, diffuser efficiency decreases. A computation using a uniform velocity profile (no boundary layer) at the inlet resulted in the pressure recovery coefficient being much larger than the values measured. By changing the profile toward one possessing a thicker boundary layer, the coeffi-

cient was found to be dramatically reduced. In regards to the turbulence model, Habib and Whitelaw [10] and Sturgess and Syed [51] have reported that for complicated swirling flow conditions, the k-ε turbulence model is not adequate to describe the flow behavior accurately. This is due to strong curvature effects, brought about by rapid changes of the flow in the axial direction, which give rise to an extra rate of strain in addition to simple shear. This effect makes the assumptions regarding the constant Cμ and iso-tropic turbulence, used in the construction of the turbulence model, invalid. Modifications of the current model to account for this effect have been proposed, e.g., [51], but still require further validation.

Axial velocity contours for non-swirling flow, m = 0, and for the largest swirling flow condition, m=0.18, are plotted in Figures 32 and 33. These plots show that the two cases have completely different flowfields. In lightly swirling flows, the fluid is pressed toward the wall and suppresses the formation of separation. This effect enhances the fluid mixing near the boundary and decreases the boundary layer thickness. As a consequence, the pressure recovery is increased. However, when the swirl intensity is greatly elevated, a recirculation zone will be created along the center line. The central recirculation bubble reduces the effective cross sectional area and results in a low pressure recovery coefficient. The maximum efficiency of the diffuser is obtained by trading off the

effects between boundary layer thickness and the effective flow area brought about by swirl. As shown in Figure 29, the optimum swirl number for the maximum pressure recovery coefficient is approximately 0.12, for both the predicted and measured flows.

The bifurcated combustor prediffuser is designed to provide maximum efficiency, in terms of the pressure recovery, for the shortest length. A bifurcated diffuser is illustrated in Figure 34. The diffuser divides the flow into two parallel passages and directs almost equal amounts of flow to corresponding combustor chambers.

The flow simulation uses the experimental inlet boundary condition data of Lown et al. [52]. In their experiments, three different inlet velocity profiles were generated to test the performance of the diffuser, but only one of them, designated as the center peaked velocity profile, is employed in this study. The velocity profile of the flow at the inlet is shown in Figure 35. The average velocity at the diffuser inlet is 87 m/sec, the Reynolds number is approximately 2.2×10^5, and the Mach number is 0.247. Since the Mach number is below 0.3, the fluid can be treated as incompressible. Computations are performed on two levels of grids: a 17x13 and a 36x25. Three finite difference methods were used: the hybrid scheme, the skew upwind scheme and the quadratic upwind scheme. The grid distribution for the 36x25 mesh is shown in Figure 36. Since the actual diffuser is short, only 2.74 inches long, the usual boundary condi-

69

tion of zero normal gradient for dependent variables at the exit may not be fully realized. Thus, the exit boundary condition is assumed to be such that the second derivative of each variable with respect to ξ is zero. The velocity components at the outlet of both ducts are extrapolated from inner values and adjusted to satisfy the overall mass conservation. It is noted that flow rates through the inner duct and the outer duct were not specified, but rather were permitted to seek individual balances.

The velocity contours are plotted in Figures 37 and 38 for different numerical schemes on the two grid systems considered. The velocity was normalized by the average of the inlet velocity. The profiles computed by the skew upwind scheme and by the hybrid scheme were found to be very similar. This is expected since the coordinates were generated almost parallel to the streamlines; thus, the diffusion error arising from the streamline-grid-skewness was minimized. The results obtained by using the quadratic scheme show less diffusion in the radial direction than the other two schemes. The velocities at both diffuser outlets are plotted against the experimental data in Figures 39 and 40 for the 17x13 and the 36x25 grids, respectively. The experimental data was scaled so as to have the same basis as that used in the simulation. The predicted distributions are seen to agree fairly well with the measurements. The computed mass flow rates through the inner duct and the outer duct are compared with the measured values in Table 4. Pre-

dicted values are all rather close to the measured distributions: 48% through the outer duct and the remaining 52% through the inner duct. It is worth mentioning that, even on the coarse grid, the ratio of the mass division is predicted very well. Also, the velocity profiles at the diffuser outlet predicted on the coarse mesh were found to be more consistent with the experimental values than those predicted on the finer mesh. The flow streamlines and the velocity vectors obtained from using the hybrid scheme on the 36x25 grid are shown in Figures 41 and 42, respectively. The pressure distributions as predicted on the fine mesh for the three differencing schemes are shown in Figure 43. Examination of this figure reveals that all three schemes produce similar patterns, except near the outlet of the outer duct, where the quadratic upwind shows a small pressure drop due to separation. Predicted pressure coefficients along the inner and outer casings are compared with the experimental values in Figures 44 and 45, respectively. Prediction is very good along the outer casing, but the pressure coefficient is substantially overestimated on the inner casing. In addition, the simulation is unable to predict the pressure trough on the inner casing surface. The trough was measured near the diffuser inlet. At this point, it is not clear whether the disagreement is related to the computations or attributed to some experimental difficulty.

From the several comparisons between predictions and experimental data in combustor geometries and in diffusers,

it may concluded that numerical accuracy depends upon many factors. These include the coordinate system used, the turbulence model and the inlet flow conditions. The various numerical differencing schemes considered have been found to exhibit only a minor effect on the results. The accuracy of the results seems to involve the placement of the grid more than the numerical scheme used. In spite of the deficiency of the turbulence model, the flowfield is reasonably predicted even though the turbulence quantities can only be qualitatively simulated. In diffuser flow, a precise description of the inlet velocity profile is necessary in order to correctly predict the pressure recovery.

7-2 Results of Zonal Grid Calculations

The zonal grid approach will be demonstrated in this section for problems of flow in a 45° expansion combustor and in a bifurcated diffuser. The flow geometries are the same as those used in previous computations for a single grid system. The computations here are mainly used to verify the zonal boundary scheme developed earlier and to evaluate the effects of the finite differencing methods on the results.

7-2-1 Flow in a 45° Expansion Combustor

The flow domain of a 45° expansion combustor is divided into two zones separated by a zonal boundary. A fine grid is used to cover the inlet zone and the recirculation area, and

a coarse grid is used to cover the downstream region. The number of grid points used in the fine grid zone is 30x21, 15x20 and 30x30, whereas in the coarse grid zone a 5x12 mesh is used throughout. For the 15x20 and the 30x30 nets, the grid is evenly spaced in the radial direction; however, for the 31x21 net, the grid is clustered in the wall region. Figures 46 and 47 show the grid distribution for the uniform 30x30 and the non-uniform 30x21 nets, respectively. The discontinuity of coordinate lines at the zone interface is self evident. Prior testing with different computational schemes revealed that the final solution was determined more by how it was calculated in the upstream region than what differencing methods were used in the downstream zone. From this observation and the fact that the downstream flow is nearly parallel to the axial coordinate lines, computations were made using various differencing schemes in the fine grid zone, while the hybrid scheme was always applied in the coarse grid region.

Table 5 presents the calculated reattachment lengths for various computational schemes and meshes. The hybrid scheme produced more reliable results than did the other two schemes. Predictions based on the skew upwind scheme are very low, almost 30% smaller than the measured lengths. The lengths predicted when using the quadratic scheme are mixed. A possible reason for this behavior is that the zonal interface is not handled very well at the wall region because of high gradients that exist there. It was also

thought that the grid in the downstream zone might be too coarse. However, the mesh in the coarse grid zone was halved without appreciably affecting the results. The velocity profiles computed on the 30x30 mesh system are shown in Figure 48. The predictions compare favorably with the experimental data and also show improvement over the single grid results at the center portion of the duct at the location of L/D = 1.0, (refer to Figure 19). In the wall region, the predicted velocities vary according to the differencing method used. Consequently, the estimation of the reattachment length can be expected to differ even though the velocity field comparison is good for most regions of the flow. The radial distributions of turbulence intensity at different stations are shown in Figure 49. The results are essentially the same as those determined using a single grid system. In particular, within the recirculation zone the predictions are not in good agreement with the measured vaules, but in the downstream region the agreement is very good. Figures 50 to 52 depict streamline contours of the flow, and contours of the axial velocity and the turbulence intensity, respectively. The contours in each zone are plotted independently of each other. Lines of constant velocity and the flow streamlines are seen to be continuous across the zonal boundary. However, small discontinuities in the contours of the turbulence intensity may be observed because a less accurate interpolation scheme was used for this variable.

74

7-2-2 Flow in a Bifurcated Diffuser

The bifurcated diffuser was divided into three computational zones: an inlet zone and an upper and lower branch. Two different grid systems were used in the computations. The coarse grid has an 11x15 mesh in the inlet area and a 14x11 mesh in each of the upper and lower branches. The fine grid has 16x25, 21x17, and 21x17 grid points for the inlet and the two branches, respectively. The grid distribution for the coarse mesh is shown in Figure 53. Because each flow region is enclosed by a simple block, grids are more easy to generate.

The ratio of the mass division for various differencing methods and grid systems was first examined. The calculated and the measured mass split ratios are listed in Table 6. The skew upwind scheme and the hybrid scheme produced results with less grid dependency, and were in good agreement with the measured values. On the other hand, the predictions based on the quadratic scheme did not possess these characteristics; the results were found to be better when using the coarse grid than when using the fine grid. On the fine grid, the mass flow rate was overpredicted in the outer duct and underpredicted in the inner duct. The outlet velocity distributions are compared in Figures 54 and 55 for the coarse and the fine grids, respectively. It can be seen that the predicted shape of the velocity profiles generally agree with the experimenetal data. However, there is a dif-

75

ference between predicted and measured values in the regions near the solid wall. It is noted that in the fine grid system, the quadratic scheme overpredicted the velocity in the outer duct by a significant amount in the central region. Accordingly, the mass flow rate is overestimated as shown in Table 6. The velocity contours for three differencing methods are presented in Figure 56 for the coarse mesh and Figure 57 for the fine mesh. The flow patterns are generally the same as those produced using a single grid system, but possess less diffusion in the radial direction. The contours are observed to be continuous at most locations across zonal boundaries. Some discontinuities are seen near the solid wall of the outer duct when using the coarse grids. In that region, the velocity variation is large and the grids are too coarse to obtain accurate transfer of the required informatin. Comparing the velocity contours computed on the two different grid systems, it is found that the predictions using the hybrid scheme are more consistent than those using the other two schemes. When using the quadratic upwind scheme and the skew upwind scheme, the velocity pattern possesses a considerable change in the upper duct at the position the duct splits and also near the exit. Lines of constant pressure in two different mesh systems are shown in Figures 58 and 59. Some discontinuity was observed at the position where the ducts divide. The pressure gradients in this region are very large. Figure 59 also reveals that the pressure distributions are not quite

76

the same when using fine grid points. The reason is believed due to the nature of the pressure correction equation, which is known not to provide good correction of the pressure even though it corrects the velocity field very well [40]. Running in a fine grid system, it is found that the rate of convergence of the pressure field is much slower than that of the velocity field. Thus, even though the correct velocity field and the mass balance in each grid cell are obtained, a correct pressure field may not be completely established.

In this section it has been demonstrated that zonal grid calculations are capable of producing results of the same quality as those using a single grid system. The zonal approach has the additional advantage of permitting an optimized grid distribution by placing only necessary grid points in high gradient regions for the best resolution. Unfortunately, the computation, when crossing a zone interface, requires either integration or interpolation to update the boundary points of another zone. This additional procedure requires extra computer time which tends to offset the savings from using less grid points.

CHAPTER 8

CONCLUSIONS AND RECOMMENDATIONS

Turbulent flows in different combustor and diffuser geometries were predicted using the k-ε turbulence model and different numerical methods. In addition to a body-fitted coordinate transformation, a zonal method that partitioned the entire flow field into a number of subsections each having its own grid density and local computational scheme was incorporated for better utilization of the overall grid points. Whenever possible, comparisons have been made with existing experimental data, and have yielded good results. From the foregoing computations and analyses, the following conclusions and recommendations can be stated:

1. A numerical code for two-dimensional axisymmetrical turbulent flows has been developed to successfully describe the flow occurring in different configurations of combustors and diffusers;

2. A conservative zonal boundary scheme was developed for discontinuous grid calculations. The zonal boundary scheme was numerically stable in several test cases and permitted flow properties to be transferred smoothly across the zonal interface. The results demonstrated the capability of using the zonal approach in solving more complicated flow problems;

78

3. Numerical accuracy has been evaluated through the use of various computational schemes including hybrid, quadratic and skew upwind schemes. Basically, all three schemes generated comparable results on the same grid systems. With different grid systems, the predictions were varied. The number of grid points used was limited due to computer time and space; further refinement of the grids using a large computer is suggested for better results;

4. Although velocity and pressure fields were reasonably predicted by the $k-\varepsilon$ model, this model was found to be inadequate to describe the behavior of the turbulence quantities. Additional improvements in the $k-\varepsilon$ model or the use of more advanced Reynolds stress models are necessary for a better prediction of turbulence properties;

5. The computer code developed is limited to imcompressible, isothermal flows. To fully describe the phenomena of momentum, heat and mass transport in a combustion chamber, it is recommended that an energy equation and species continuity equations with appropriate chemical reactions should be incorporated into the program.

REFERENCES

1. Launder, B. E. and Spalding D. B., 'The Numerical Computations of Turbulent Flows', Comp. Meth. Appl. Mech. Eng., 3, p269, 1974.

2. Patanker, S. V. and Spalding, D. B., 'A Calculation Procedure for Heat, Mass & Momentum Transfer in Three Dimensional Parabolic Flows', Int. J. Heat & Mass Transfer, 15, p1785, 1972.

3. Raithby, G. D., 'Skew Upstream Differencing Schemes for Problems Involving Fluid Flow', Comp. Meths. Appl. Mech. Eng., 9, p153, 1976.

4. Leonard, B. P., 'A Stable and Accurate Convective Modelling Procedure Based on Quadratic Upstream Interpolation', Comp. Meths. Appl. Mech. Eng., 19, p59, 1979.

5. Syed, S., Gosman, A. and Peric, M., 'Assessment of Discretization Schemes to Reduce Numerical Diffusion in the Calculation of Complex Flows', AIAA-85-0441, Reno, Nevada, 1985.

6. Syed, S. and Chiappetta, L., 'Finite Difference Methods for Reducing Numerical Diffusion in TEACH-Type Calculations', AIAA-85-0057, Reno, Nevada, 1985.

7. Shyy, W., 'A Further Assessment of Numerical Annular Dump Diffuser Flow Calculations', AIAA-85-1440, Montery, California, 1985.

8. Pope, S. B., 'The Calculation of Turbulent Recirculating Flows in General Orthogonal Coordinates', J. Comp. Phys., 26, p197, 1978.

9. Demirdzic I., Gosman, A. D. and Issa, R. I., 'A Finite Volume Method for the Prediction of Turbulent Flow in Arbitrary Geometries', Lecture Series in Physics, Vol. 141, Eds., W. C. Reyolds and R. W. MacCormack, Springer-Verlag, Berlin, 1981.

10. Habib, M. A. and Whitelaw, H., 'The Calculation of Turbulent Flow in Wide-Angle Diffusers', Numerical Heat Transfer, 5, p145, 1982

11. Hah, C., 'Calculation of Various Diffuser Flows with Inlet Swirl and Inlet Distortion Effects', AIAA J., 21, p1127, 1983.

12. Shyy, W. and Correa, M., 'A Systematic Comparison of

Several Numerical Schemes for Complex Flow Calculations', AIAA 85-0440, Reno, Nevada, 1985.

13. Hessenius, K. A. and Pulliam, T. H., 'A Zonal Approach to Solution of the Euler Equation', AIAA 82-0969, St. Louis, Mo., 1982

14. Rai, M. M., 'A Conservative Treatment of Zonal Boundaries for Euler Equation Calculation', AIAA-84-0164, 1984.

15. Rai, M. M. and Hessenius, K. A., 'Metric-Discontinuous Zonal Grid Calculation Using the Osher Scheme', Computers and Fluids, 12, p161, 1984.

16. Atta Essam, H. and Vadyak, J., 'A Grid Overlapping Scheme for Flowfield Computations About Multicomponent Configurations', AIAA J., 21, p1271, 1983.

17. Berger, M. and Jameson, A., 'Automatic Adaptive Grid Refinement for fhe Euler Equations', AIAA J., 23, p561, 1985.

18. Boussinesq, J., 'Theorie de L'ecoulement Tourbillant', Mem. Pres. Acad. Sci., 23, p46, 1877.

19. Prandtl, L., 'Bercht Uber Untersuchung Zur Ausgebildeten Turbulenz', ZAMM, 5, p236, 1925.

20. Tennekes, H. and Lumley, J. L., 'A First Course in Turbulence', The MIT Press, Cambridge, Mass., 1972.

21. Rodi, W., 'Turbulent Models and Their Applications', IAHR Monograph, Delft, The Netherlands, 1980.

22. Launder, B. E. and Spalding, D. B., 'Mathematical Models of Turbulence', Academic Press, New York, 1972.

23. Harlow, F. H. and Nakayama, P. I., 'Turbulent Transport Equations', Physics of Fluids, 10, p323, 1967.

24. Jones, W. P. and Launder, B. E., 'Predictions of Low Reynolds Number Phenomena with a Two Equation Model of Turbulence', Int. J. Heat and Mass Transfer, 16, p1119, 1973.

25. Launder, B. E., Reece, G. J. and Rodi, W., 'Progress in the Development of Reynolds Stress Turbulence Closure', J. Fluid Mechanics, 68, p537, 1975.

26. Bradshaw, P. and Ferriss, D. H., 'Applications of a General Method of Calculating Turbulent Shear Layer', J. Basic Eng., 94, p345, 1973.

27. Khalil, E. E., 'Modelling of Furnaces and Combustors', Abacus Press, London, Britain, 1982.

28. Patel, V. C., Rodi, W. and Schenerrer, G., 'Turbulence Models for Near-Wall and Low Reynolds Number Flows: A Review', AIAA J., 23, p1308, 1985.

29. Syed, S. A. and Sturgess, G. J., 'Validation Studies of Turbulence and Combustion Models for Aircraft Gas Turbine Combustors', in 'Momentum and Heat Transfer Processes in Recirculating Flows', ASME HTD, 13, p71, 1980.

30. Krishnamurthy L. and Park, S. O., 'Isothermal Predictions of Recirculating Turbulent Flowfields of Confined Dual Coaxial Jets Behind an Axisymmetric Bluff Body', ASME 83-FE-14, 1983.

31. Lilley, D. G. and Rhode, D. L., 'A Computer Code for Swirling Turbulent Combustor Geometries', NASA Contractor Report, 3442, 1982.

32. Thompson, J. F., 'Grid Generation Technique in Computational Fluid Dynamics', AIAA J., 22, p1505, 1984.

33. Thompson, J. F., Editor, 'Numerical Grid Generation', North-Holland, 1982.

34. Thompson, J. F., Warsi, Z. V. A. and Mastin, C. W., 'Boundary-Fitted Coordinate System for Numerical Solution of Partial Differential Eqations - A Review', J. Comp. Phys., 47, p1-108, 1982.

35. Thomas, P. D. and Middlecoff, J. F., 'Direct Control of the Grid Point Distribution in Meshes Generated by Elliptic Equations', AIAA J., 18, p652, 1980.

36. Rhie, C. M. and Chow, W. C., 'Numerical Study of the Turbulent Flow Past an Airfoil with Trailing Edge Separation', AIAA J., 21, p1525, 1983.

37. Shyy, W., Correa, S. M. and Tong, S. S., 'Demonstration of a New Body-Fitted Coordinate Code for Modeling Gas Turbine Combustor Flows', AIAA-84-1381, Cincinnati, Ohio, 1984.

38. Vinokur, M., 'Conservation Equations of Gasdynamics in Curvilinear Coordinate Systems', J. Comp. Phys., 14, p105, 1974.

39. Hindman, R. G., 'Generalized Coordinate Forms of Governing Fluid Equations and Associated Geometrically Induced Errors', AIAA J., 20, p1359, 1982.

40. Patankar, S. V., 'Numerical Heat Transfer and Fluid

Flow', Hemisphere Publishing Corporation, New York, 1980.

41. Harlow, F. H. and Welch, J. E., 'Numerical Calculation of Time Dependent Viscous Incompressible Flow of Fluids with Free Surfaces', Physics of Fluids, 8, p311, 1965.

42. Leschziner, M. A., 'Practical Evaluation of Three Finite Difference schemes for the Computation of Steady-State Recirculating Flow', Comp. Meths. Appl. Mech. Eng., 23, p293, 1980.

43. Leschziner, M. A. and Rodi, W., 'Computation of Strongly Swirling Axisymmetric Free Jet', AIAA J., 22, p1742, 1984.

44. Smith, R. M. and Hutton, A. G., 'The Numerical Treatment of Advection: A Performance Comparison of Current Methods', Numerical Heat Transfer, 5, p439, 1982.

45. Mastin, C. W., 'Error Induced by Coordinate Systems', 'Numerical Grid Generation', p31, Ed. J. F. Thompson, North Holland, 1982.

46. Chaturvedi, M. C., 'Flow Characteristics of Axisymmetric Expansions', J. Hydraulic Division, Proceedings of ASCE, May, p61, 1963.

47. Hackman, L. P., Raithby, G. D. and Strong, A. B., 'Numerical Predictions of Flows Over Backward-Facing Steps', Int. J. for Numerical Methods in Fluids, 4, 711, 1984.

48. Senoo, Y., Kawaguchi, W. and Nagata, T., 'Swirl Flow in Conical Diffusers', Bulletin of the JSME, 21, p112, 1978.

49. Stevenson, W. H., Thompson, H. D. and Craig, R. R., 'Laser Velocimeter Measurements in Highly Turbulent Recirculating Flows', J. Fluids Engineering, 106, p173, 1984.

50. Schlichting, H., 'Boundary Layer Theory', 7th edition, McGraw Hill, 1979.

51. Sturgess, G. J. and Syed, S. A., 'Calculation of Confined Swirling Flows', AIAA-85-0060, Reno, Nevada, 1985.

52. Lown, H., Sabla, P. A. and Taylor, J. R., 'Energy Efficient Engine Component Development and Integration- Combustor Inlet Diffuser Aerodynamics Performance Evaluation', R80AEG611, General Electric, 1980.

53. Prandtl, L., 'Ubre ein nenes Formelsystem fur die

ansgebildate Turbulenz', Nachr. Akad. Wiss., Gottingen, Math.- Phys. Klasse, p6, 1945.

54. Rodi, W., 'On the Equation Governing the Rate of Turbulent Energy Dissipation', Imperial College, Mech. Eng. Rep. TWF/TN/A/14, 1971.

55. Rodi, W., 'A New Abgebraic Relation for Calculating the Reynolds Stresses', ZAMM 56, T219, 1976.

56. Launder, B. E., Priddin, C. H. and Sharma, B. I., 'The Calculation of Turbulent Boundary Layers on Spinning and Curved Surfaces', J. Fluids Eng., p231, 1977.

57. Leschziner, M. A. and Rodi, W., 'Calculation of Annular and Twin Parallel Jets Using Various Discretization Schemes and Turbulenc Model Variations', J. Fluids Eng., 103, p352, 1981.

58. Pourahmadi, F. and Humphrey, J. A. C., 'Prediction of Curved Channel Flow with an Extended k-e Model of Turbulence', AIAA J., 21, p1365, 1983.

59. Rastogi, A, K., 'Hydrodymanics in Tubes Perturbed by Curvilinear Obstructions', J. Fluids Eng., 106, p262, 1984.

APPENDIX A

Implementation of Numerical Schemes

In this section, the workable form for computing the coeffi-
cients of the finite difference version of the general gov-
erning equation will be derived. The main concern is to
estimate accurate values of the dependent variables at the
surface of the control volume while avoiding the instabili-
ties associated with the convective terms.

The integration of variable ϕ in Equation (4-2) over a
control volume with a center point P (refer to Figure 2)
yields:

$$\left(C_e \phi_e - D_e \frac{\partial \phi}{\partial \xi} \Big|_e \right) - \left(C_w \phi_w - D_w \frac{\partial \phi}{\partial \xi} \Big|_w \right)$$

$$\left(C_n \phi_n - D_n \frac{\partial \phi}{\partial \eta} \Big|_n \right) - \left(C_s \phi_s - D_s \frac{\partial \phi}{\partial \eta} \Big|_s \right) = S^\phi \qquad \text{(A-1)}$$

where
$$C_e = \rho r F_\xi \Big|_e \qquad D_e = \frac{\Gamma_\phi r}{J} \alpha \Big|_e$$

$$C_w = \rho r F_\xi \Big|_w \qquad D_w = \frac{\Gamma_\phi r}{J} \alpha \Big|_w$$

$$C_n = \rho r F_\eta \Big|_n \qquad D_n = \frac{\Gamma_\phi r}{J} \gamma \Big|_n \qquad \text{(A-2)}$$

$$C_s = \rho r F_\eta \big|_s \qquad\qquad D_s = \frac{\Gamma_\phi r}{J} \gamma \big|_s$$

and S^ϕ has been defined in Equation (5-7). Integration of the continuity equation yields:

$$C_e - C_w + C_n - C_s = 0 \qquad\qquad\qquad (A-3)$$

If Equation (A-3) is multiplied by ϕ_p and subtracted from Equation (A-1), it will give:

$$\left(C_e \phi_e - C_e \phi_p - D_e \frac{\partial \phi}{\partial \xi}\big|_e\right) - \left(C_w \phi_w - C_w \phi_p - D_w \frac{\partial \phi}{\partial \xi}\big|_w\right)$$

$$\qquad\qquad\qquad\qquad\qquad\qquad\qquad (A-4)$$

$$+ \left(C_n \phi_n - C_n \phi_p - D_n \frac{\partial \phi}{\partial \eta}\big|_n\right) - \left(C_s \phi_s - C_s \phi_p - D_s \frac{\partial \phi}{\partial \eta}\big|_s\right) = S^\phi$$

Equation (A-4) is the form to which different numerical schemes will be applied. For simplicity, only the coefficient associated with the flux on the west face of the control volume will be derived. The formulation on the other faces can be obtained in the same manner. Three differencing methods have been considered, viz., hybrid, quadratic upwind and skew upwind.

I. Hybrid Scheme

　　The hybrid scheme takes the upwind value and neglects

the diffusion term when the $|Pe| \geq 2$; otherwise central differencing is used for both convection and diffusion. Applying this relation to the west face, the flux becomes:

$$
Flux|_w = C_w(\phi_W - \dot{\phi}_P) \qquad\qquad P_e > 2
$$

$$
0 \qquad\qquad P_e < 2 \qquad\qquad (A-5)
$$

$$
(\frac{C_w}{2} + D_w)(\phi_W - \phi_P) \qquad\qquad |P_e| < 2
$$

A compact form of Equation (A-5) is written as:

$$
Flux|_w = A_W (\phi_W - \phi_P)
$$

$$
\text{where} \quad A_W = [\frac{C_w}{2} + \max(D_w, |\frac{C_w}{2}|)] \qquad\qquad (A-6)
$$

II. Quadratic Upwind Scheme

This method has been used in many investigations, but most do not mention the details of how the scheme might be implementated into a computer code. In the current study, the method, as described by Shyy and Correa [12], was applied. Substituting Equation (5-22) of the variable ϕ_w into Equation (A-1) for the flux at the west face of a control volume yields

$$\left(\frac{3}{4} C_W + D_W\right)(\phi_W - \phi_P) + \frac{C_W}{8}(\phi_P - \phi_{WW}) \qquad u_W > 0$$

$$\text{(A-7)}$$

$$\left(\frac{1}{4} C_W + D_W\right)(\phi_W - \phi_P) + \frac{C_W}{8}(\phi_W - \phi_E) \qquad u_W < 0$$

A compact form for the flux is written as:

$$\left[\frac{C_W}{4} + D_W + \frac{1}{2} \max(C_W, 0)\right](\phi_W - \phi_P)$$

$$+ \left[\max\left(\frac{C_W}{8}, 0\right)(\phi_P - \phi_{WW}) - \max\left(-\frac{C_W}{8}, 0\right)(\phi_W - \phi_E)\right] \qquad \text{(A-8)}$$

In practice, the first term constitutes the coefficient A_W, and the second term is moved to the right hand side of the equation and is combined with the source term.

III. Skew upwind scheme

A general form will not be derived here since a formula taking all the flow directions and angles into account is difficult to generate. Instead, the coefficient of A_W is determined individually for different u and v. Four different combinations of u and v are considered:

88
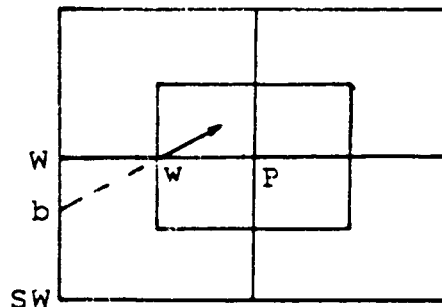
(1) when $u \geq 0$ and $v \geq 0$

In this condition, the upwind value falls between ϕ_{SW} and ϕ_W, and ϕ_W is taken to be

$$\phi_W = \alpha \phi_{SW} + (1 - \alpha) \phi_W \qquad \text{(A-9)}$$

where α is a proportionality constant. The maximum value of α is set equal to one, so the upwind point is never beyond the control volume and α is confined by

$$\alpha = \min\left(\frac{\overline{W\,b}}{\overline{SW\,W}}, 1\right) \qquad \text{(A-10)}$$

Applying Equation (A-9) to the flux term, it becomes:

$$Flux\big|_W = (C_W + D_W)(\phi_W - \phi_P) + C_W \alpha (\phi_{SW} - \phi_W) \qquad \text{(A-11)}$$

For other combinations of u and v, the resulting coefficients of A_W are expressed without comment as follows:

(2) when $u \geq 0$ and $v < 0$

$$\phi_W = \alpha \phi_{NW} + (1 - \alpha) \phi_W \qquad \text{(A-12)}$$

$$\alpha = \min\left(\frac{\overline{W\,b}}{\overline{NW\,W}}, 1\right) \qquad \text{(A-13)}$$

89

$$\text{Flux}|_W = (C_W + D_W)(\phi_W - \phi_P) + C_W \alpha (\phi_{NW} - \phi_W) \qquad \text{(A-14)}$$

(3) when $u < 0$ and $v \geq 0$

$$\phi_W = \alpha \phi_W + (1 - \alpha) \phi_P \qquad \text{(A-15)}$$

$$\alpha = \min(\frac{\overline{P\,b}}{\overline{P\,S}}, 1) \qquad \text{(A-16)}$$

$$\text{Flux}|_W = D_W(\phi_W - \phi_P) + C_W \alpha (\phi_P - \phi_S) \qquad \text{(A-17)}$$

(4) when $u < 0$ and $v < 0$

$$\phi_W = \alpha \phi_N + (1 - \alpha) \phi_P \qquad \text{(A-18)}$$

$$\alpha = \min(\frac{\overline{b\,P}}{\overline{N\,P}}, 1) \qquad \text{(A-19)}$$

$$\text{Flux}|_W = D_W(\phi_W - \phi_P) + C_W \alpha (\phi_P - \phi_W) \qquad \text{(A-20)}$$

For each face of the control volume, only one of above relations exists. The term with $(\phi_W - \phi_P)$ forms the coefficient A_W, and the other term containing α is included in the source term on the right hand side of the equation.

Table 1. Reattachment length for flow in a sudden expansion
combustor; Re = 2.5×10^5

Measurement [46]: L/D = 4.7

Method \ Grid	40x20
Hybrid	4.24
Skew	4.04
Quadratic	4.23

C-2

Table 2. Reattachment length for flow in a 45° expansion combustor; Re = 2.5x10^5

Measurement [46]: L/D = 4.5

Method \ Grid	20x20 grid I	40x21 grid I	40x21 grid II	46x29 grid I
Hybrid	3.68	4.19	4.07	4.19
Skew	3.67	3.04	-	-
Quadratic	3.36	4.05	4.02	4.72

Table 3. Number of iterations and compututational time for flow in a 45° expansion combustor

Number of iterations

Method \ Grid	20x20 grid I	40x21 grid I	grid II	46x29 grid I
Hybrid	379	422	816	950
Skew	300	522	-	-
Quadratic	277	392	720	720

Computational time

Method \ Grid	20x20 grid I	40x21 grid I	grid II	46x29 grid I
Hybrid	11' 8''	25'15''	41'58''	88' 8'
Skew	9'22''	34'10''	-	-
Quadratic	8'22''	24'31''	44' 6''	67'25''

Table 4. Mass split ratio in a bifurcated diffuser;
Re = 2.2×10^5

Measurement [52]: outer duct: 48%   inner duct: 52%

Method \ Grid	17x13		36x25	
	outer	inner	outer	inner
Hybrid	47.3	52.7	49.4	50.6
Skew	47.3	52.7	49.2	50.8
Quadratic	47.4	52.6	49.0	51.0

Table 5. Reattachment length for flow in a 45° expansion
combustor (zoned grid calculation)

Measurement [46]: L/D = 4.5

Grid Method	15x20, 5x12	30x30, 5x12
Hybrid	3.88	4.14
Skew	3.15	3.35
Quadratic	4.84	3.95

Grid Method	30x21(non-uniform), 5x12
Hybrid	4.01
Quadratic	4.46

Table 6. Mass split ratio in a bifurcated diffuser (zoned grid calculation)

Measurement [52]: outer duct: 48%   inner duct: 52%

Method \ Grid	11x15, 14x11, 14x11 outer	inner	16x25, 27x15, 27x15 outer	inner
Hybrid	48.1	51.9	46.3	53.7
Skew	47.2	52.8	48.6	51.4
Quadratic	46.8	53.2	51.2	48.8
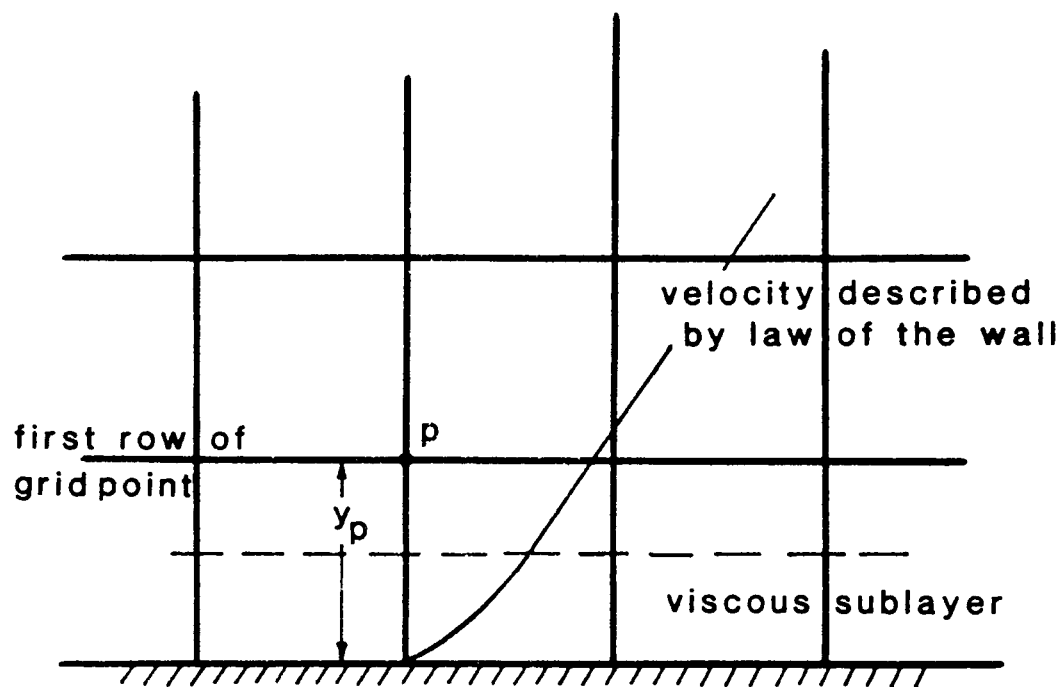
Figure 1. The grid network in the wall region
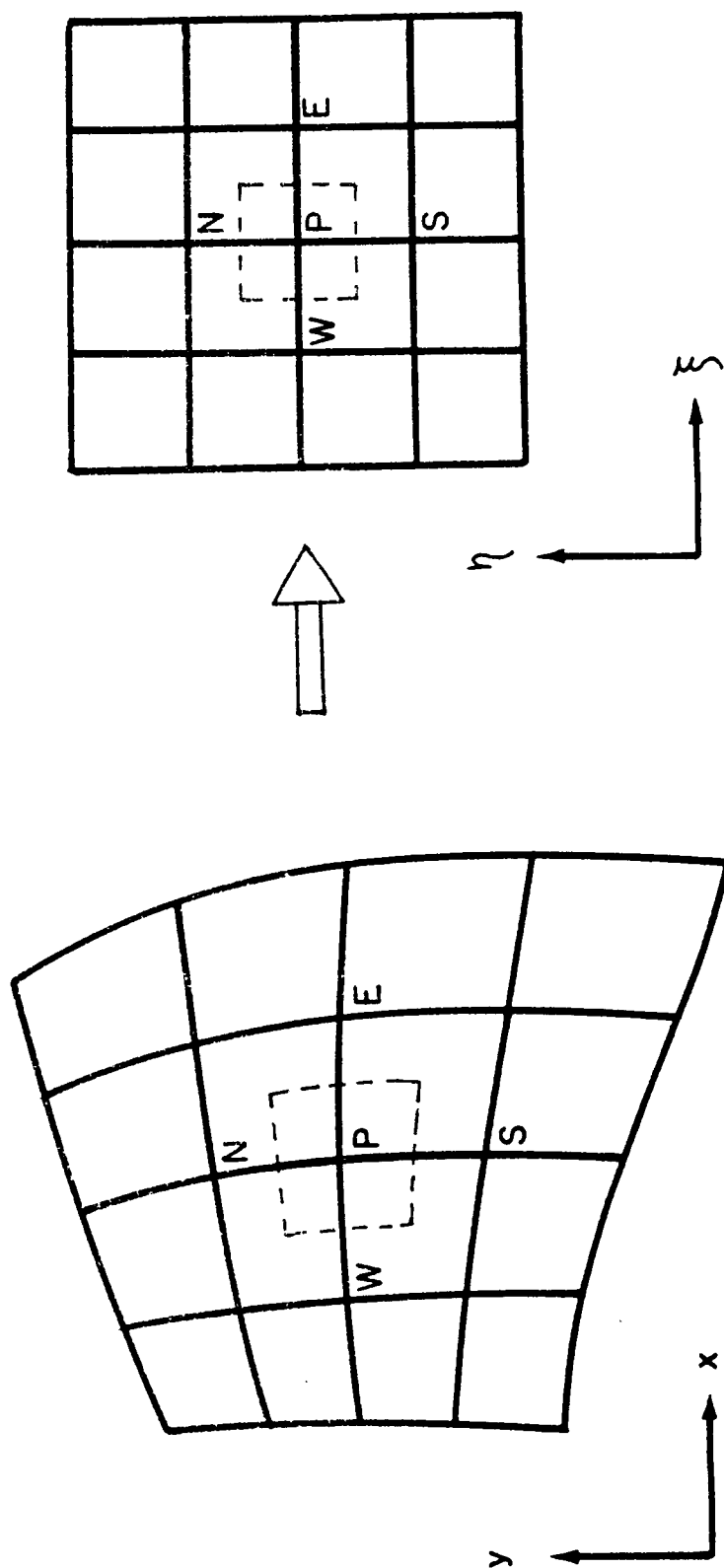
Figure 2. Coordinate transformation from physical plane to computational plane
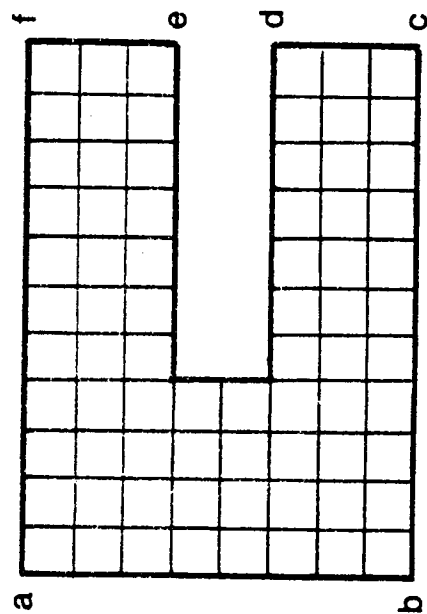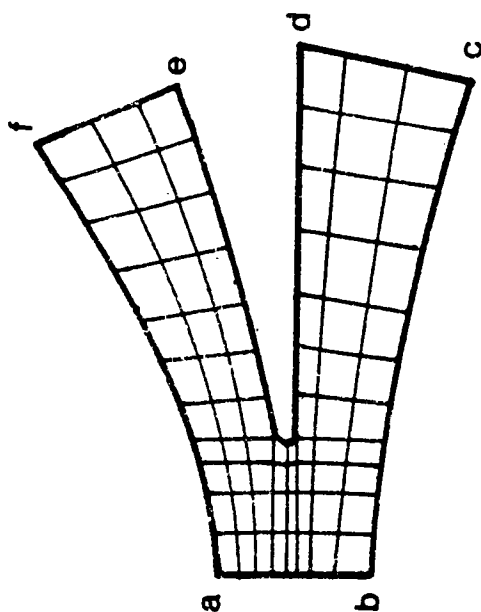
Figure 3. Grid distribution for a bifurcated diffuser in the physical plane and in the computational plane
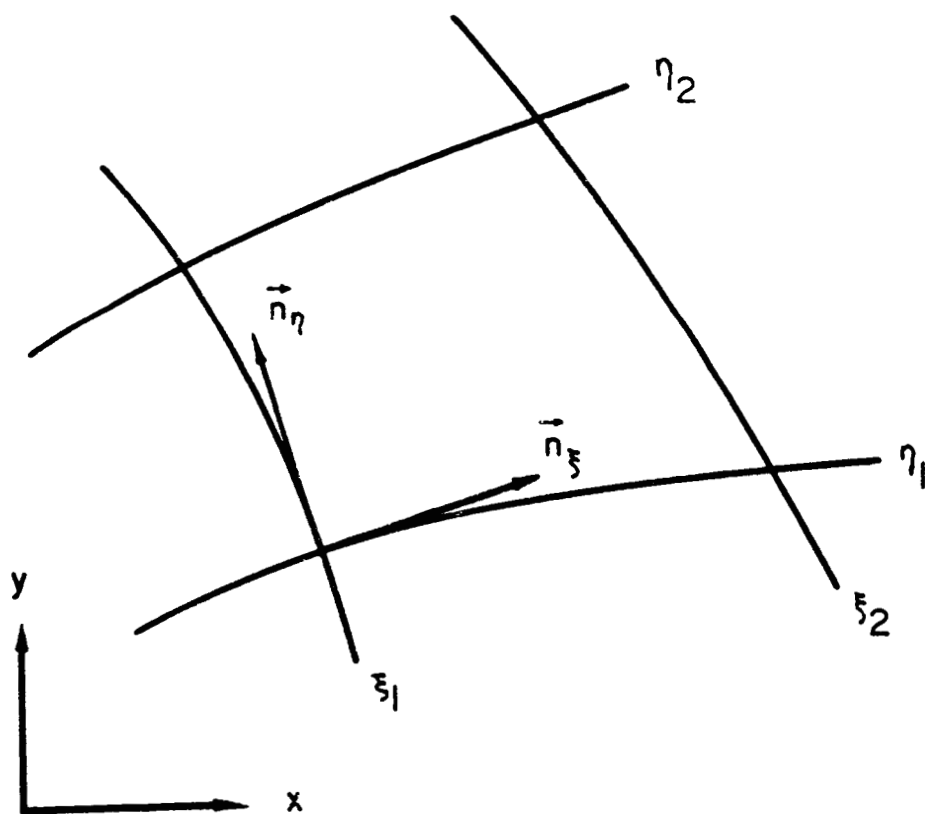
Figure 4. Unit tangent vectors
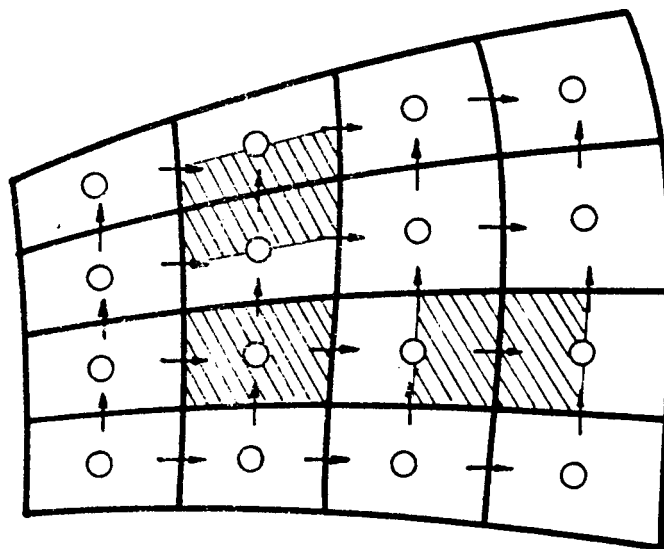
○   Grid for p, w, k, ε

➜   Grid for u

↑   Grid for v

Figure 5. Staggered grid and control volume in curvilinear
coordinates
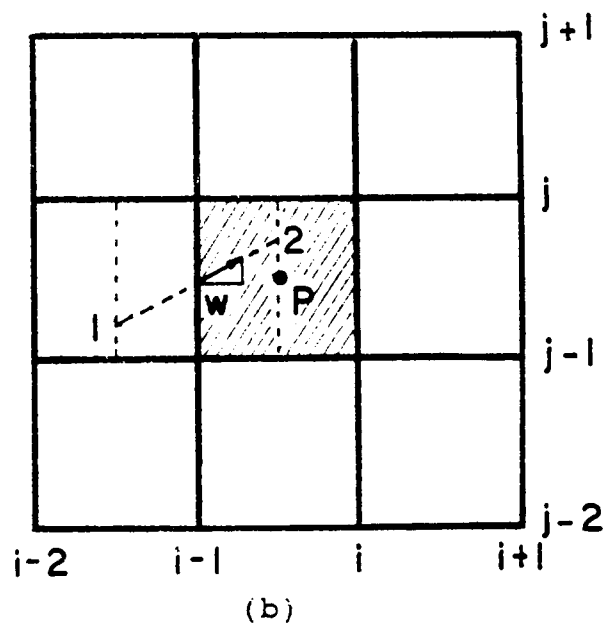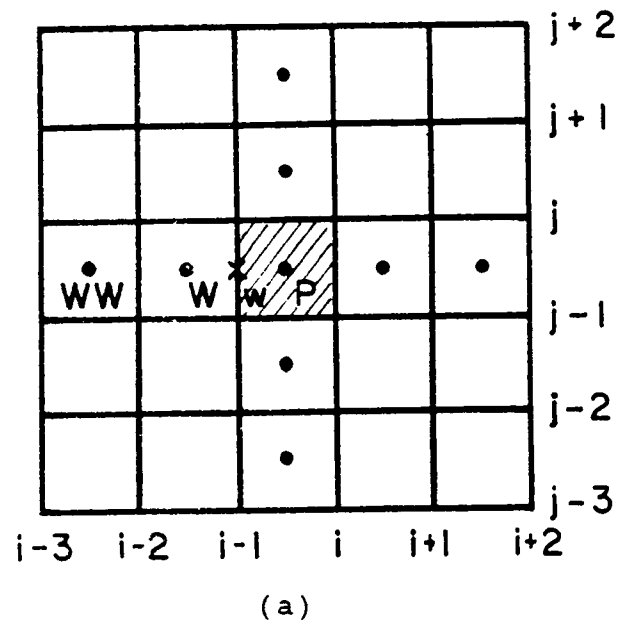
Figure 6. Numerical schemes for evaluating convection terms:
(a) quadratic upwind scheme; (b) skew upwind
scheme
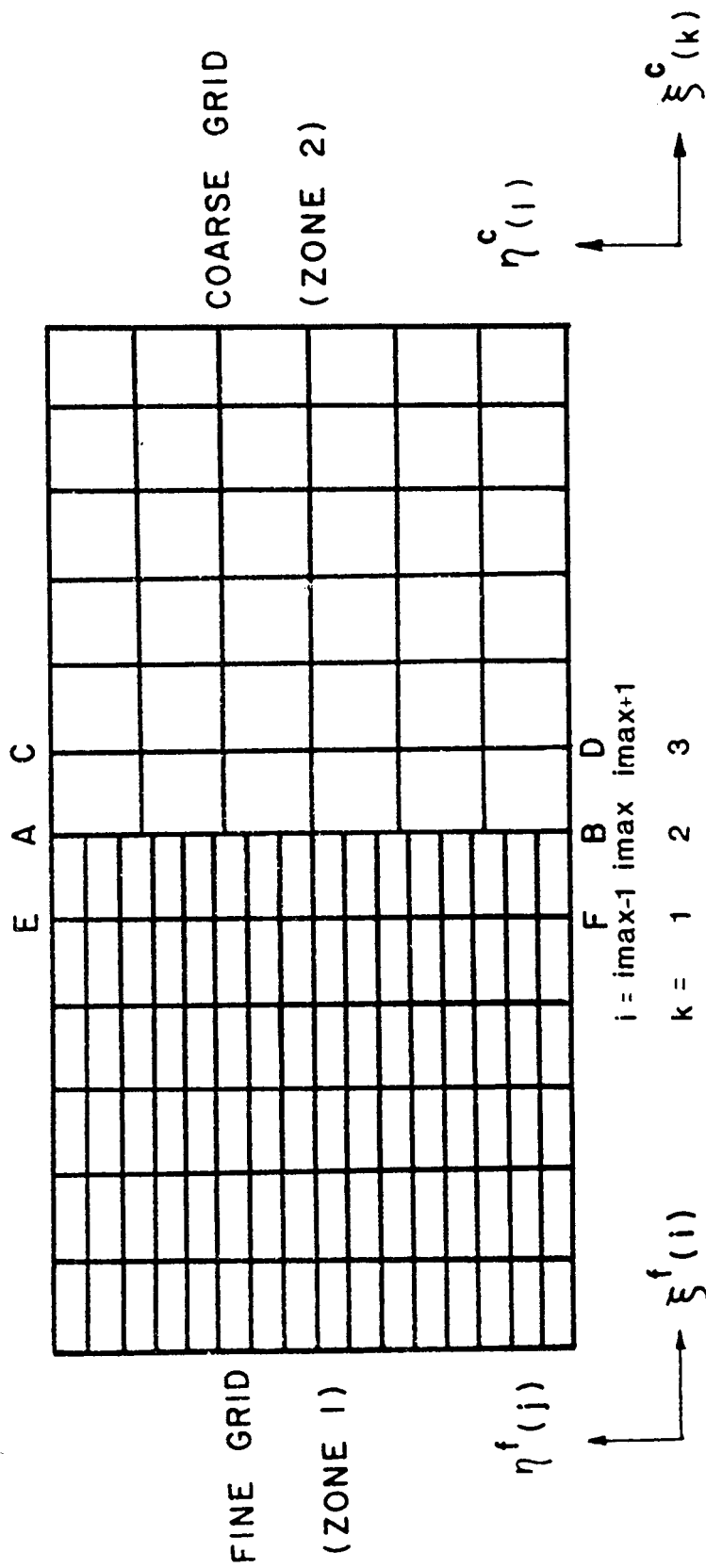
Figure 7. Illustration of a zoned grid
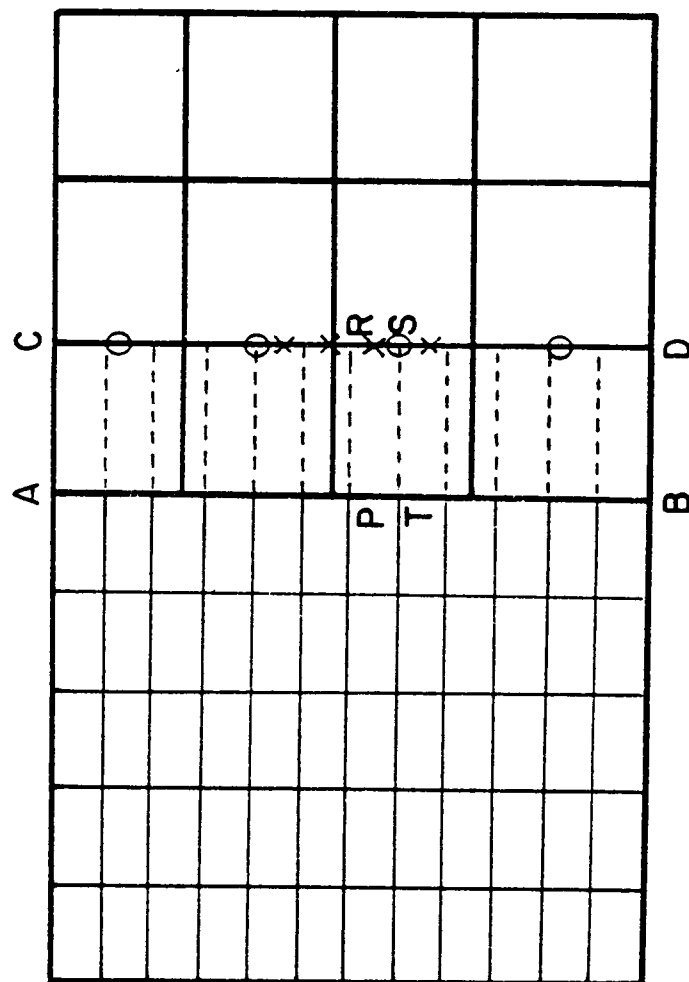
Figure 8. Zonal boundary scheme for updating fine grid points from overlapped control volumes
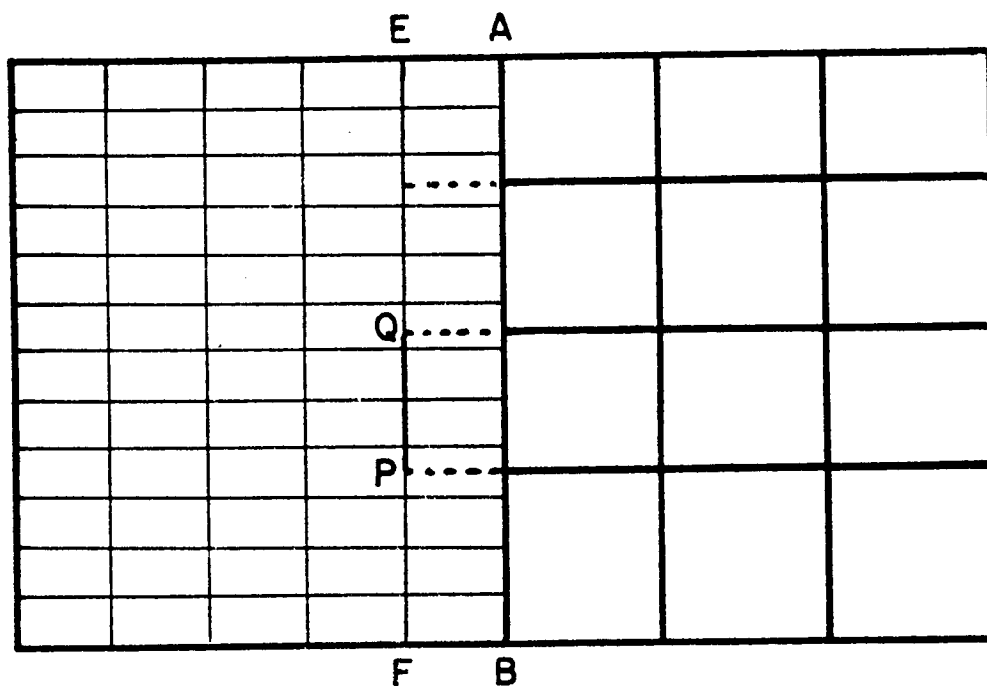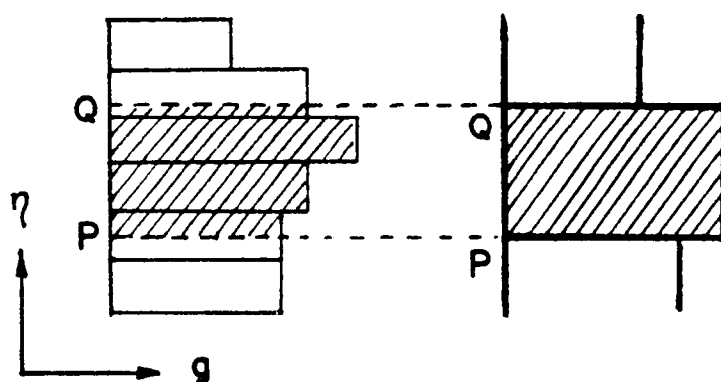
Figure 9. Zonal boundary scheme for updating coarse grid
points: (a) outer control volume; (b) piecewise
variation of the numerical flux through control
volume boundaries

105
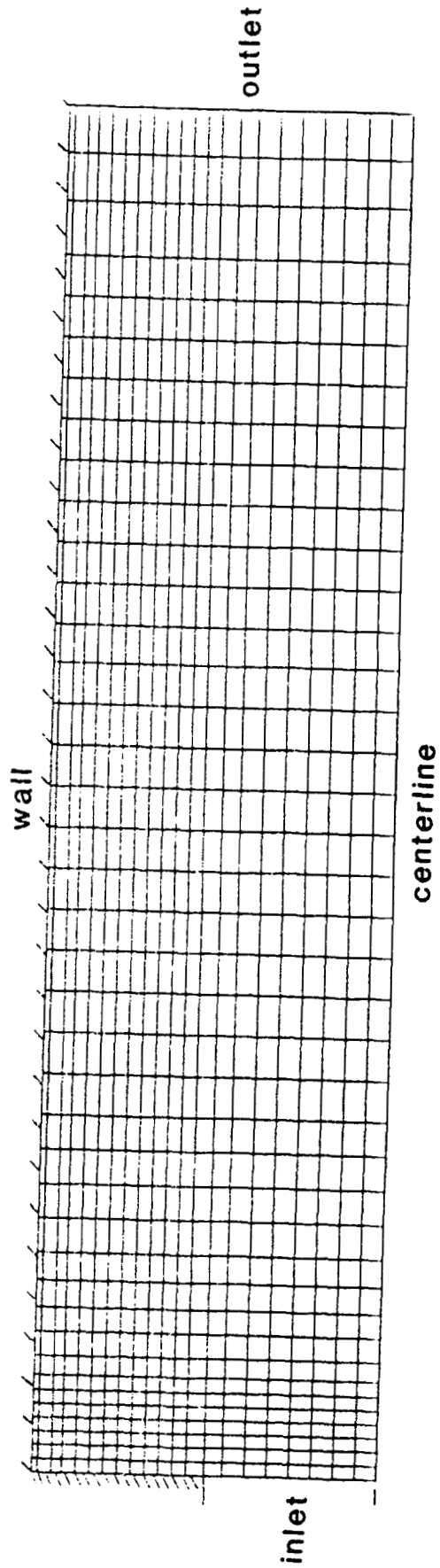
Figure 10. Grid point distribution for a sudden expansion combustor
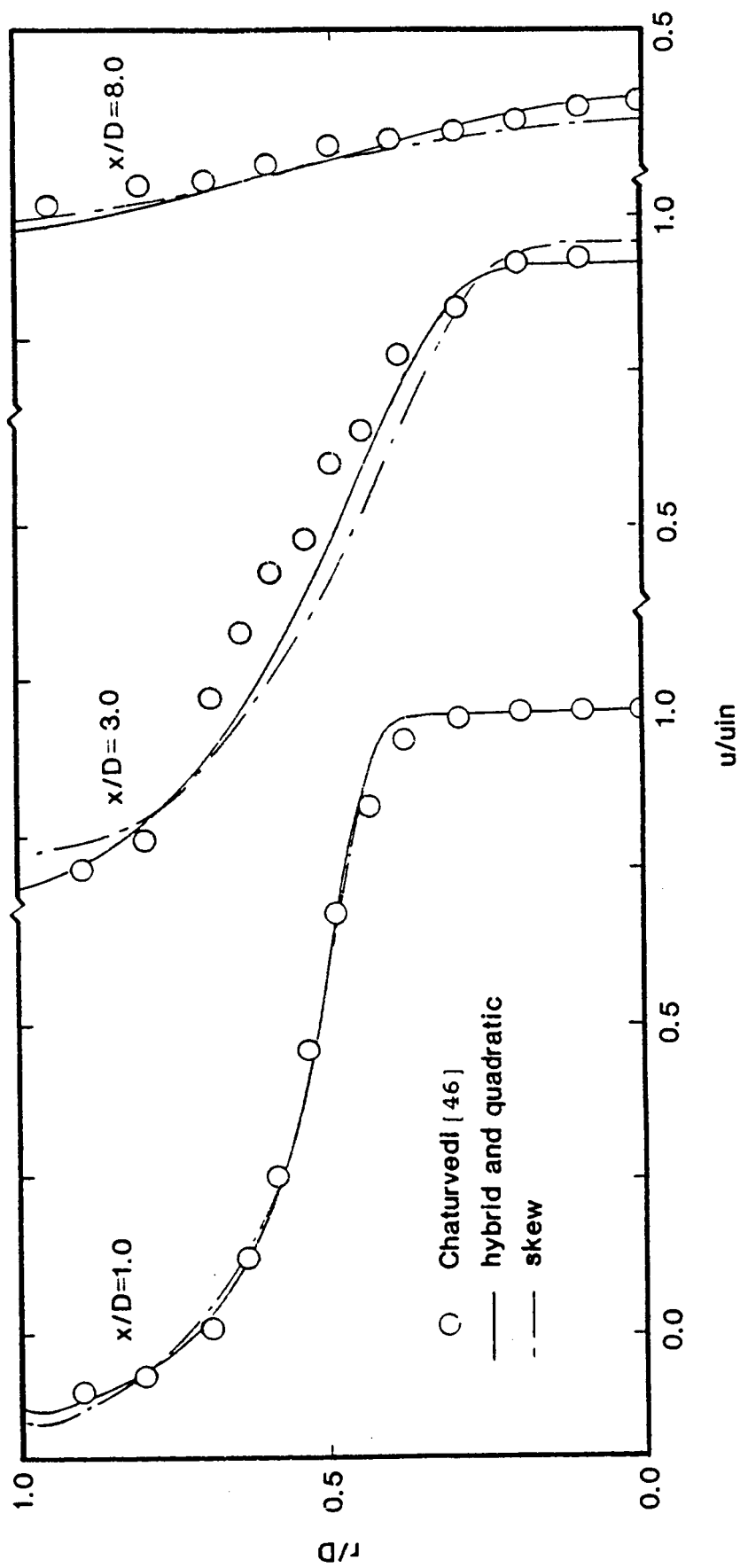
Figure 11. Axial velocity profiles at various axial locations for flow in a sudden expansion combustor
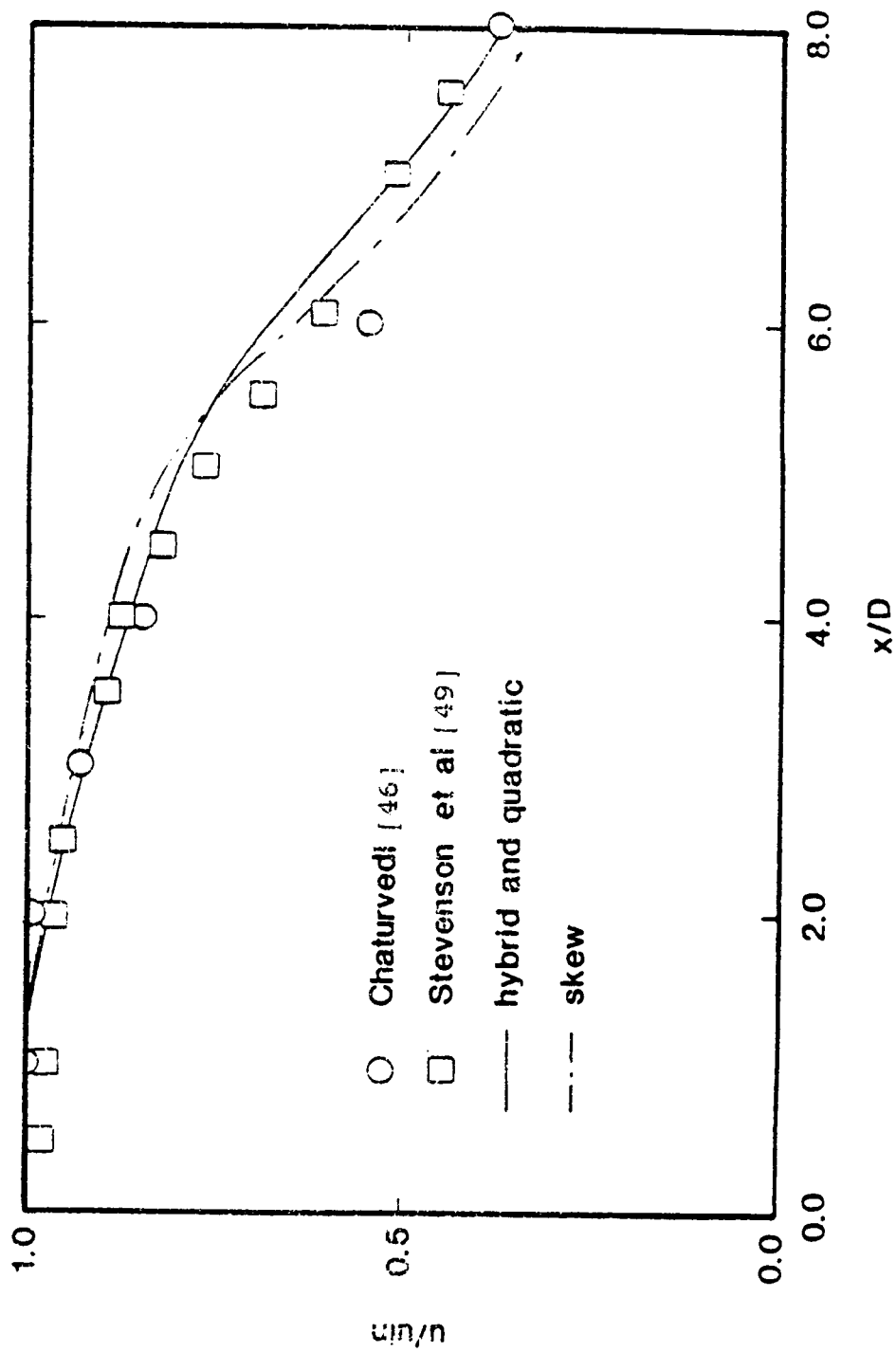
Figure 12. Variation of centerline velocity for flow in a sudden expansion combustor
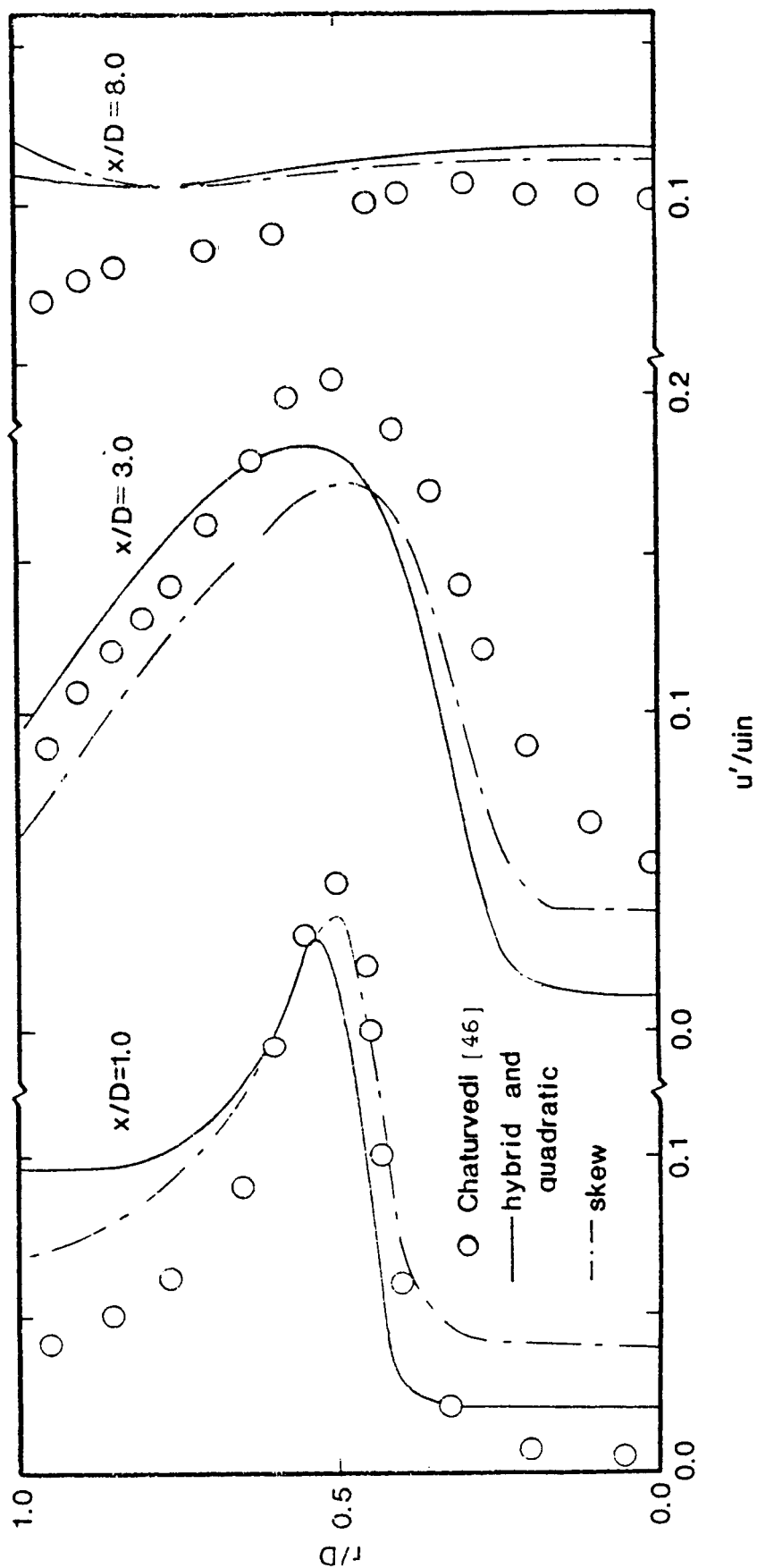
Figure 13. Turbulence intensity profiles at various axial locations for flow in a sudden expansion combustor
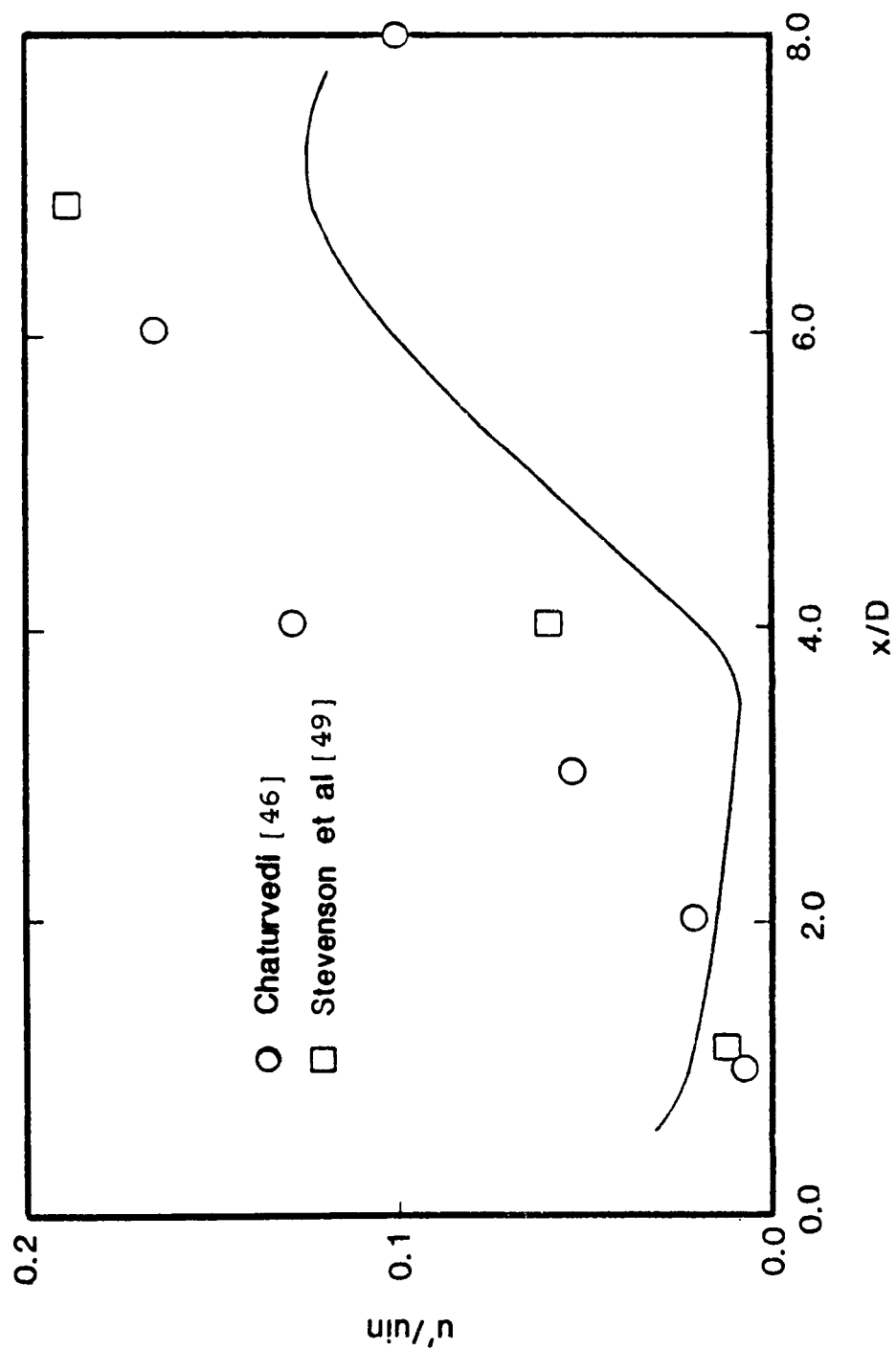
Figure 14. Turbulence intensity along the centerline in a
sudden expansion combustor
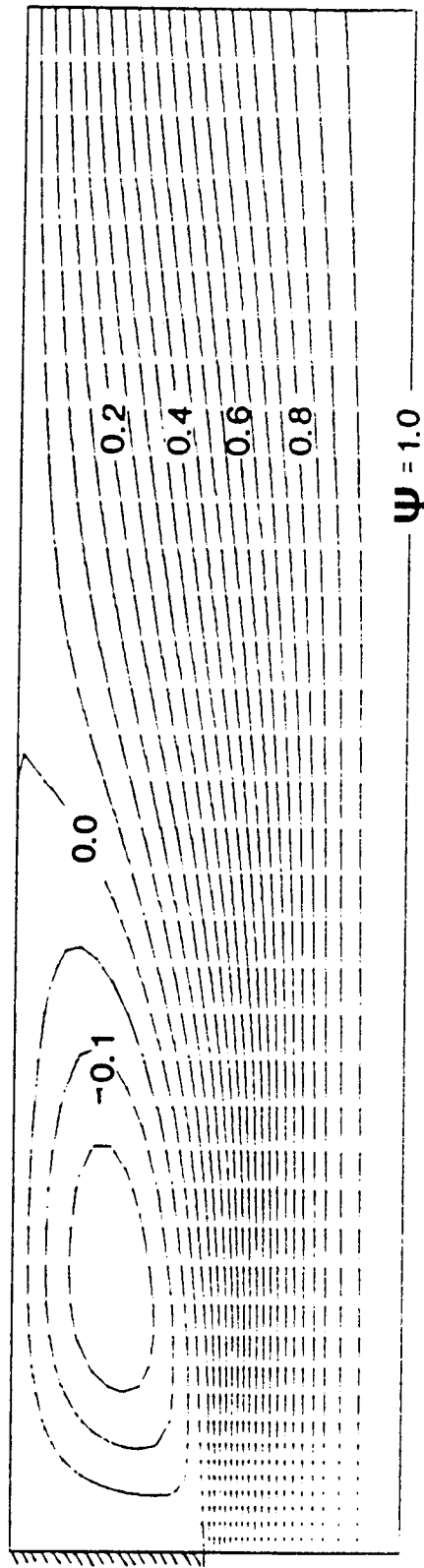
Figure 15. Streamlines of the flow in a sudden expansion
combustor
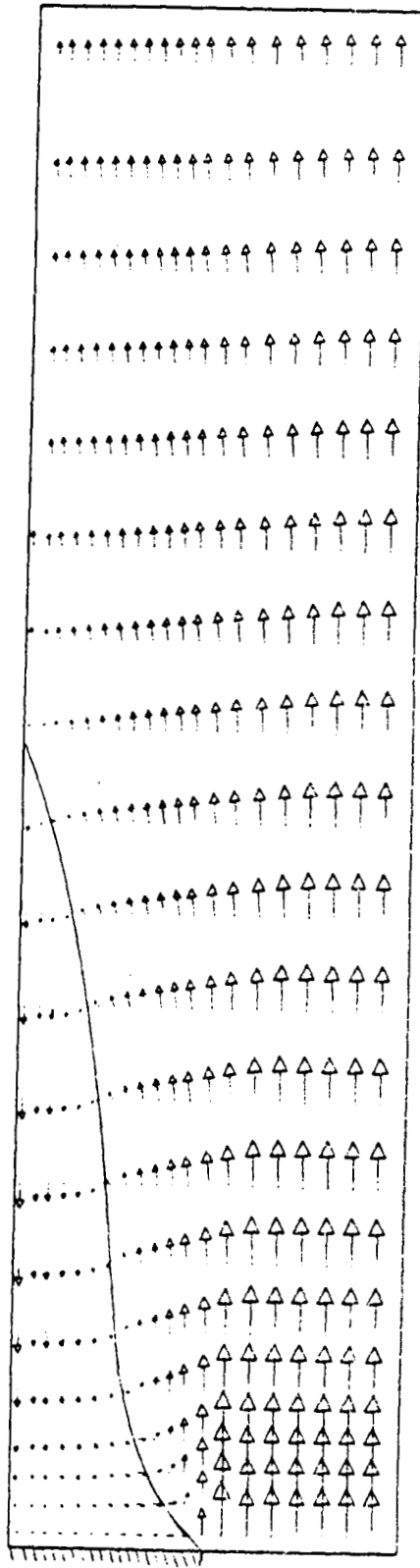
Figure 16. Velocity field in a sudden expansion combustor
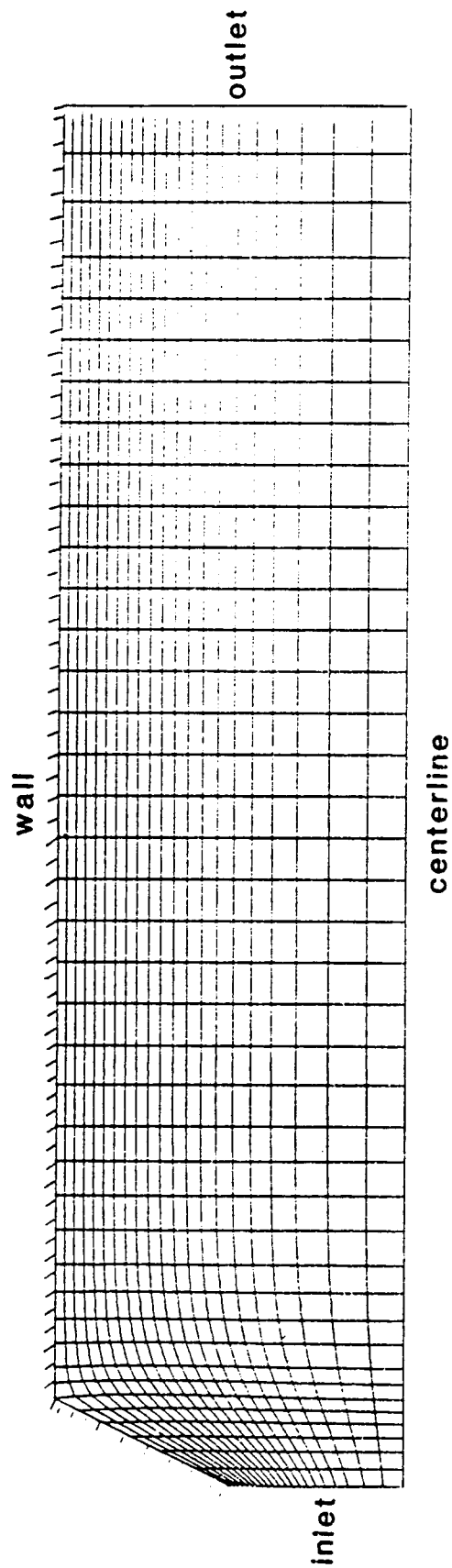
Figure 17. Grid point distribution I for a 45° expansion combustor
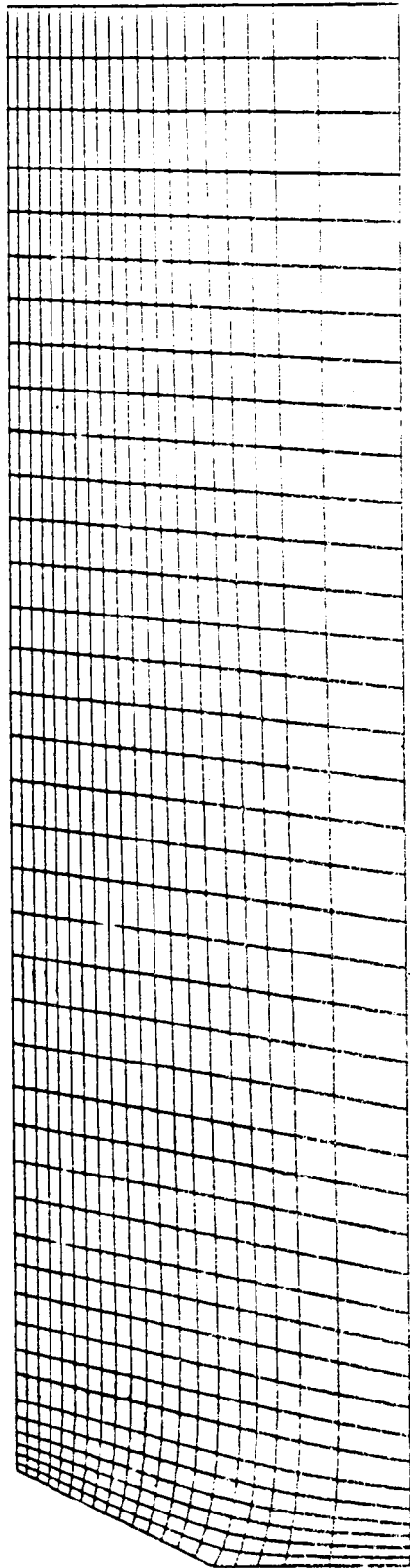
Figure 18. Grid point distribution II for a 45° expansion combustor
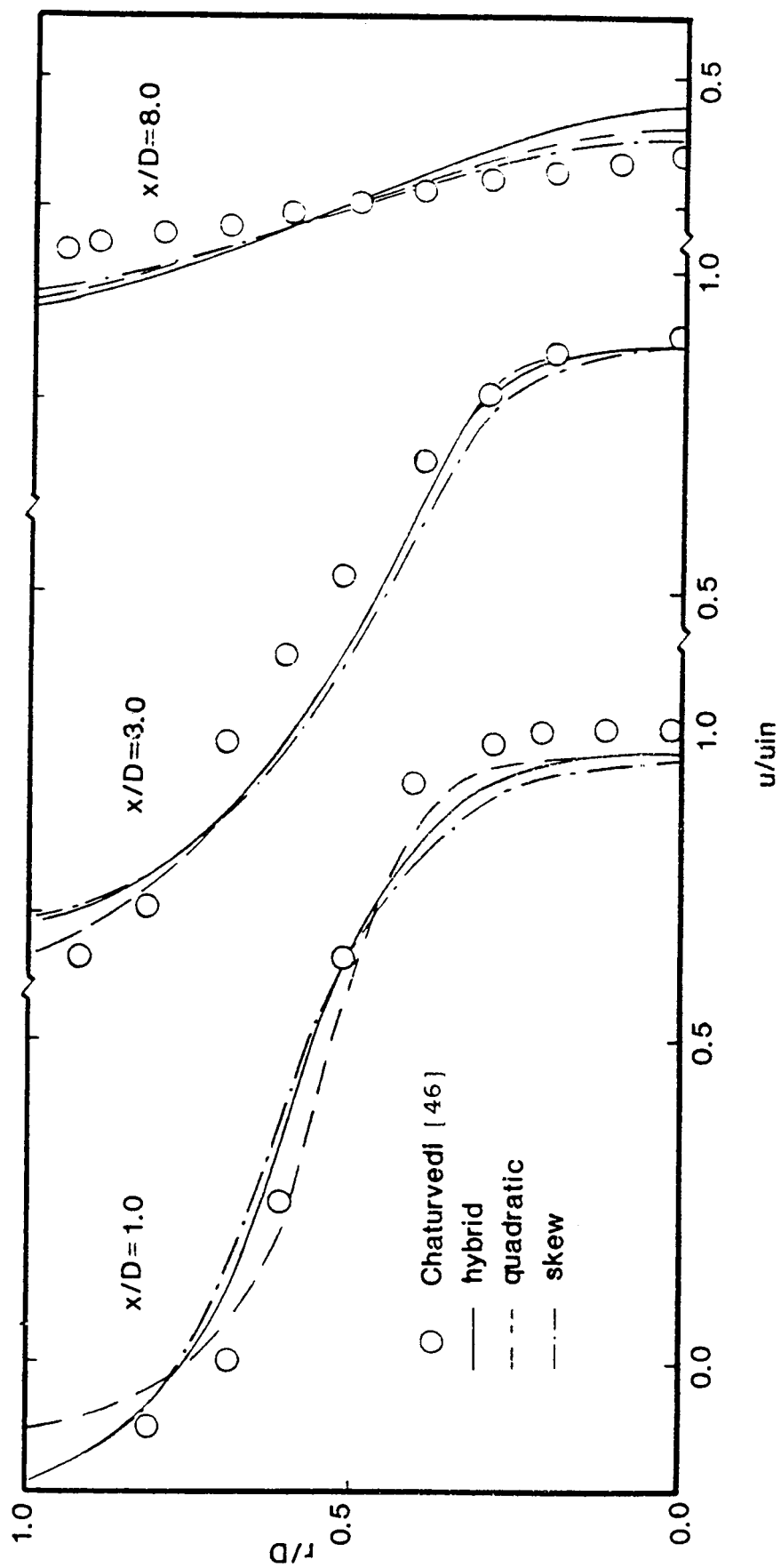
Figure 19. Axial velocity profiles at various axial
locations for flow in a 45° expansion combustor,
grid I
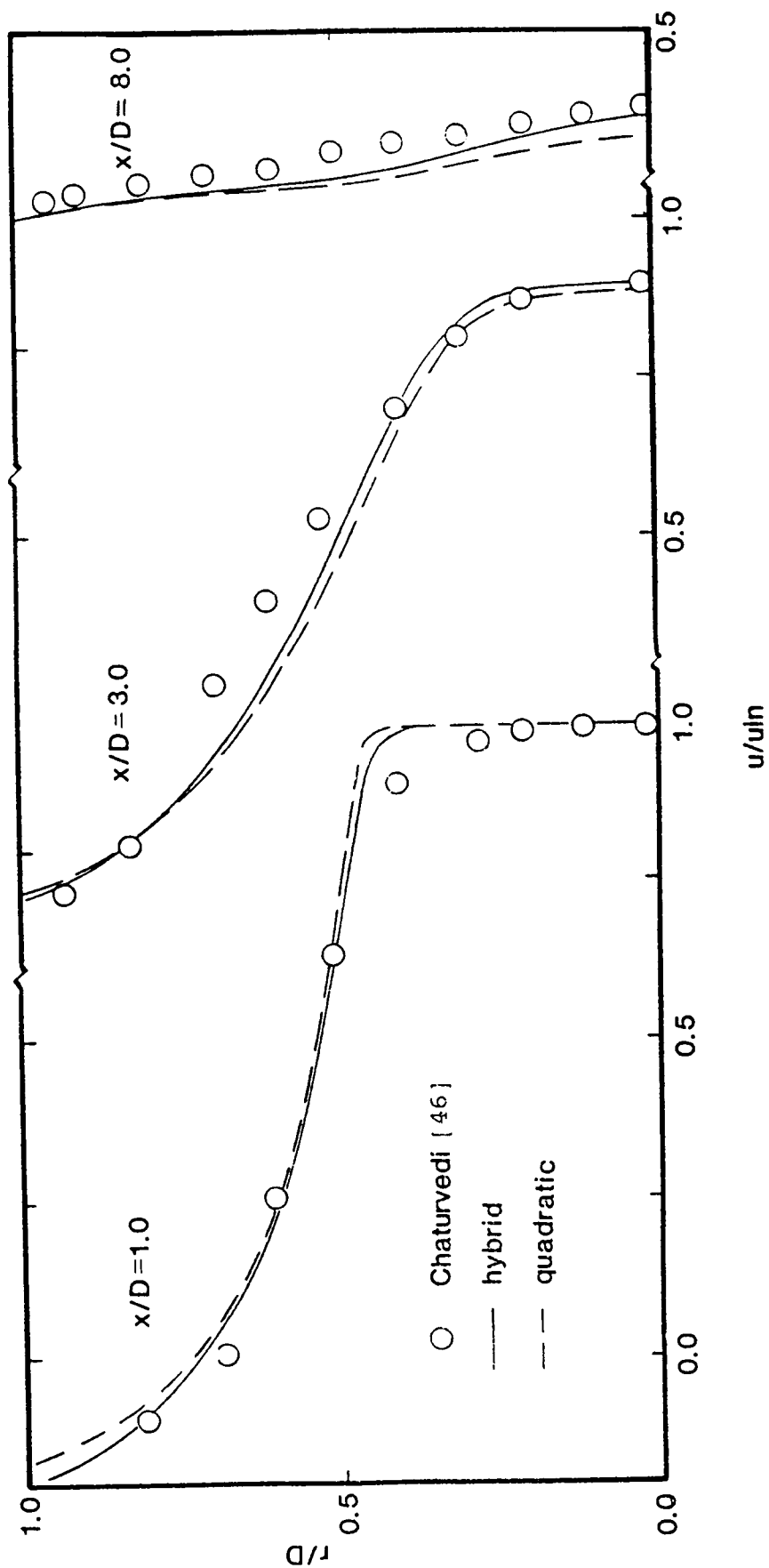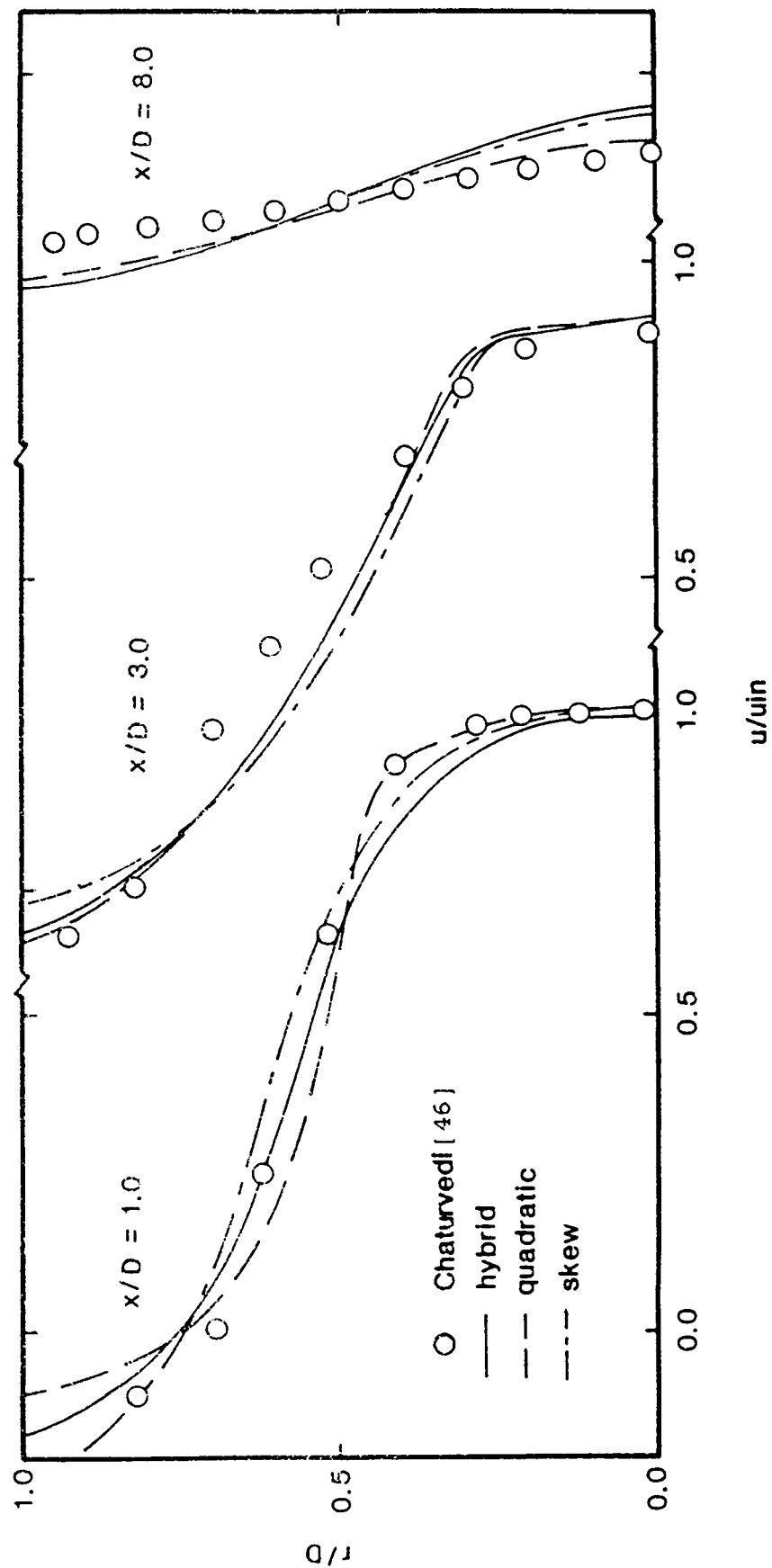
Figure 20. Axial velocity profiles at various axial locations for flow in a 45° expansion combustor, grid II
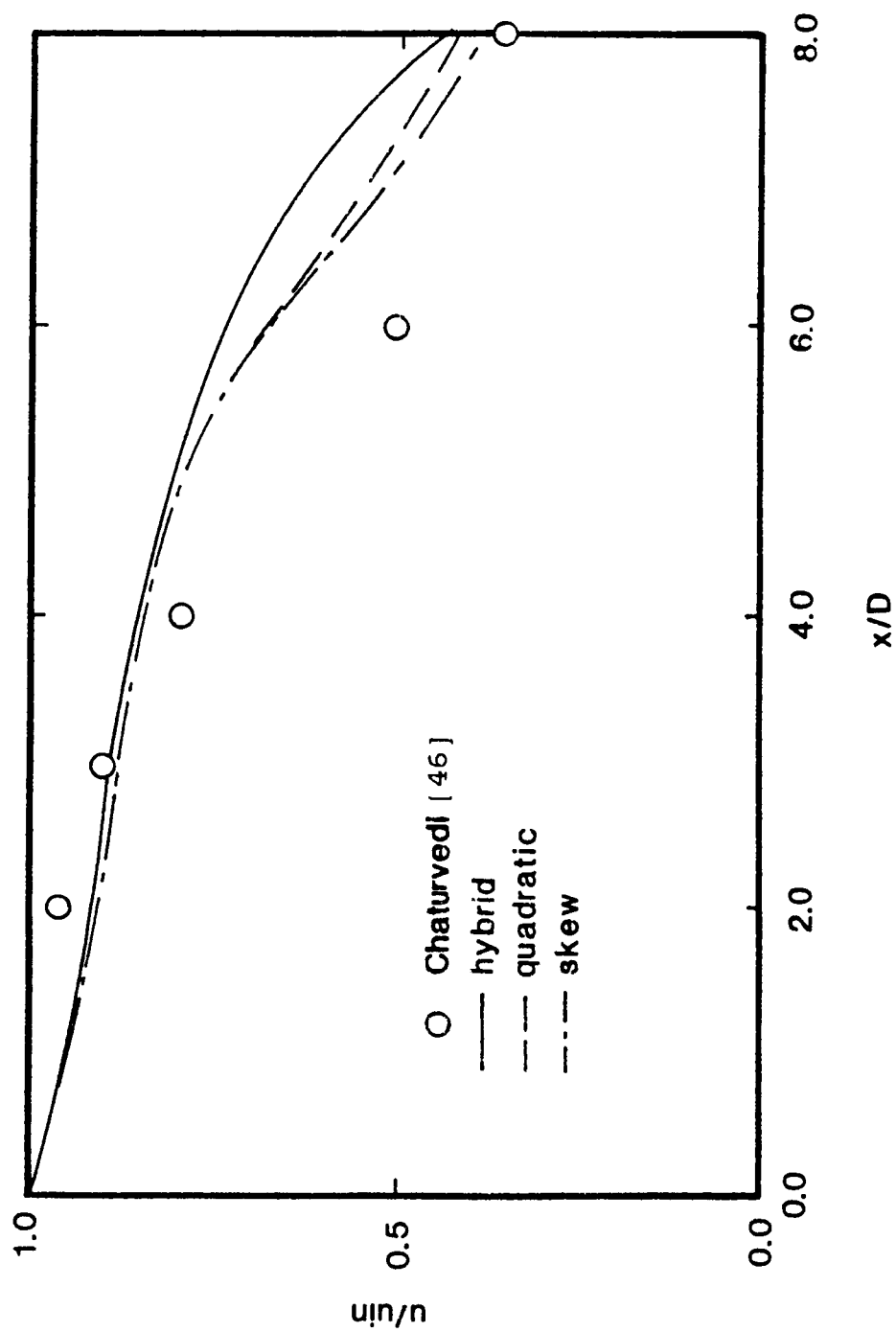
Figure 21. Centerline velocity for flow in a 45° expansion combustor, grid I
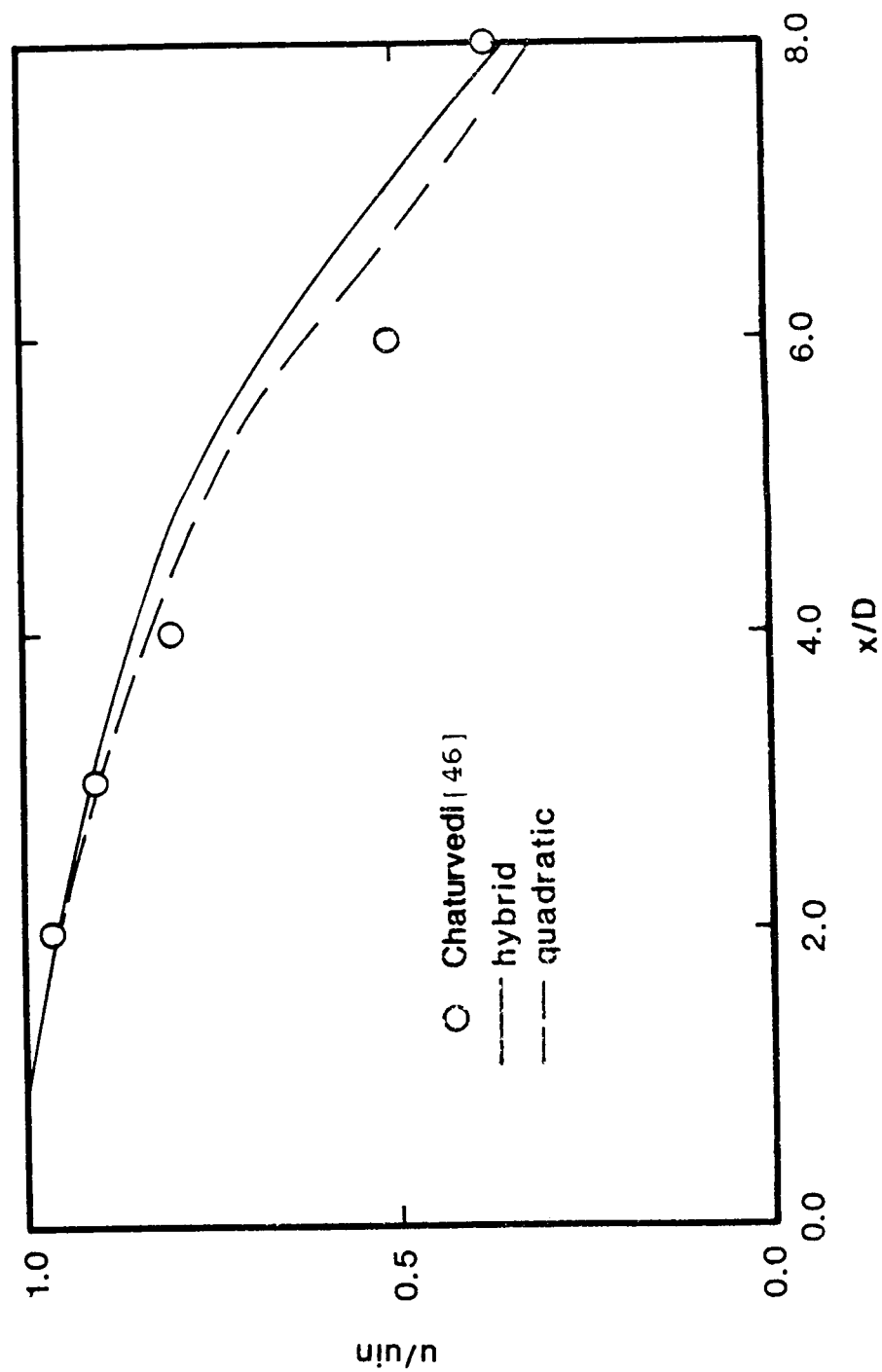
Figure 22. Centerline velocity for flow in a 45° expansion combustor, grid II
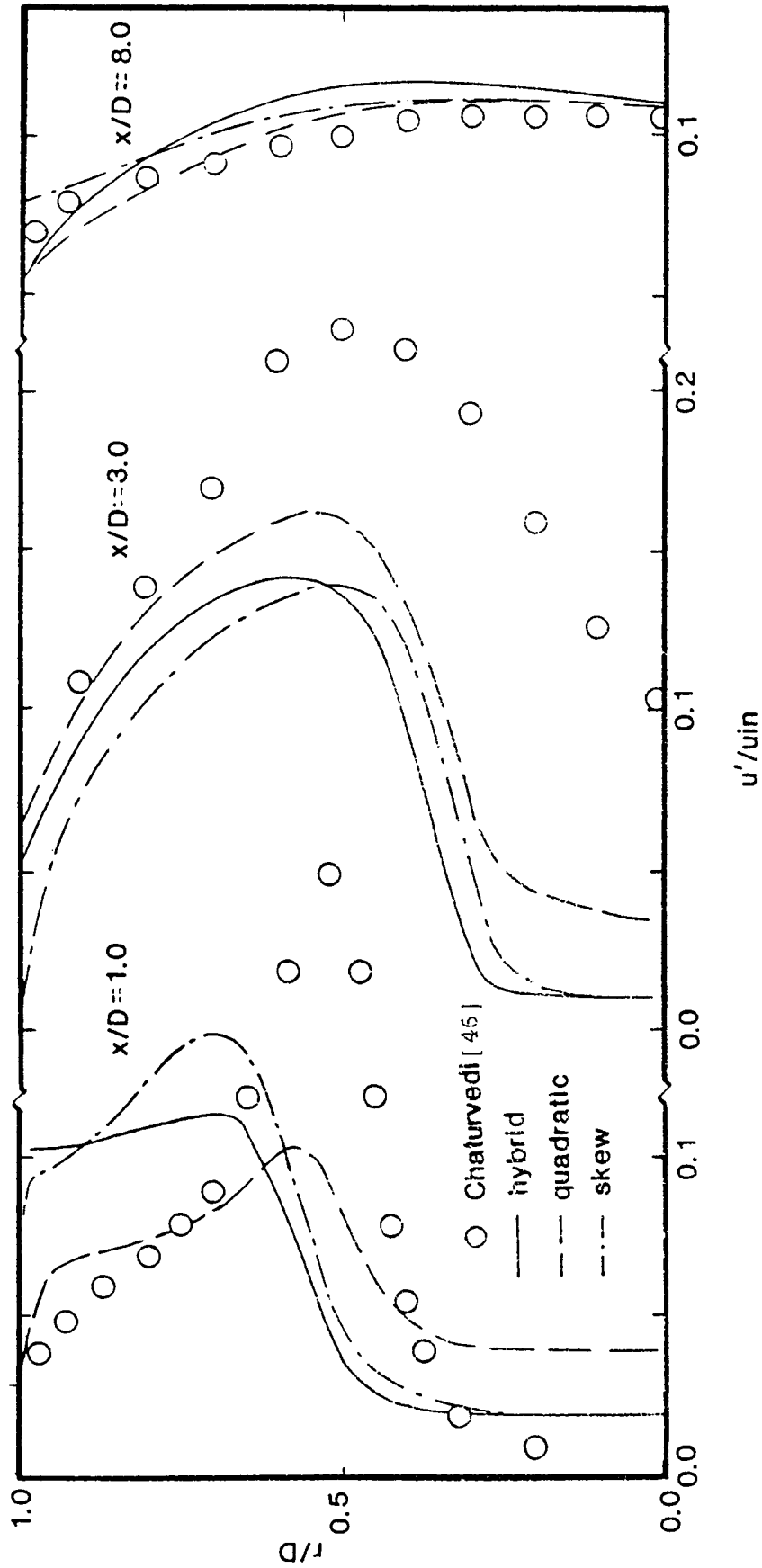
Figure 23. Turbulence intensity profiles at various axial
locations for flow in a 45° expansion combustor,
grid I
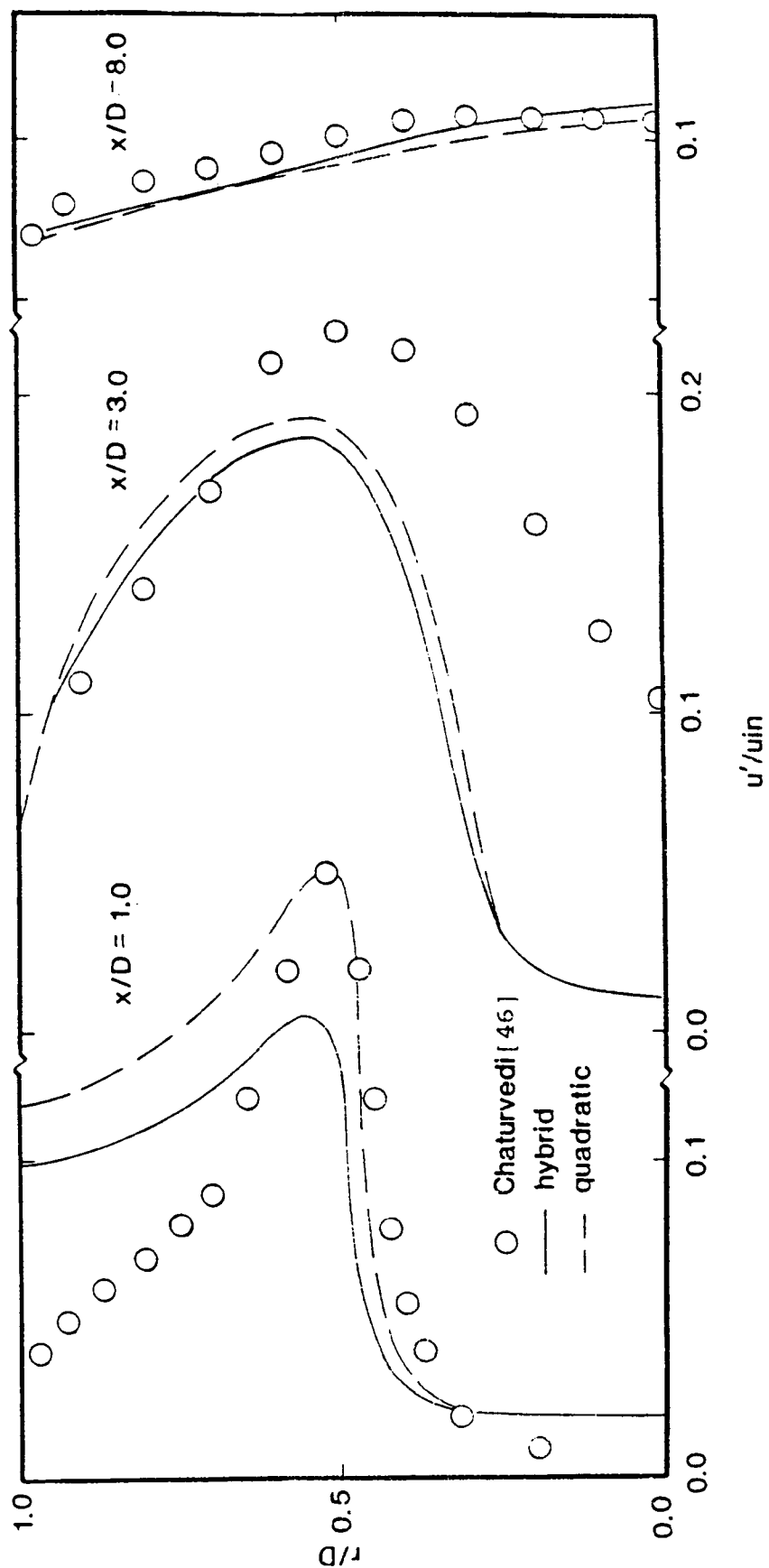
Figure 24. Turbulence intensity profiles at various axial
locations for flow in a 45° expansion combustor,
grid II

120
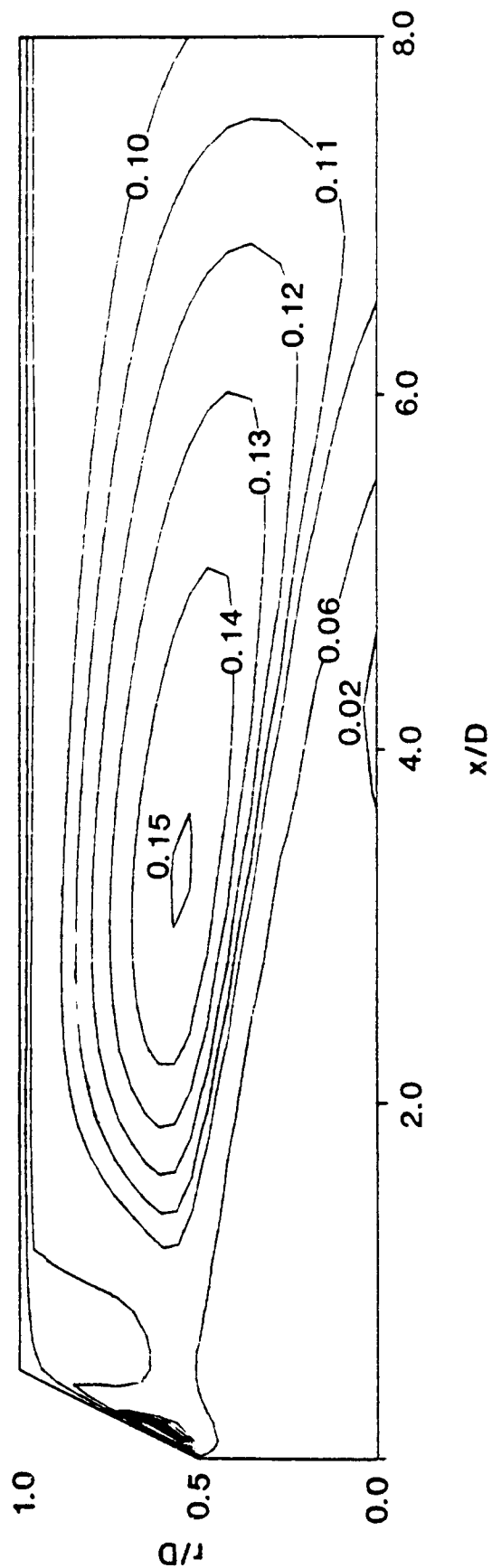
Figure 25. Turbulence intensity contours for flow in a 45° expansion combustor, grid I

121
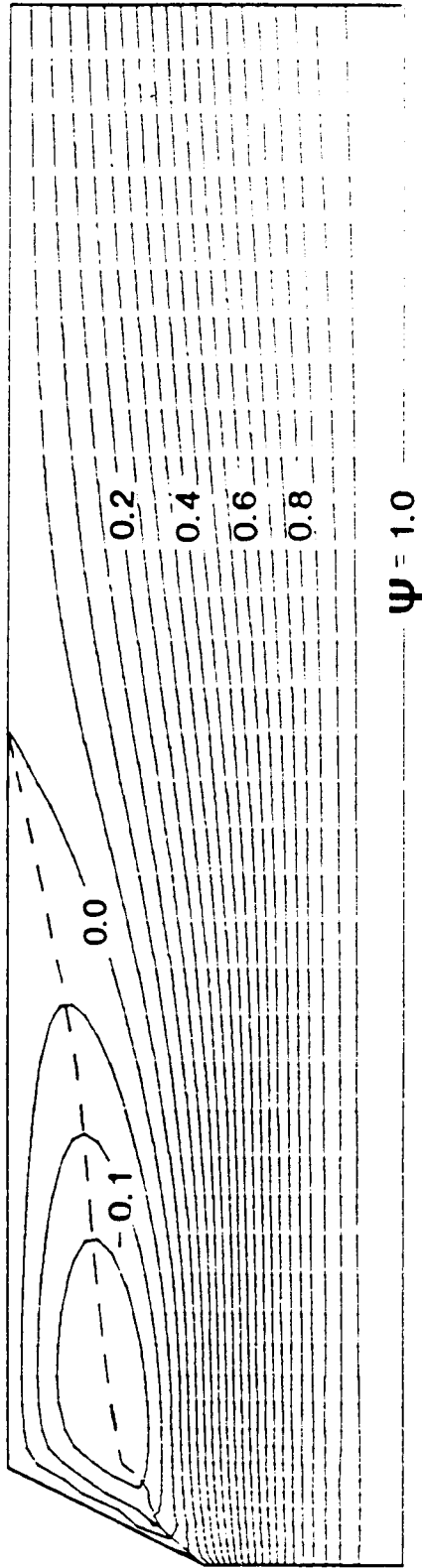
Figure 26. Streamlines of the flow in a 45° expansion combustor, grid I
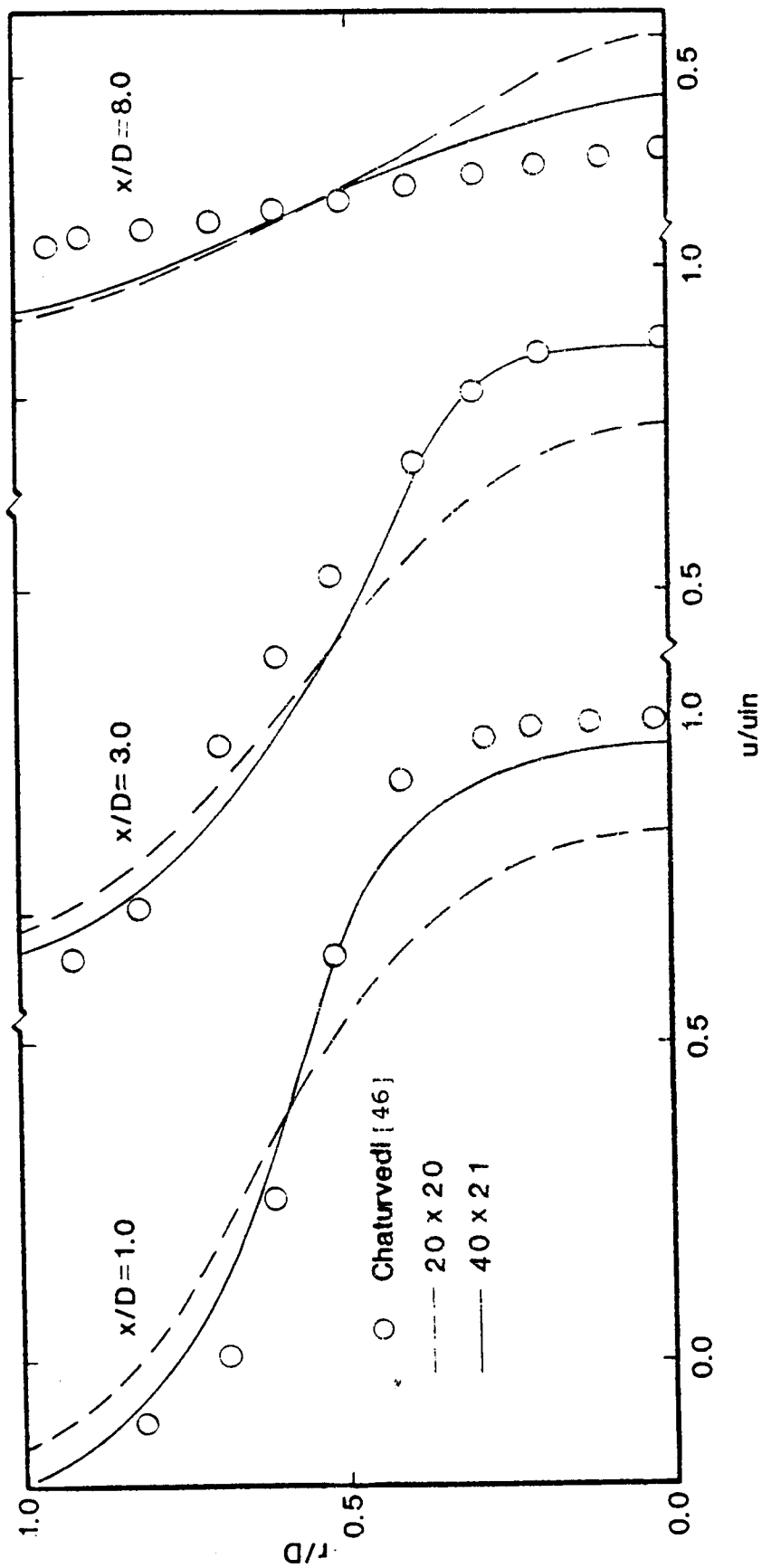
Figure 27. Axial velocity profiles at various axial locations for two grids, 40x21 and 20x20
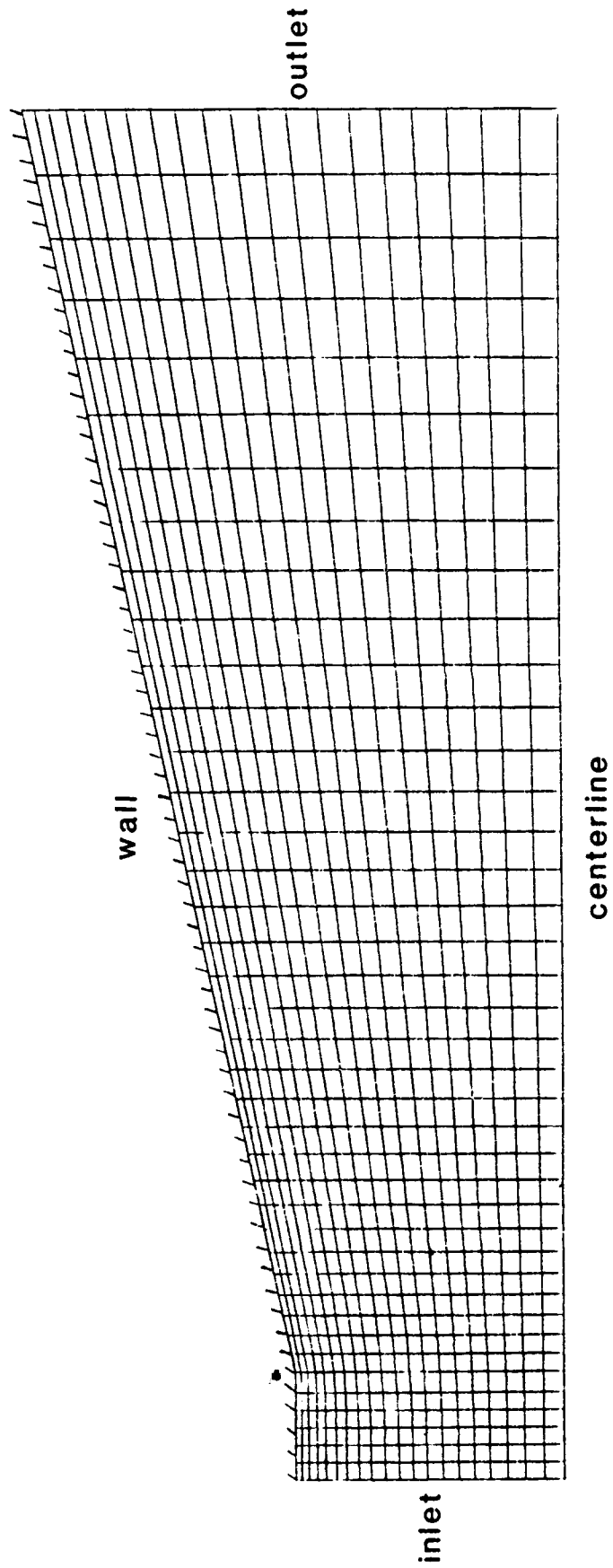
Figure 28. Grid distribution for a conical diffuser
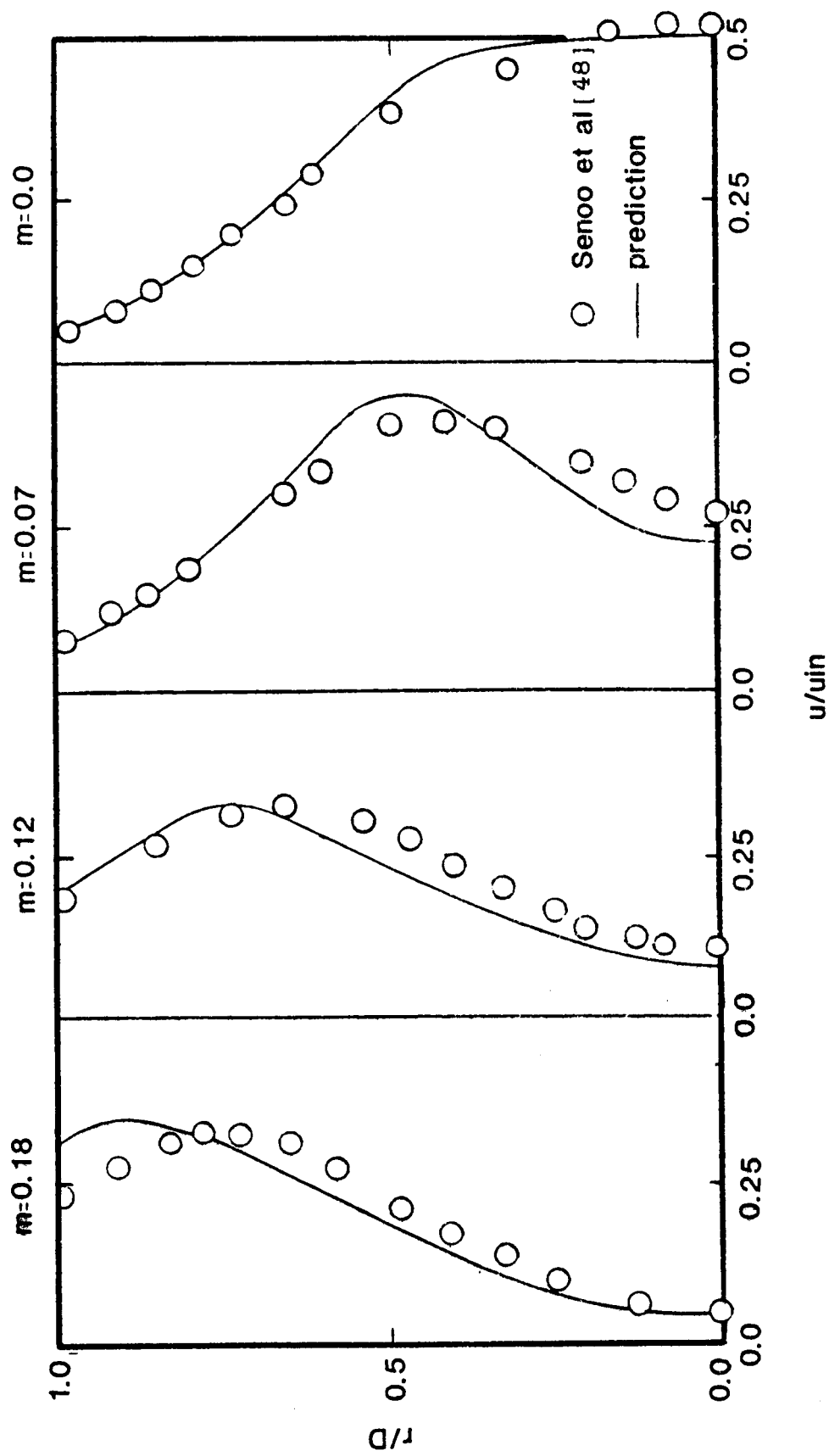
Figure 29. Axial velocity profiles at the outlet of a conical diffuser for various swirl intensities
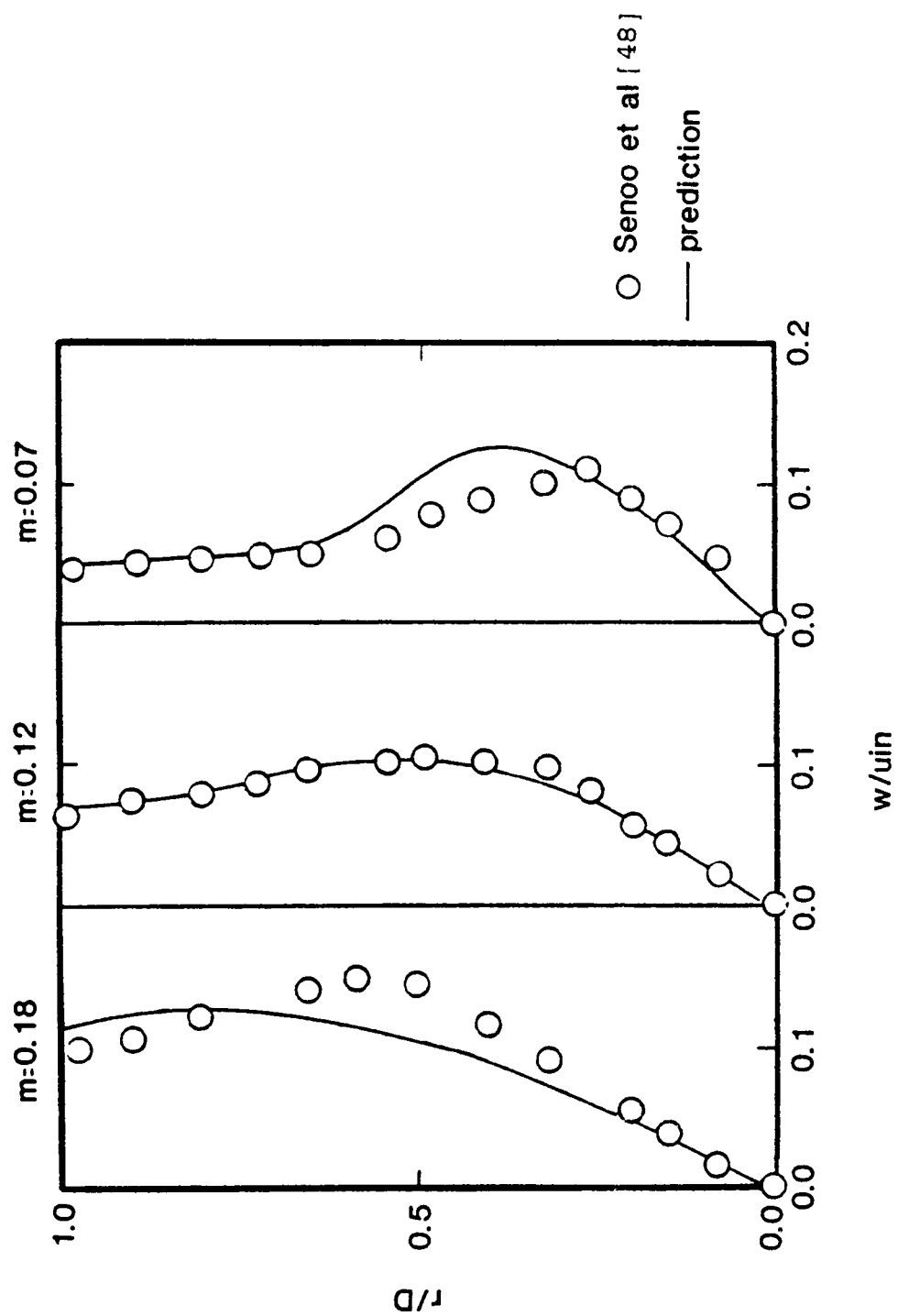
Figure 30. Circumferential velocity profiles at the outlet of a conical diffuser for various swirl intensities
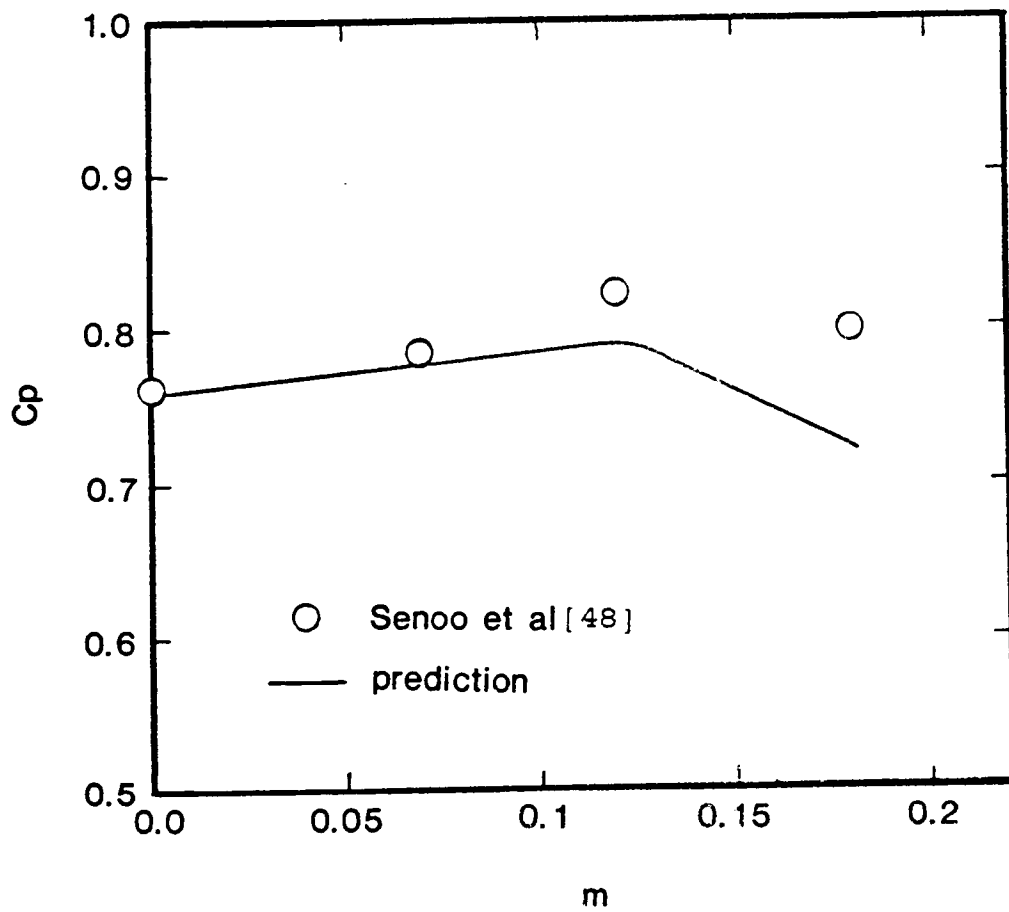
Figure 31. Variation of pressure recovery coefficient with swirl intensity for a conical diffuser
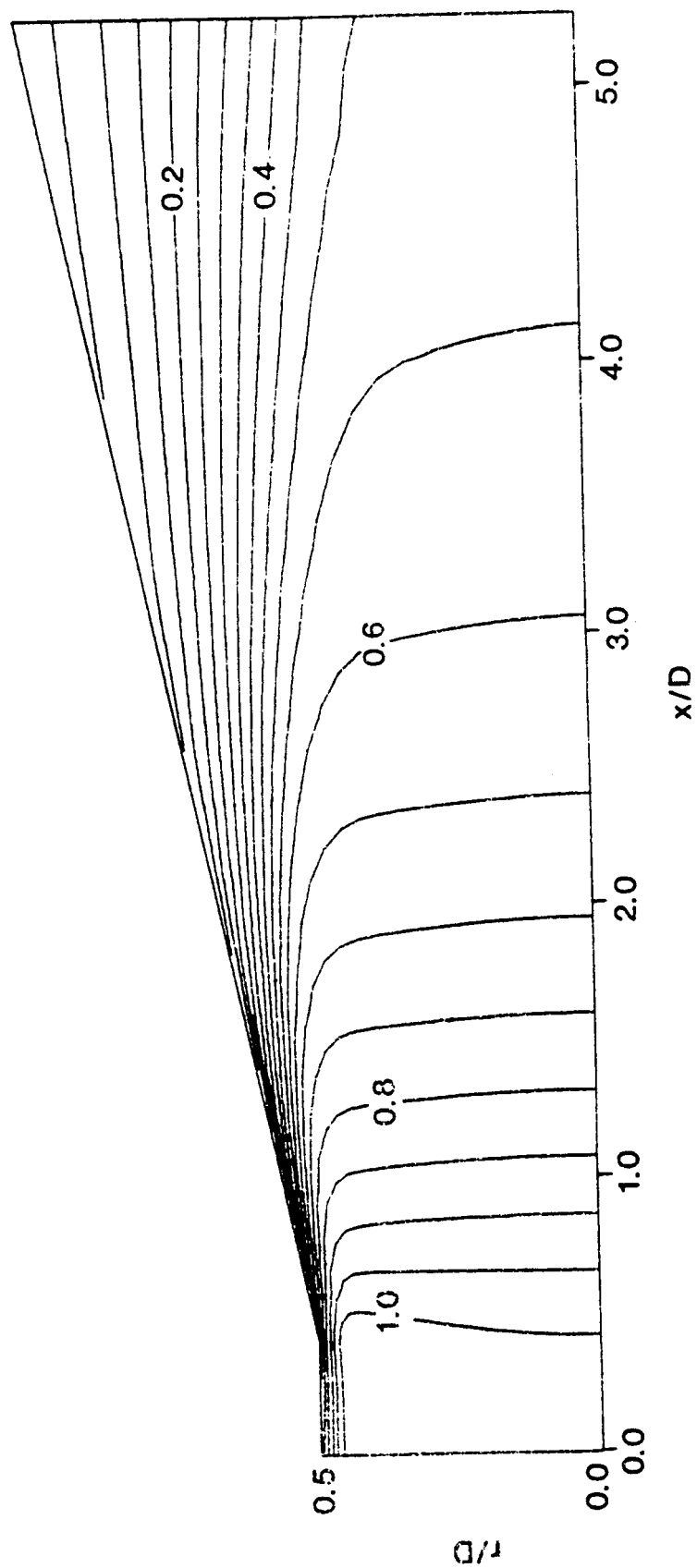
Figure 32. Axial velocity contours for flow in a conical
diffuser without swirl, m =0.0
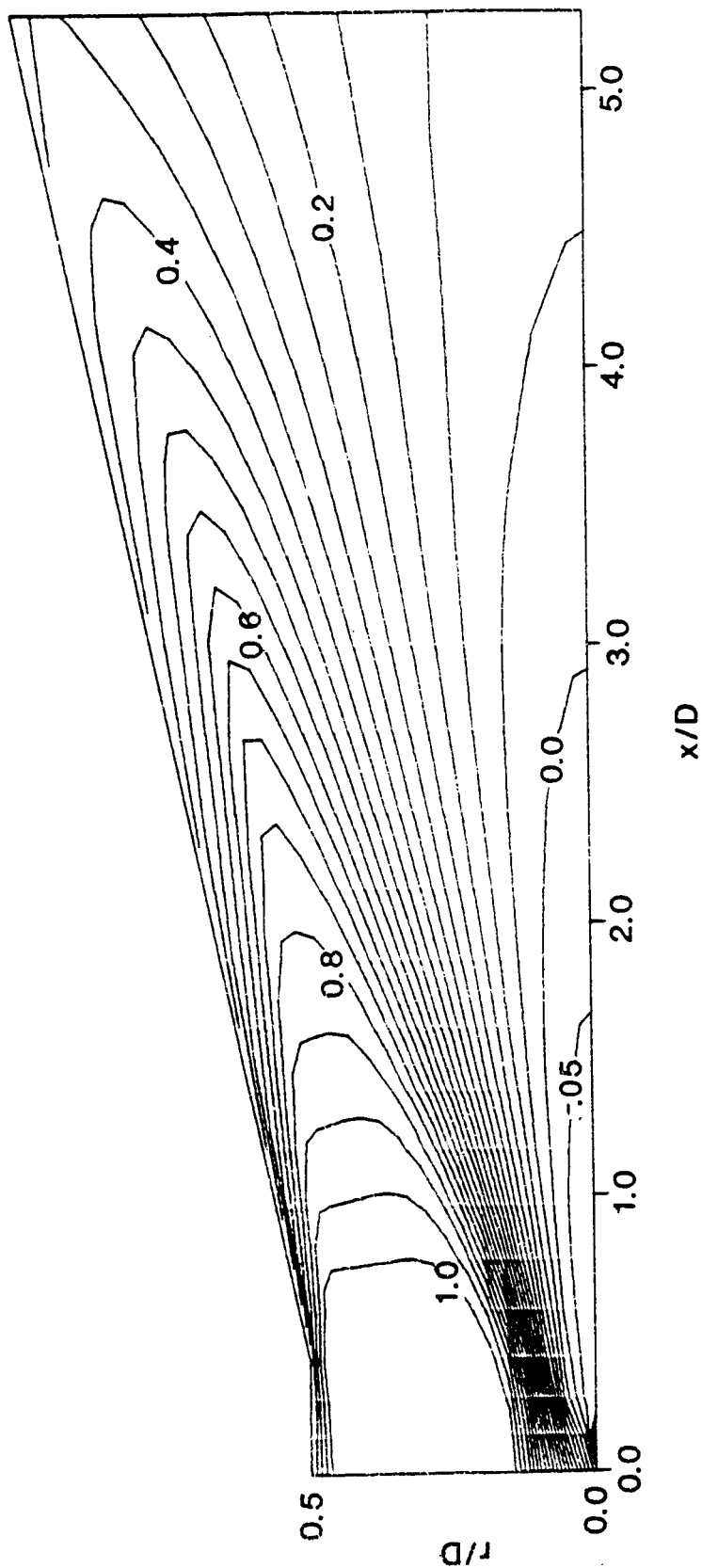
Figure 33. Axial velocity contours for flow in a conical diffuser with swirl, m = 0.18
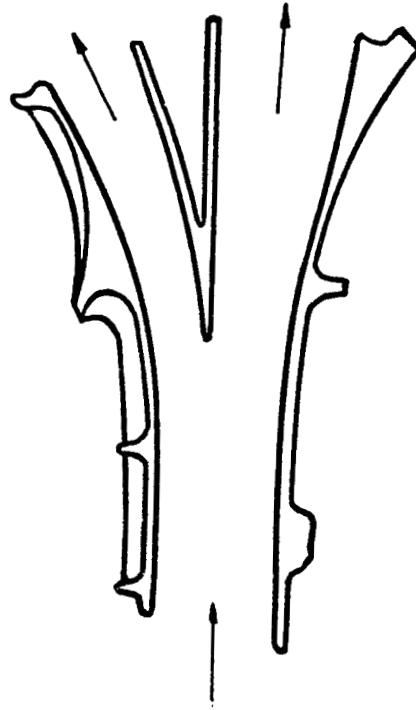
Figure 34. Schematic diagram of a bifurcated diffuser
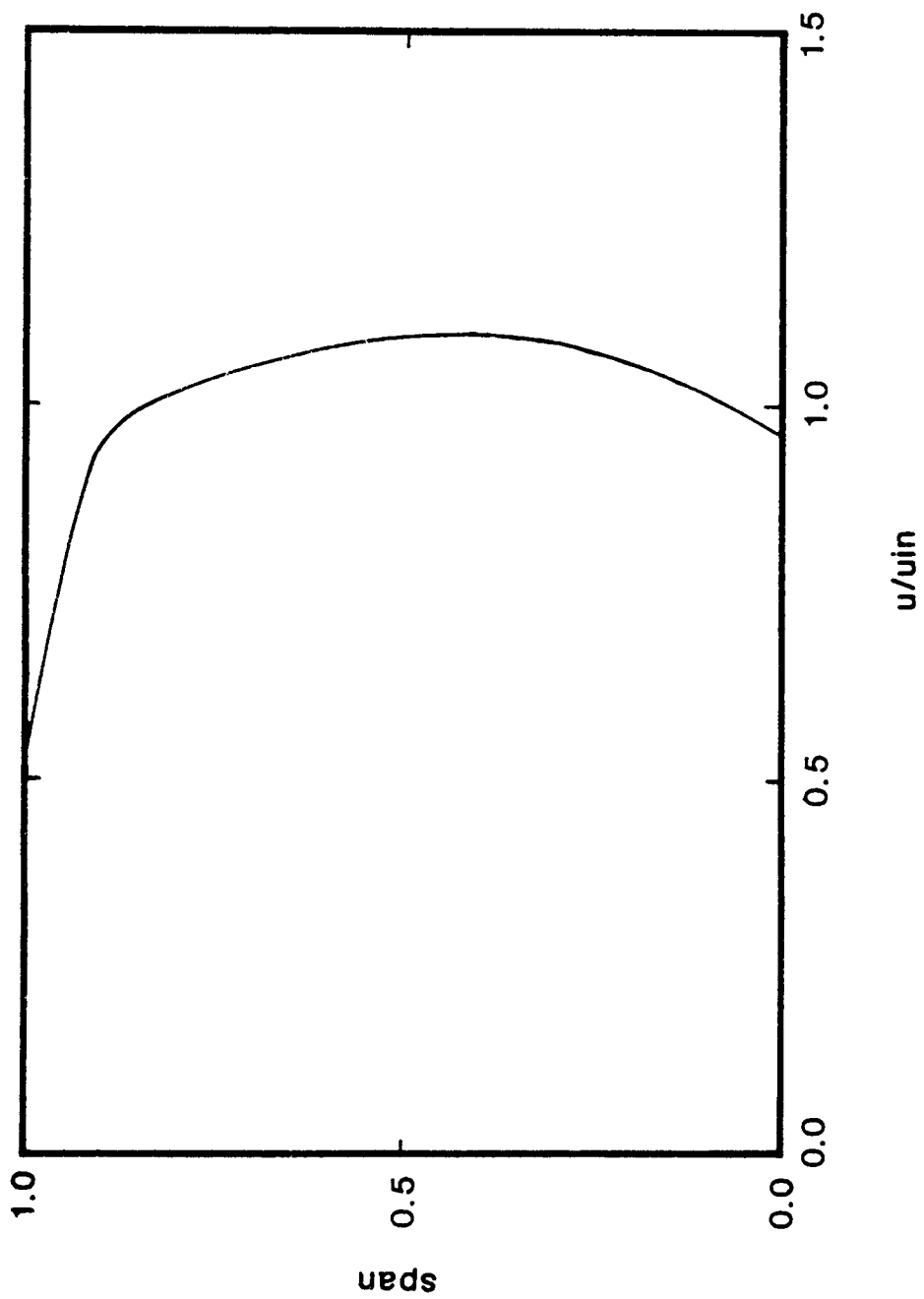
Figure 35. Inlet velocity profile for flow in a bifurcated diffuser
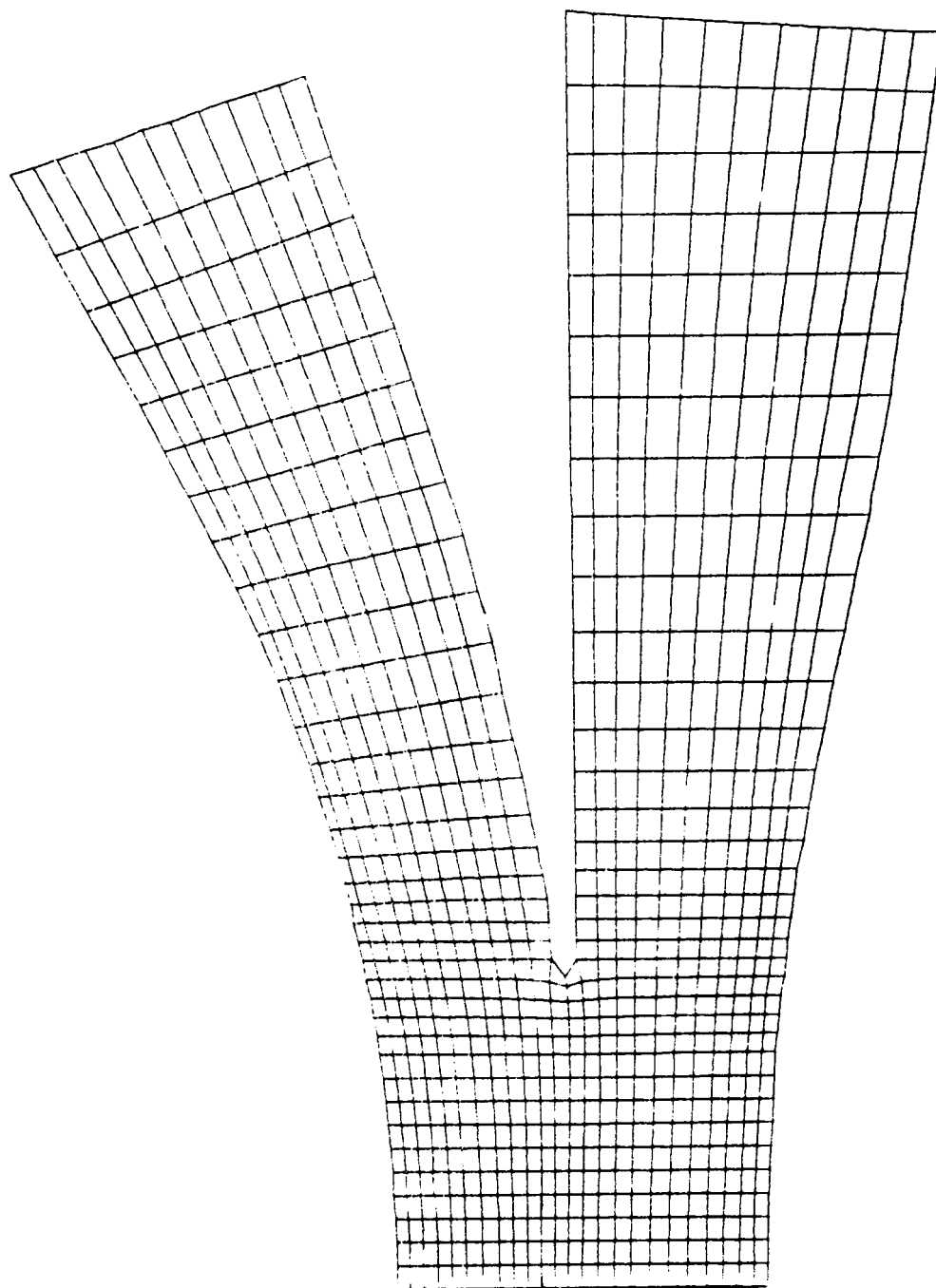
Figure 36. Grid point distribution for a bifurcated diffuser
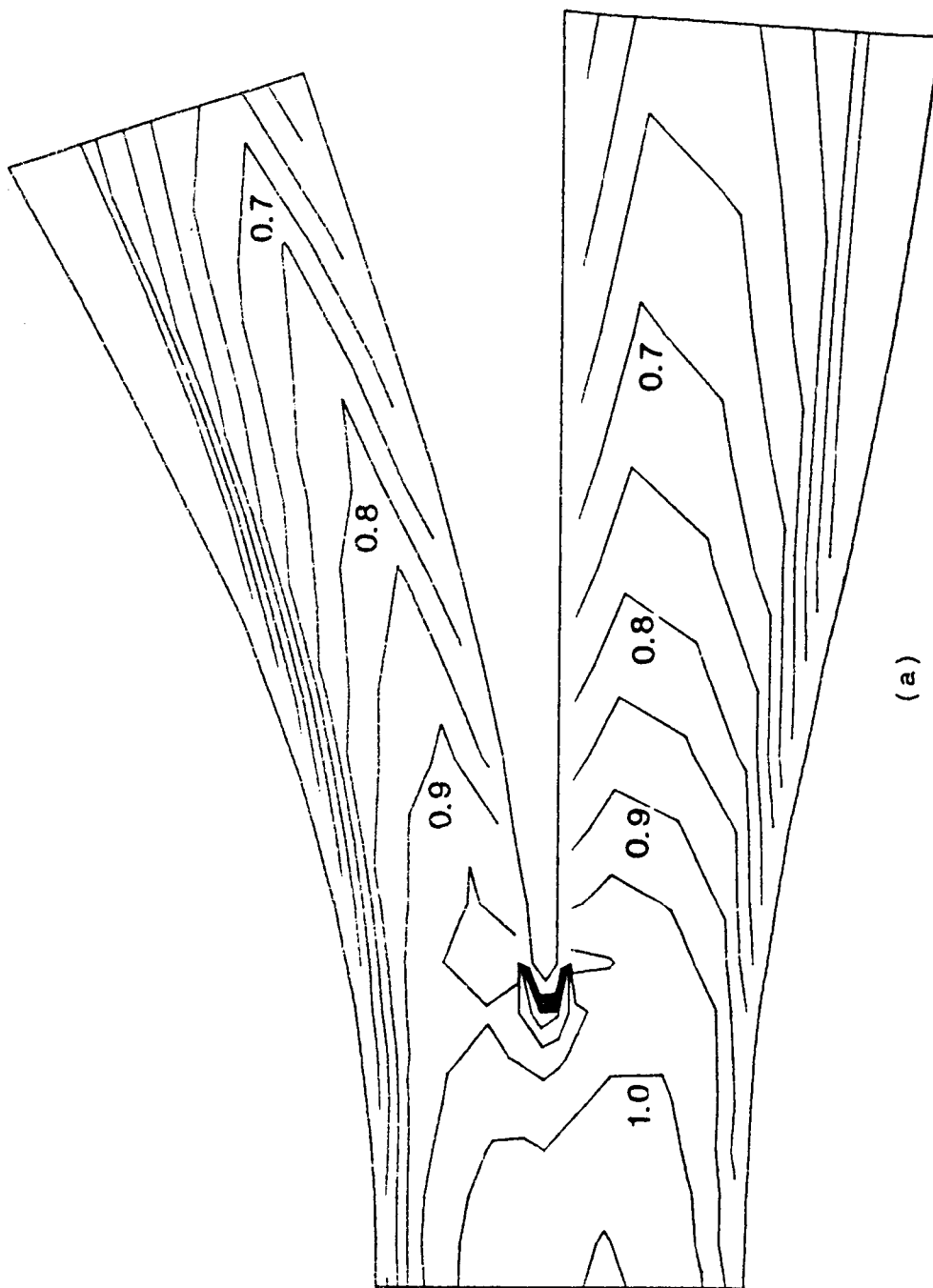
Figure 37. Axial velocity contours for flow in a bifurcated diffuser, computed on a 17x13 mesh: (a) hybrid scheme; (b) skew upwind scheme; (c) quadratic upwind scheme

(a)
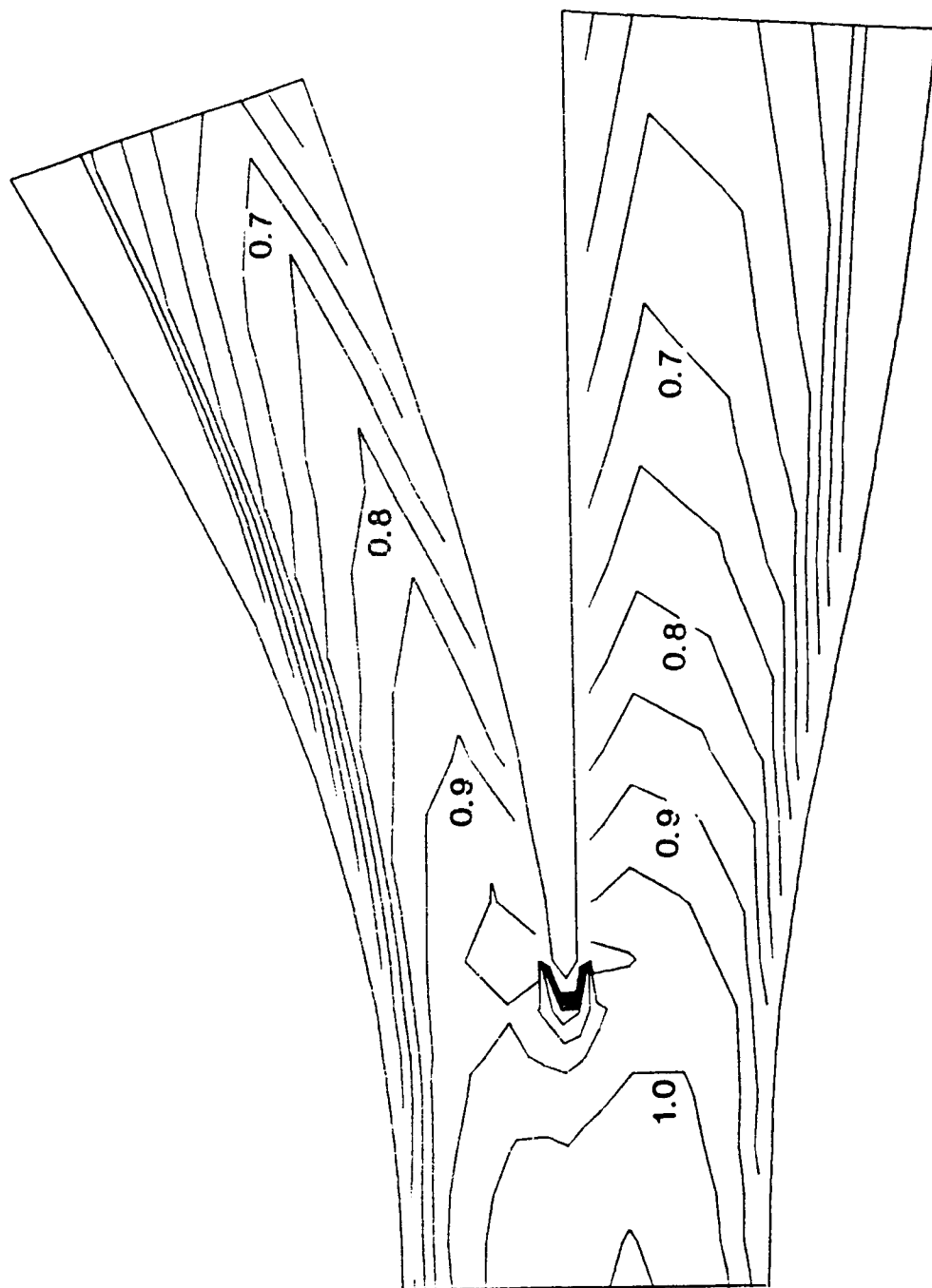
37(b)
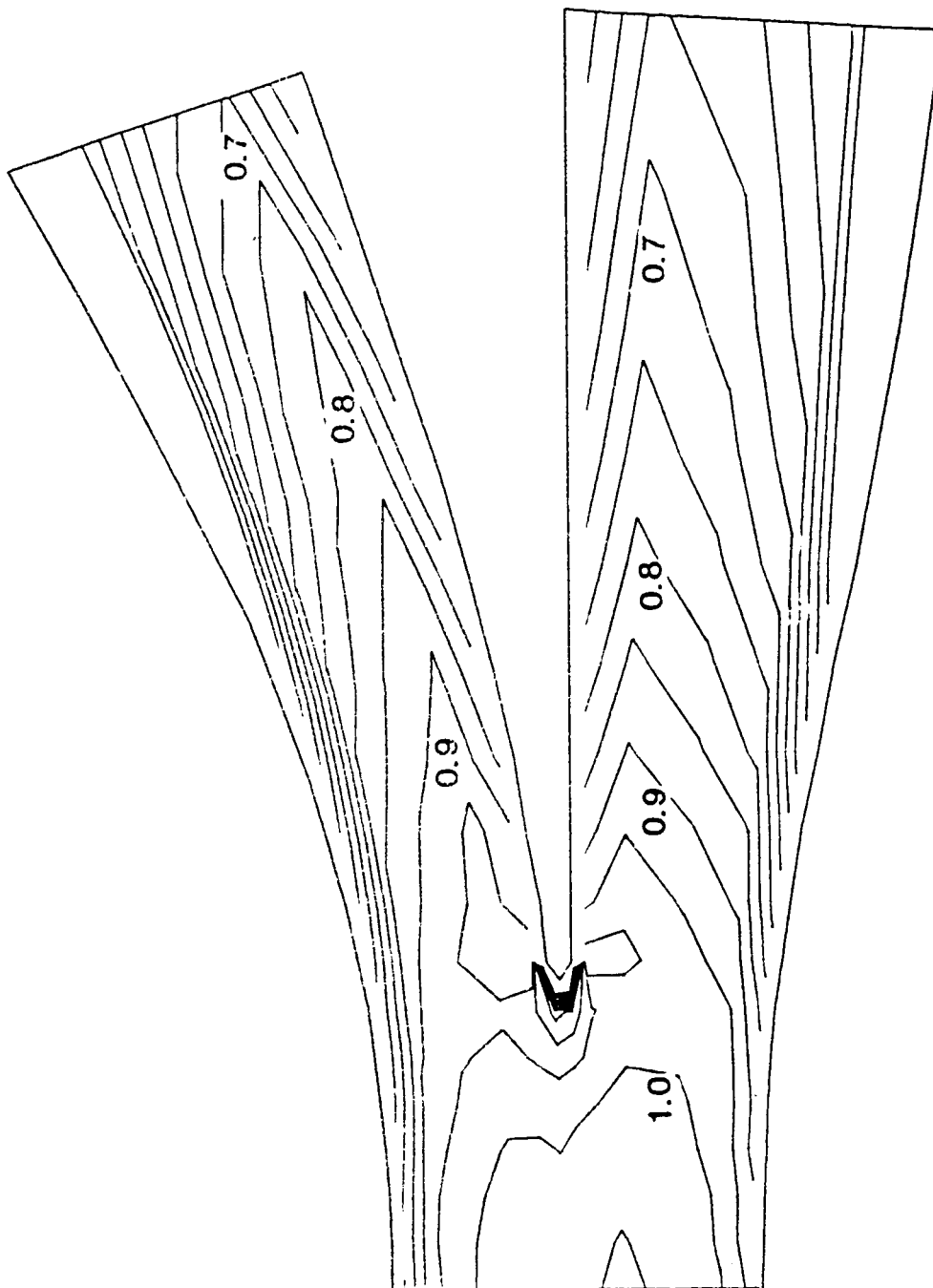
37(c)
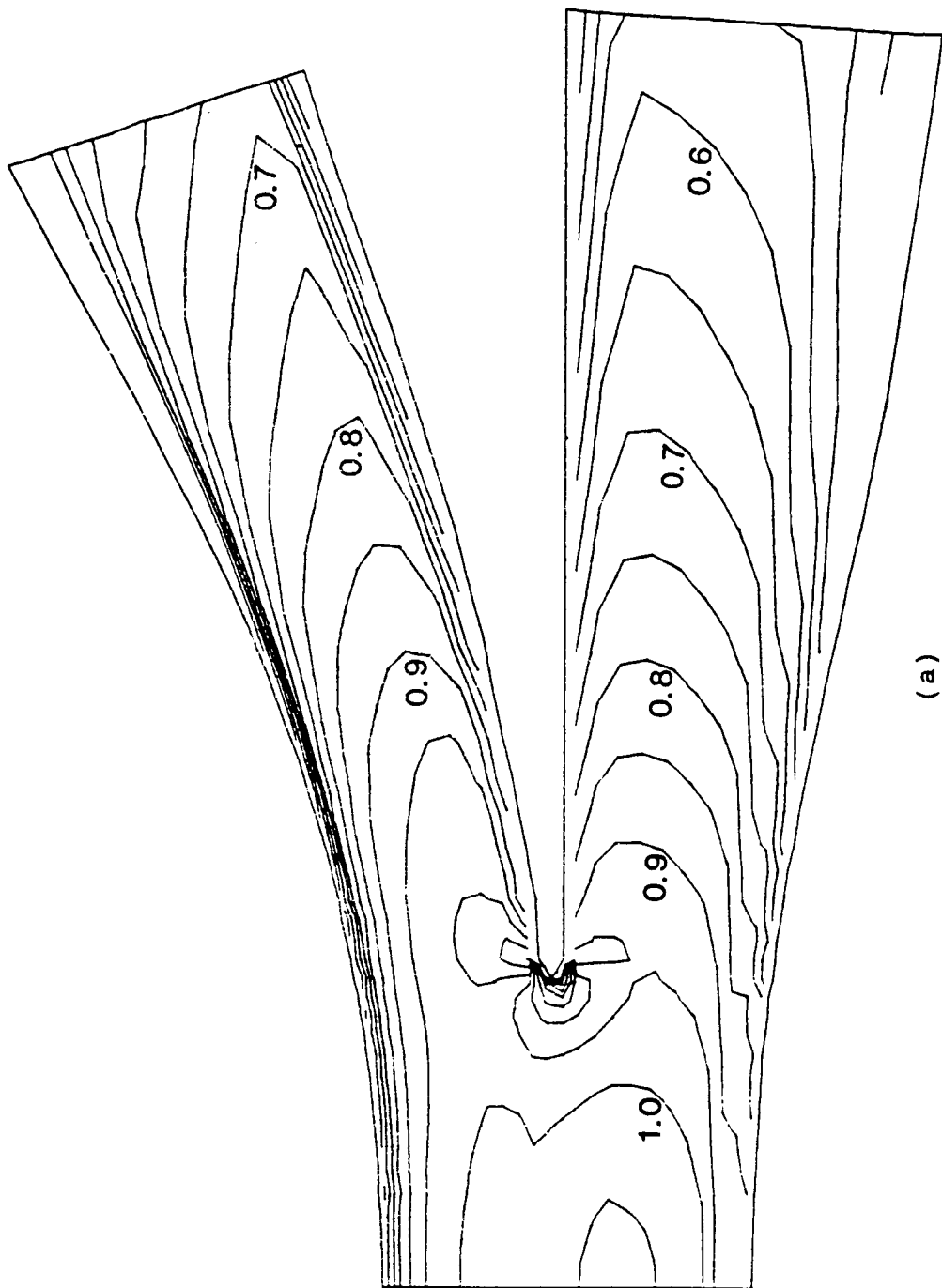
Figure 38. Axial velocity contours for flow in a bifurcated diffuser, computed on a 36x25 mesh: (a) hybrid scheme; (b) skew upwind scheme; (c) quadratic upwind scheme

(a)
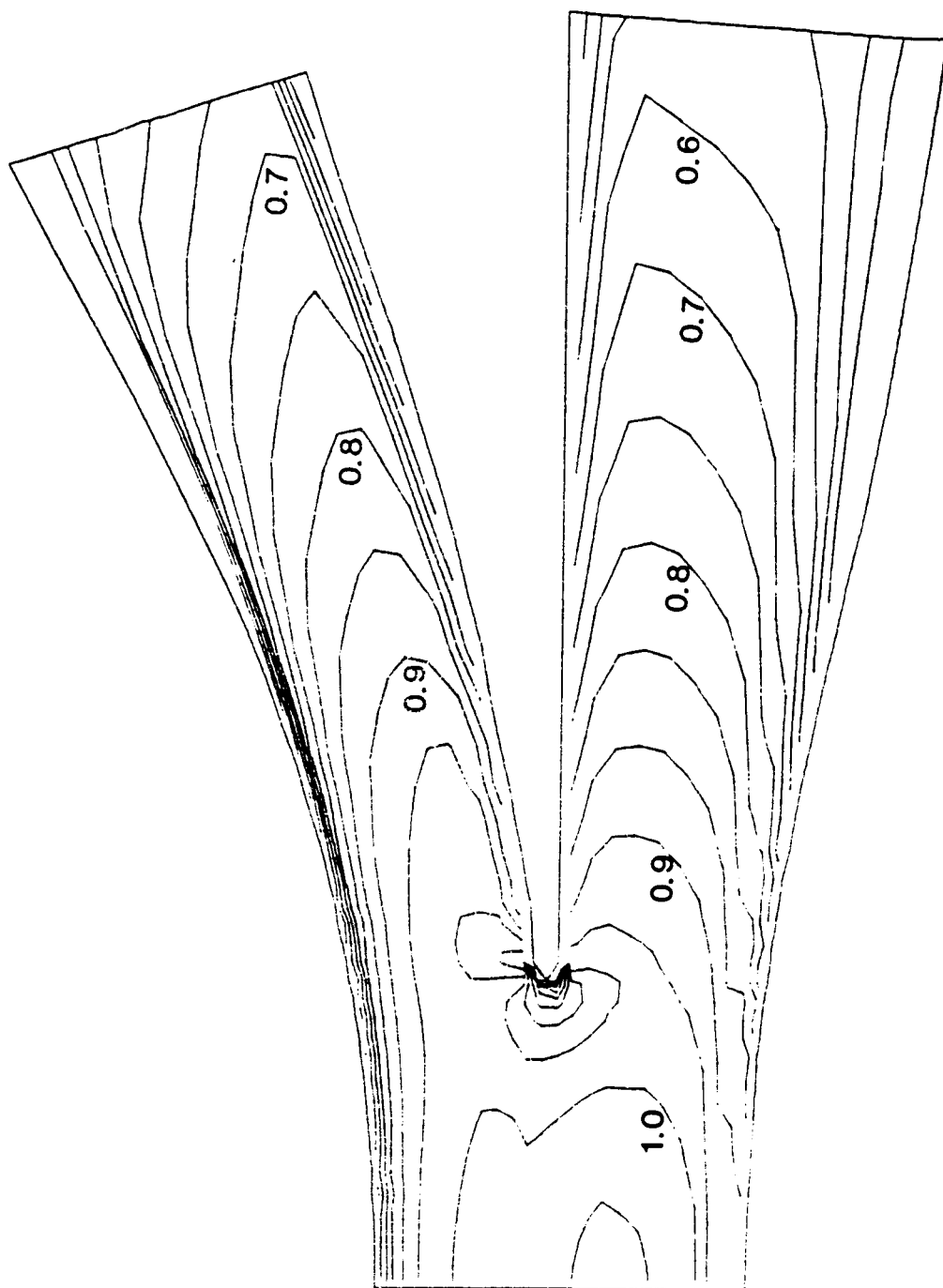
38(b)
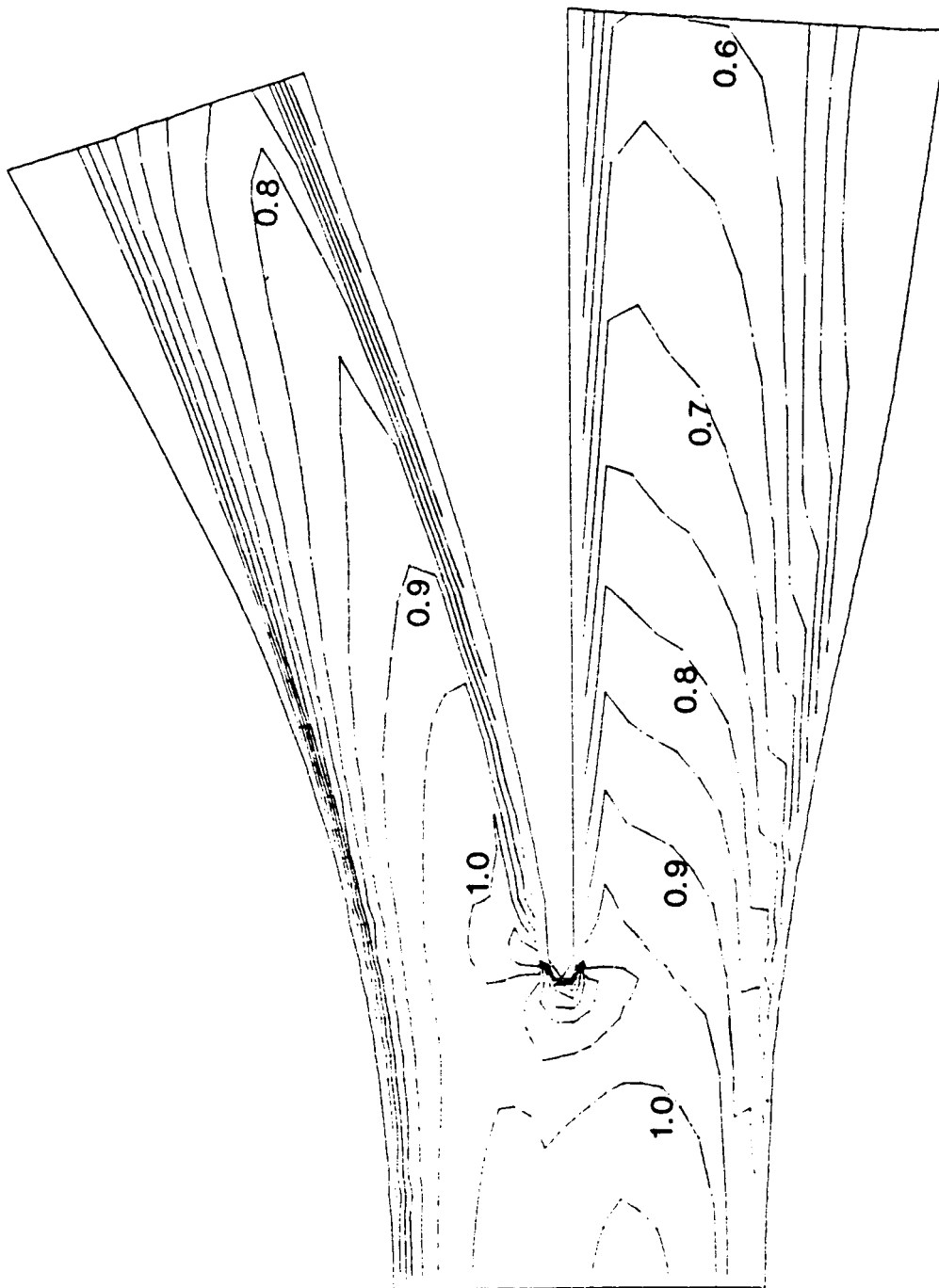
38(c)
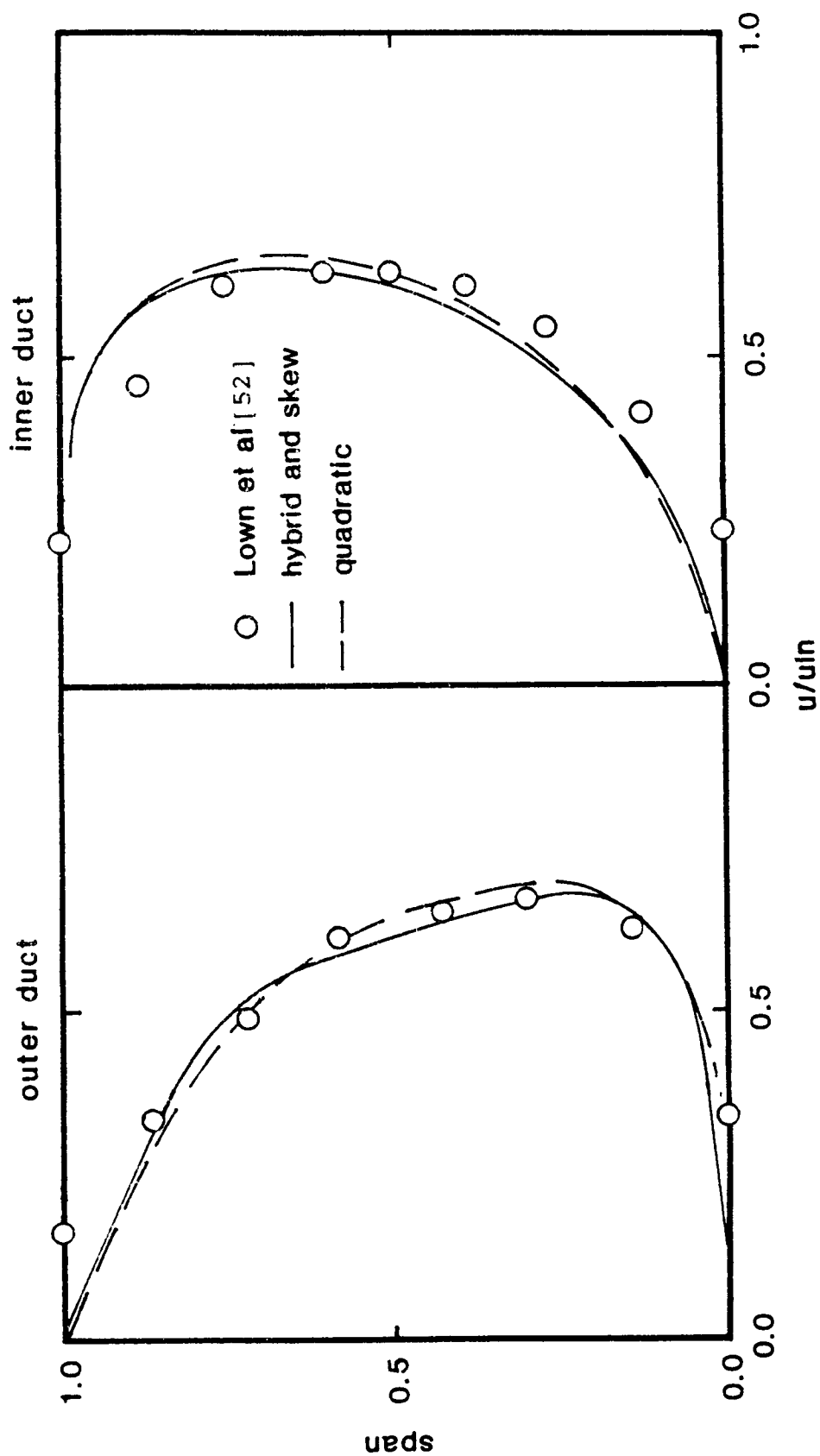
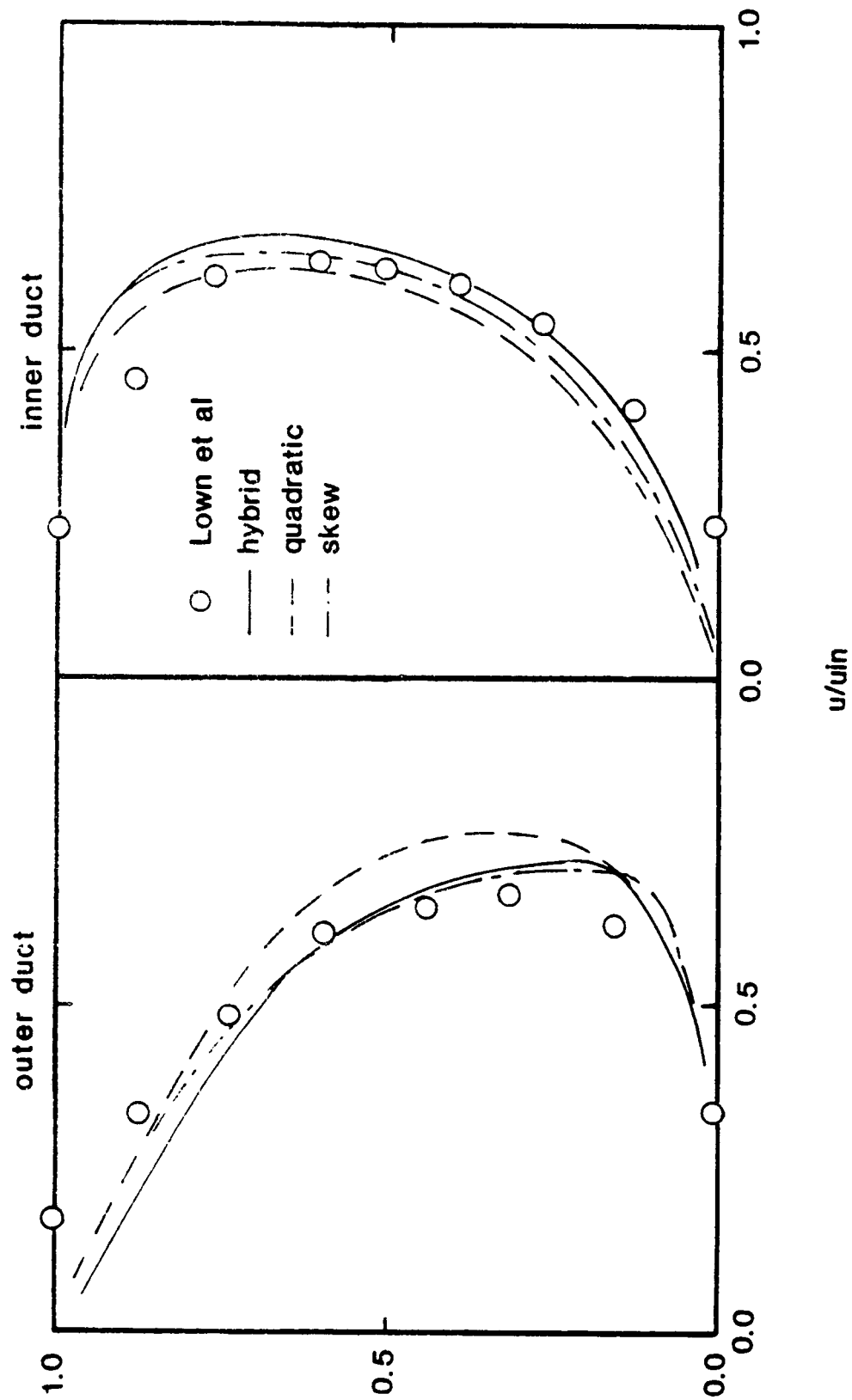Figure 39. Axial velocity profiles at the outlet of a bifurcated diffuser, computed on a 17x13 mesh

139
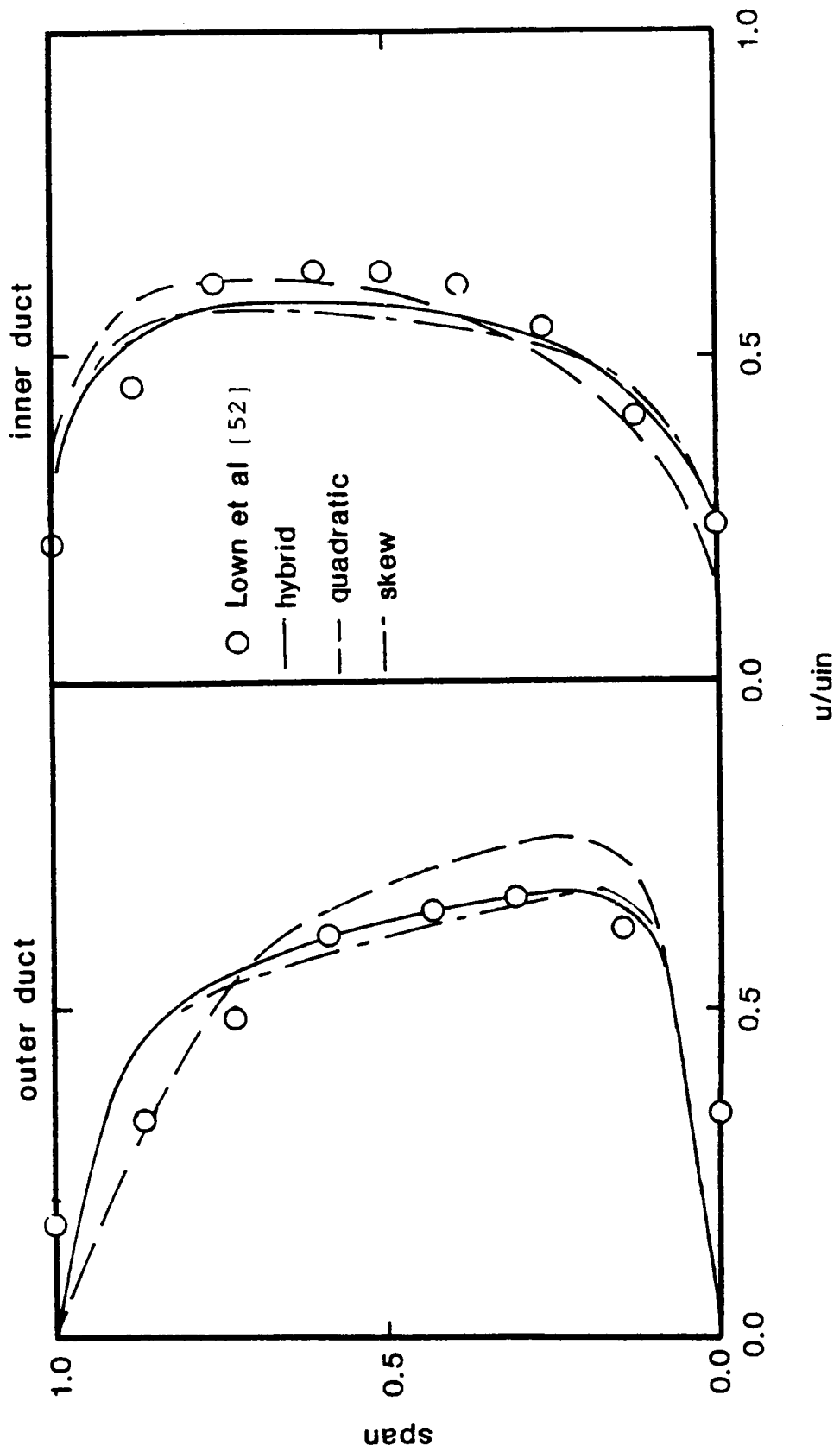
Figure 40. Axial velocity profiles at the outlet of a bifurcated diffuser, computed on a 36x25 mesh
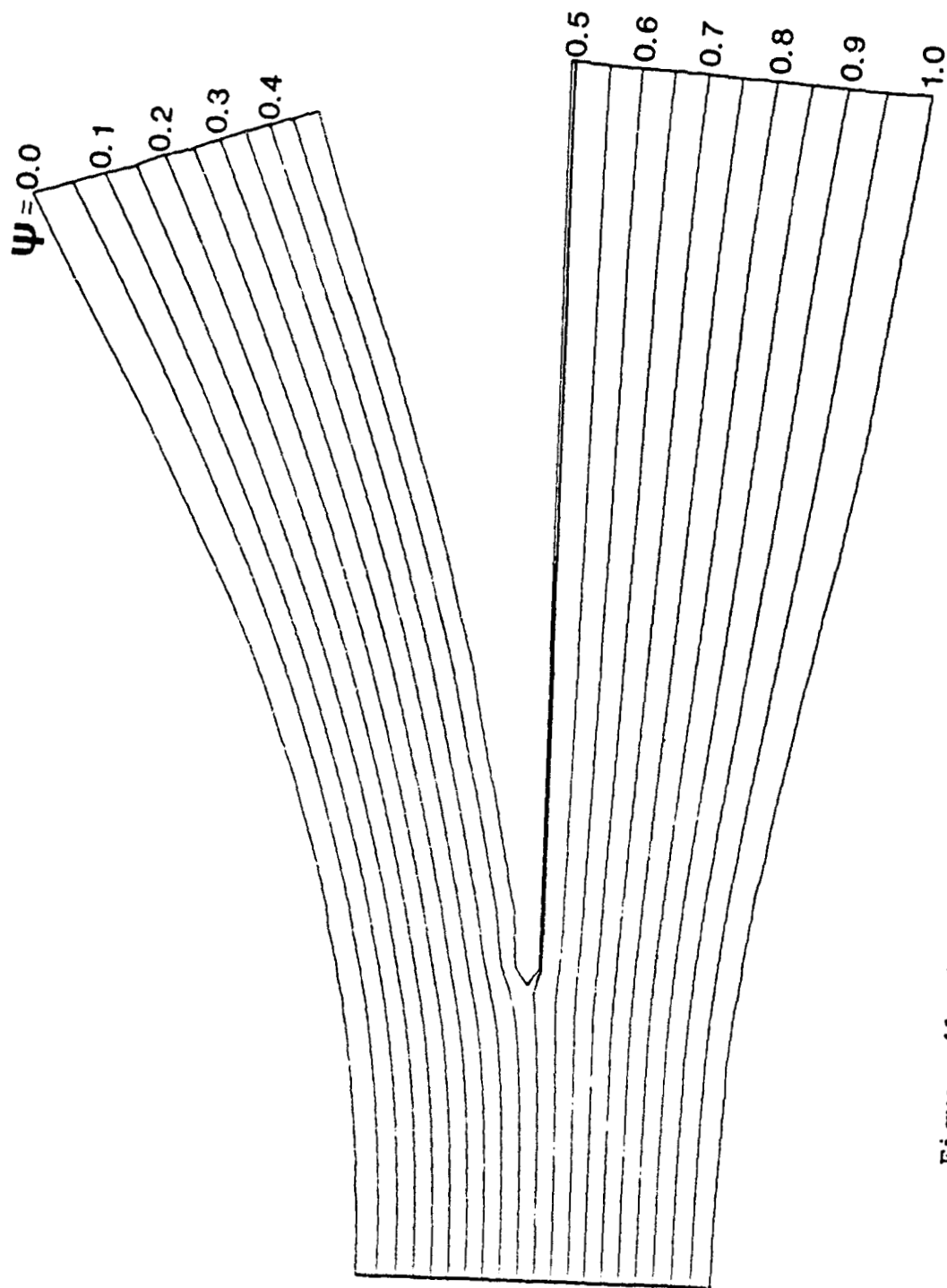
Figure 41. Streamlines of the flow in a bifurcated diffuser
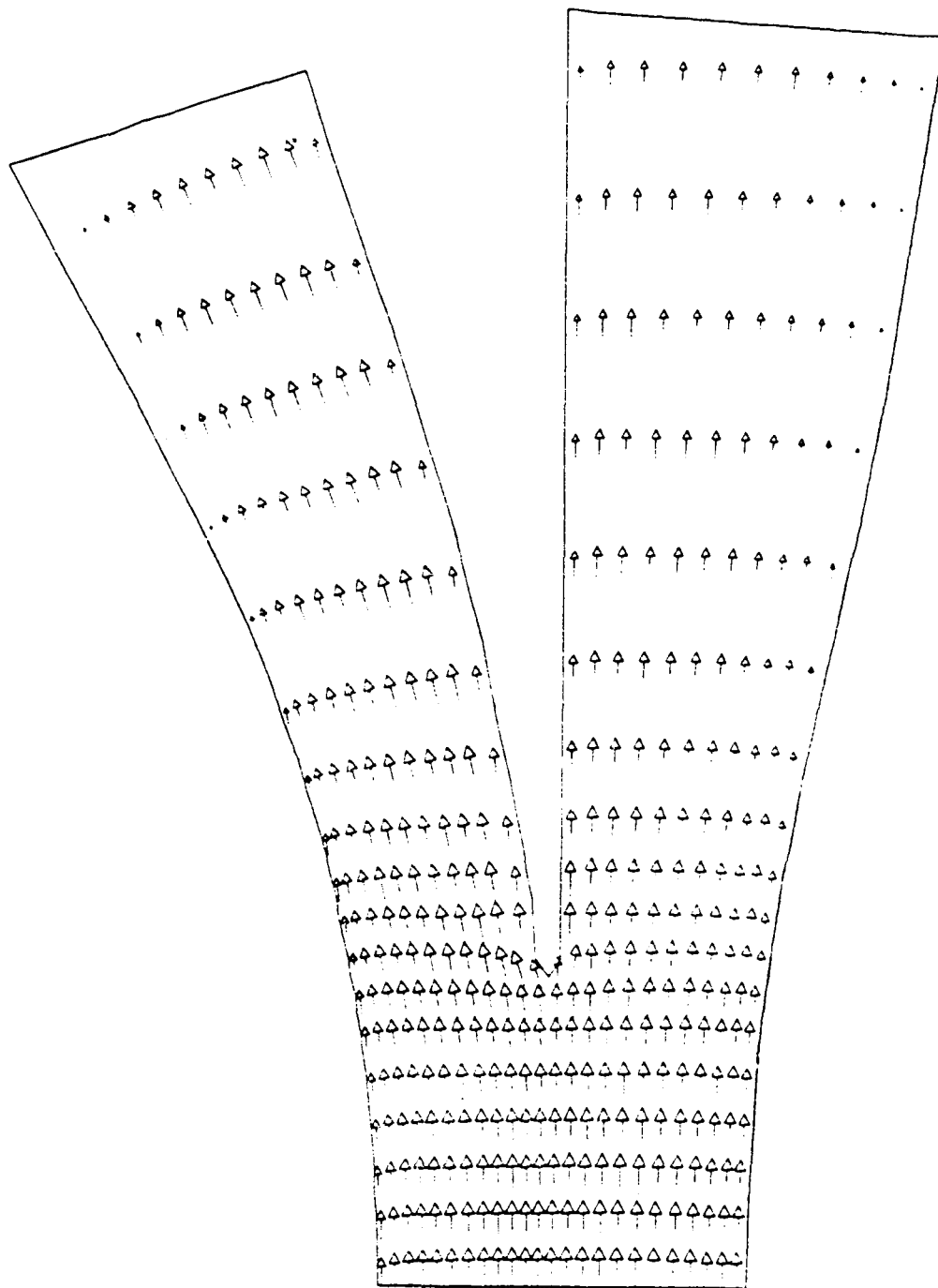
Figure 42. Velocity field for flow in a bifurcated diffuser
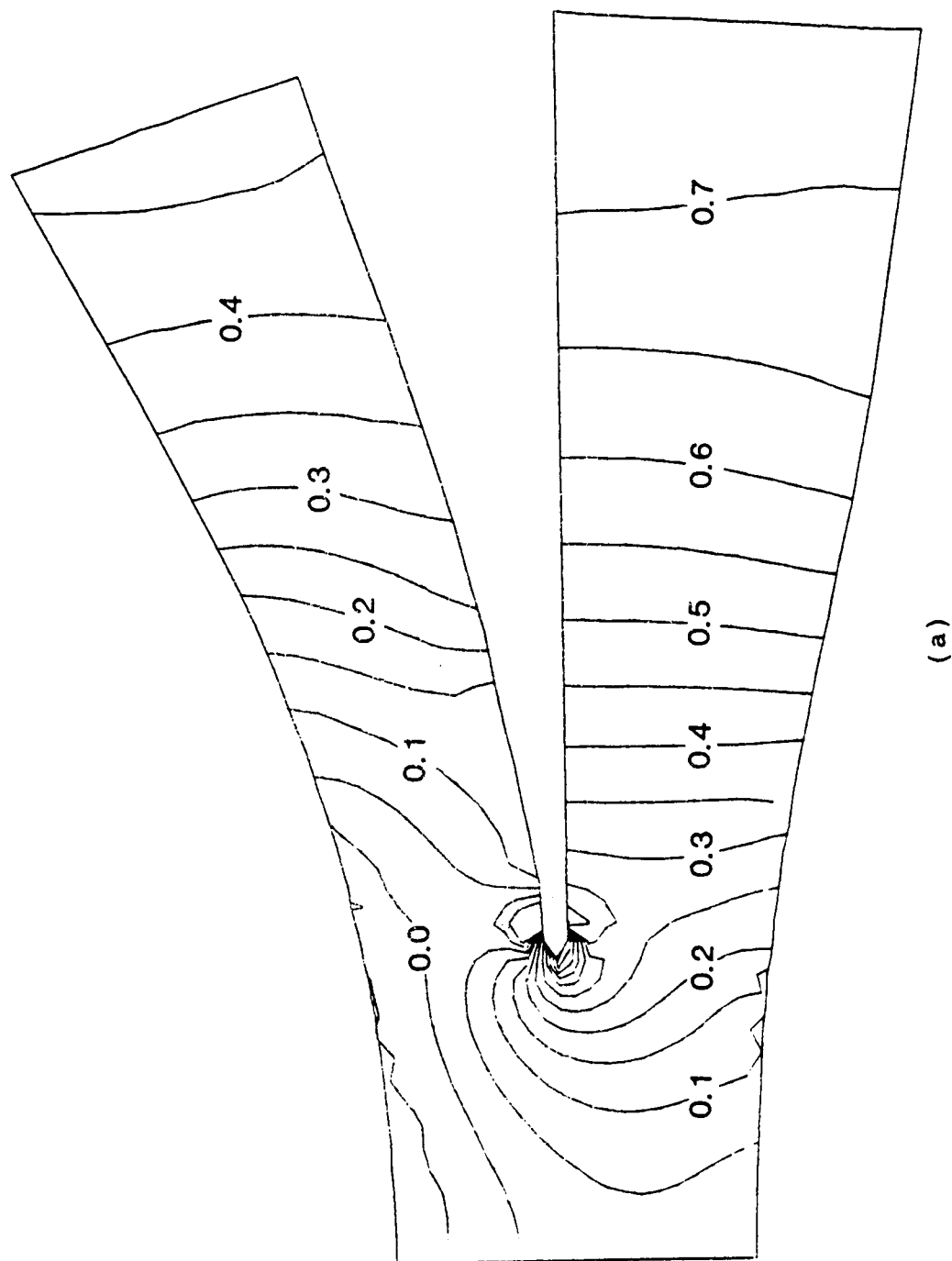
Figure 43. Pressure distribution in a bifurcated diffuser, computed on a 36x25 mesh: (a) hybrid scheme; (b) skew upwind scheme; (c) quadratic upwind scheme

(a)

43(b)

144
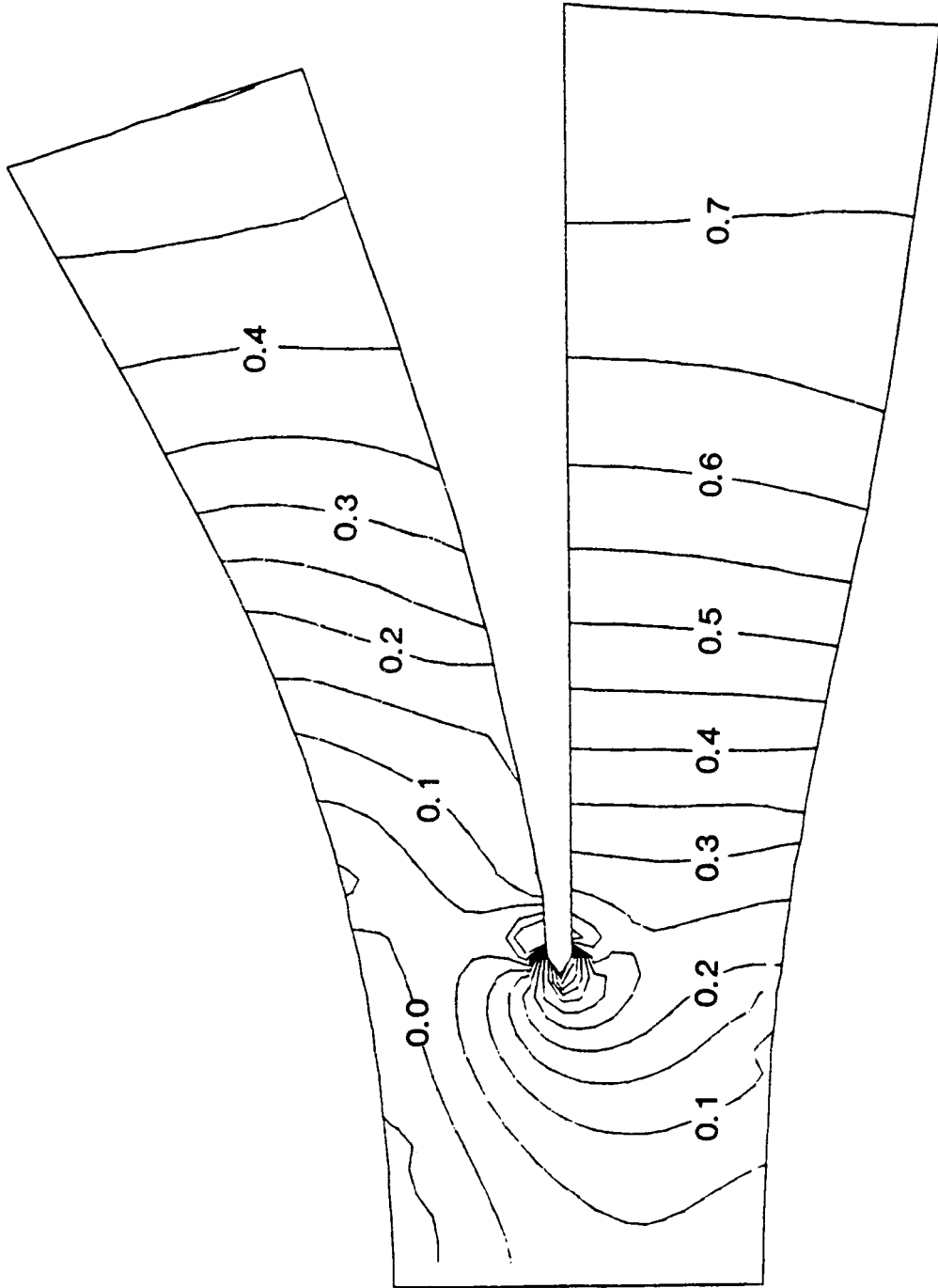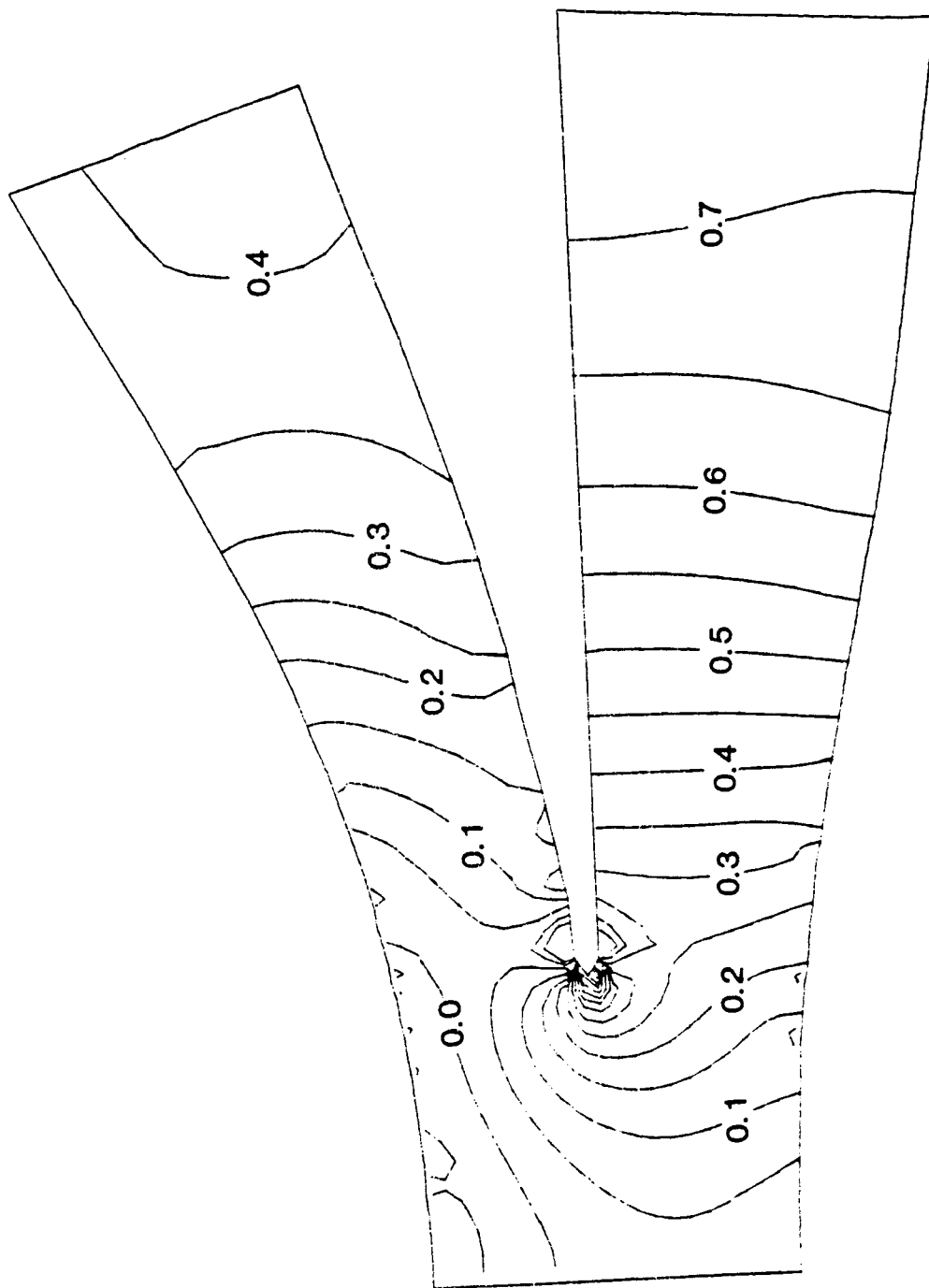
43(c)
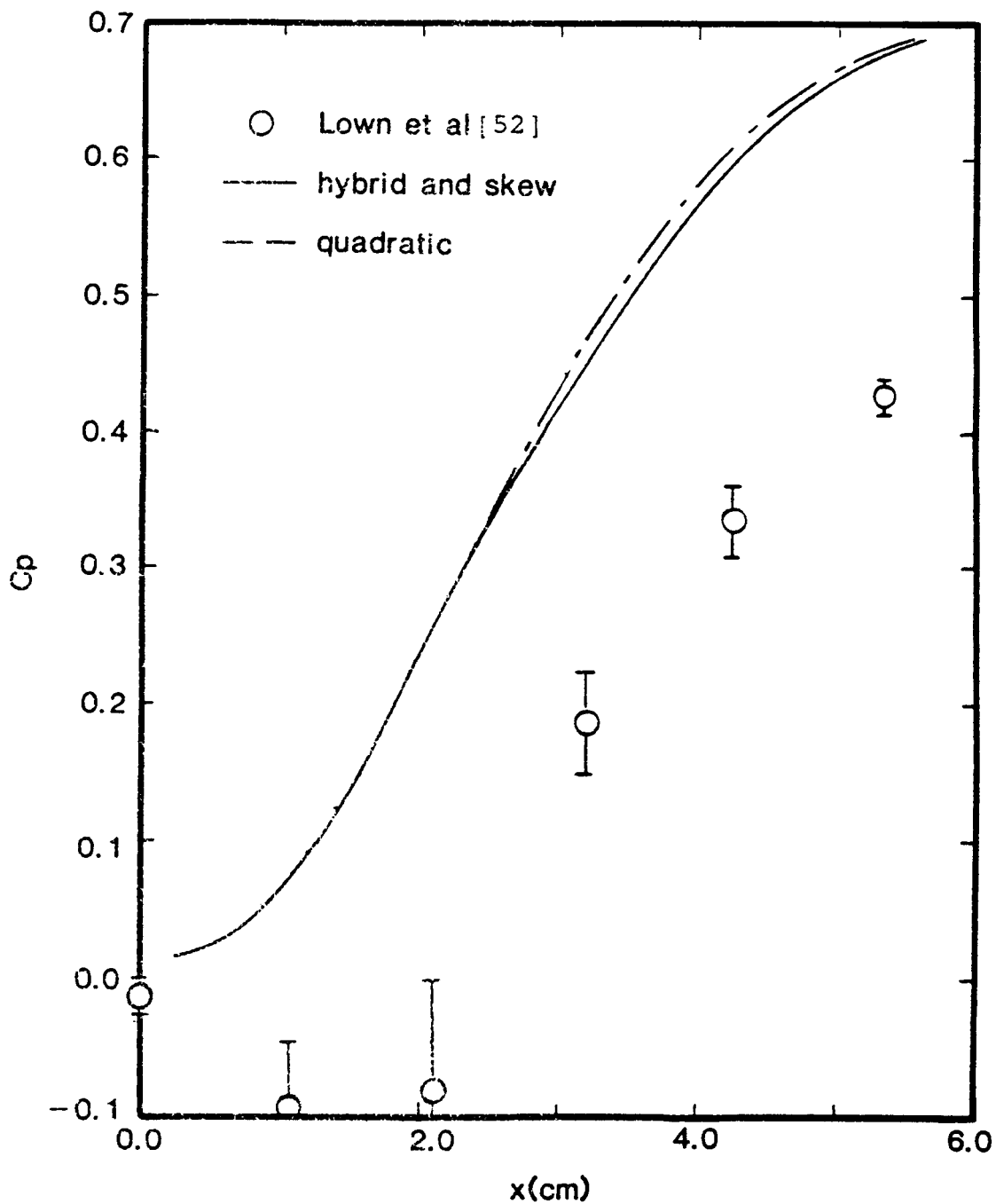
Figure 44. Pressure recovery coefficient along the inner casing of a bifurcated diffuser
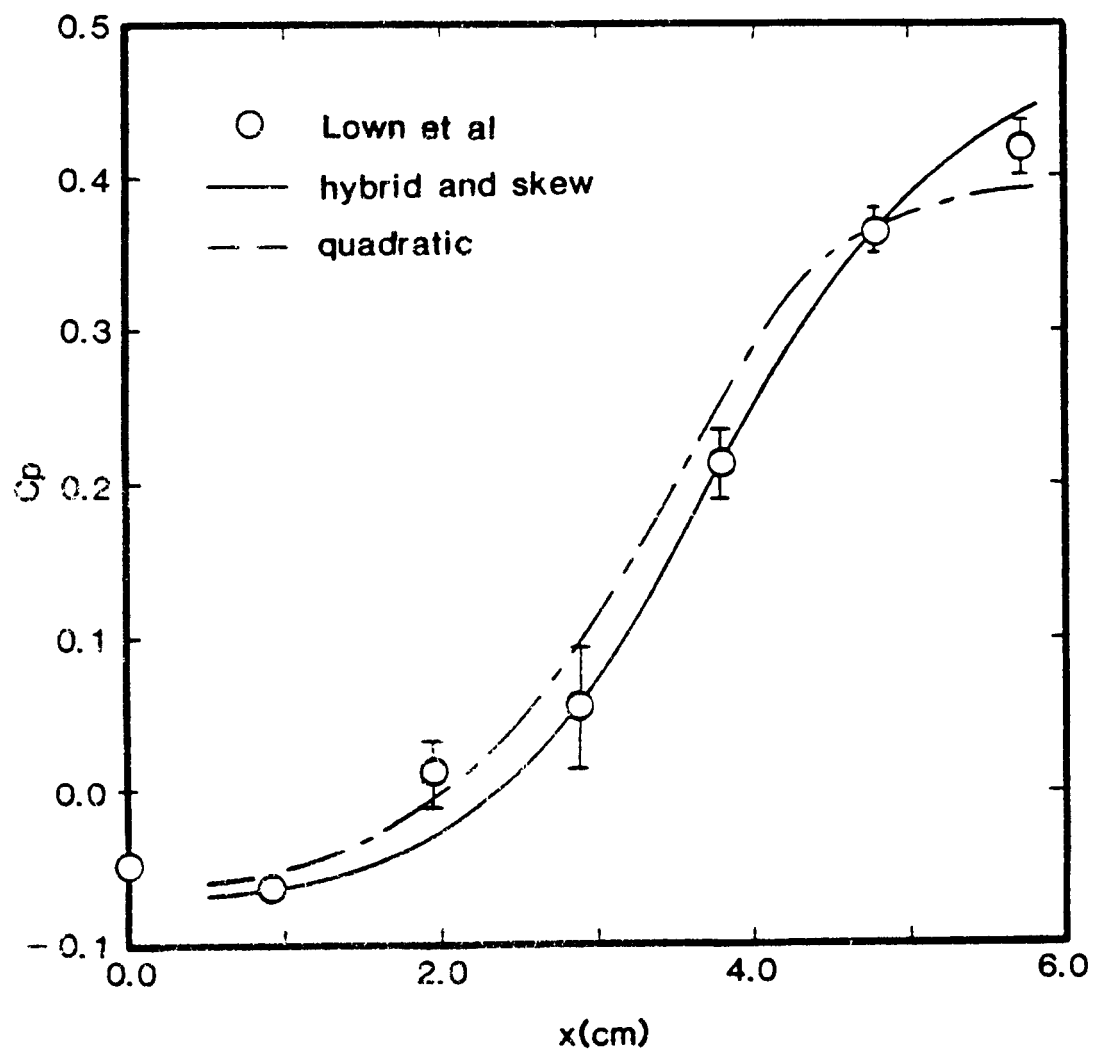
Figure 45. Pressure recovery coefficient along the outer
casing of a bifurcated diffuser

147
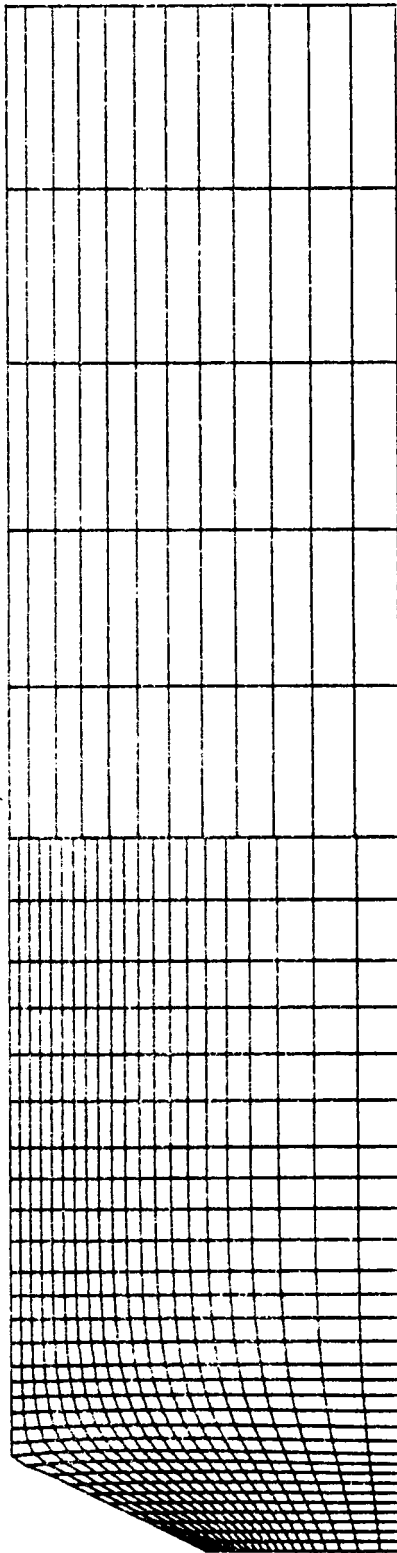
Figure 46. Zonal grid distribution for a 45° expansion combustor, using a 30x30 fine mesh and a 12x5 coarse mesh
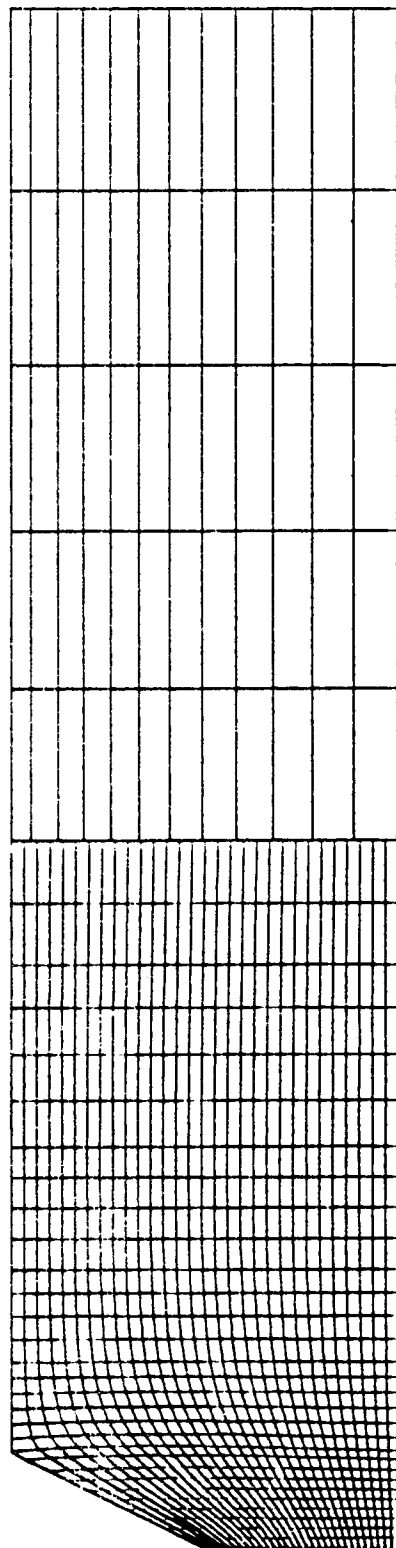
Figure 47. Zonal grid distribution for a 45° expansion combustor, using a 30x21 non-uniform fine mesh and a 12x5 coarse mesh

Figure 48. Axial velocity profiles at various axial locations for flow in a 45° expansion combustor (zoned grid calculation)
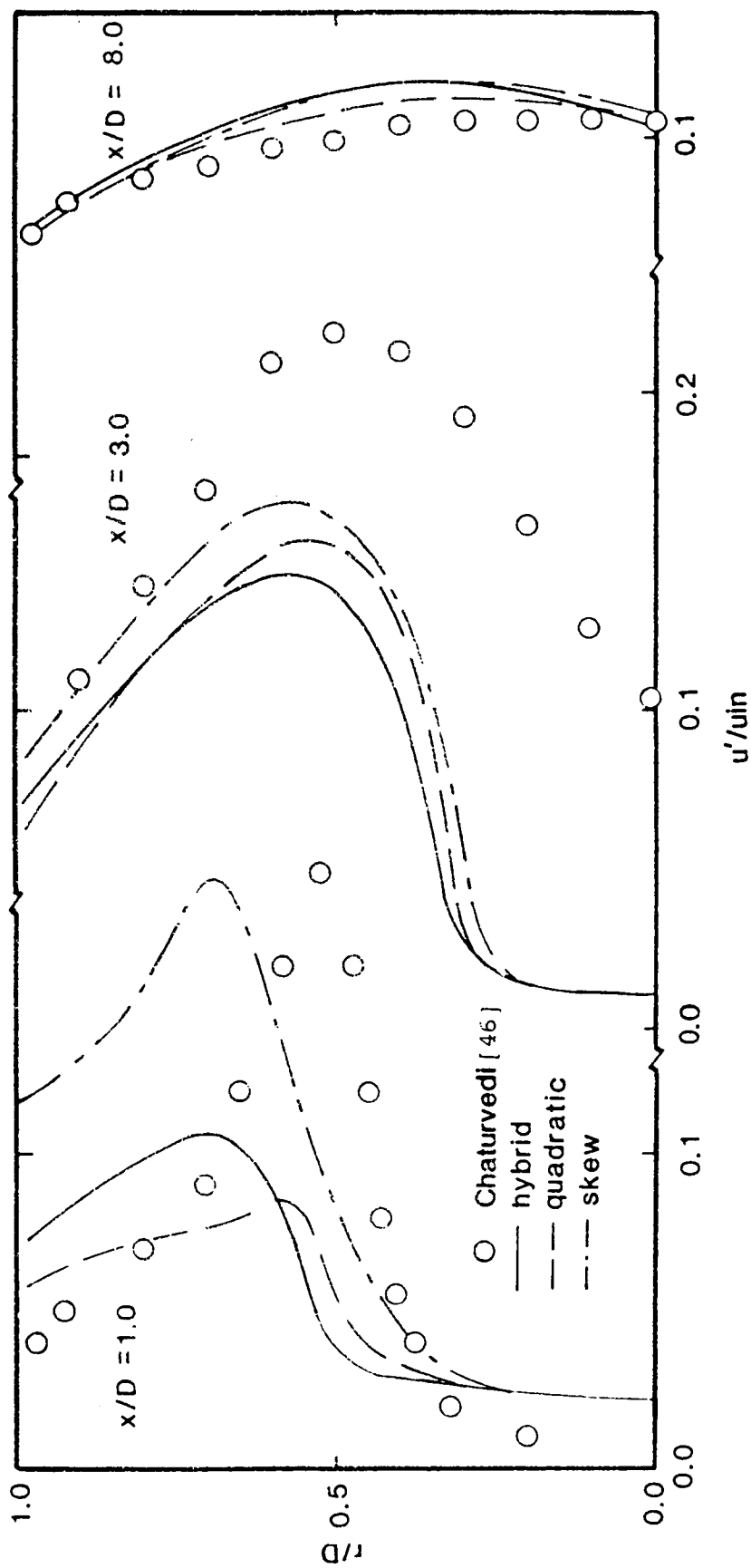
Figure 49. Turbulence intensity distribution at various axial locations for flow in a 45° expansion combustor (zoned grid calculation)
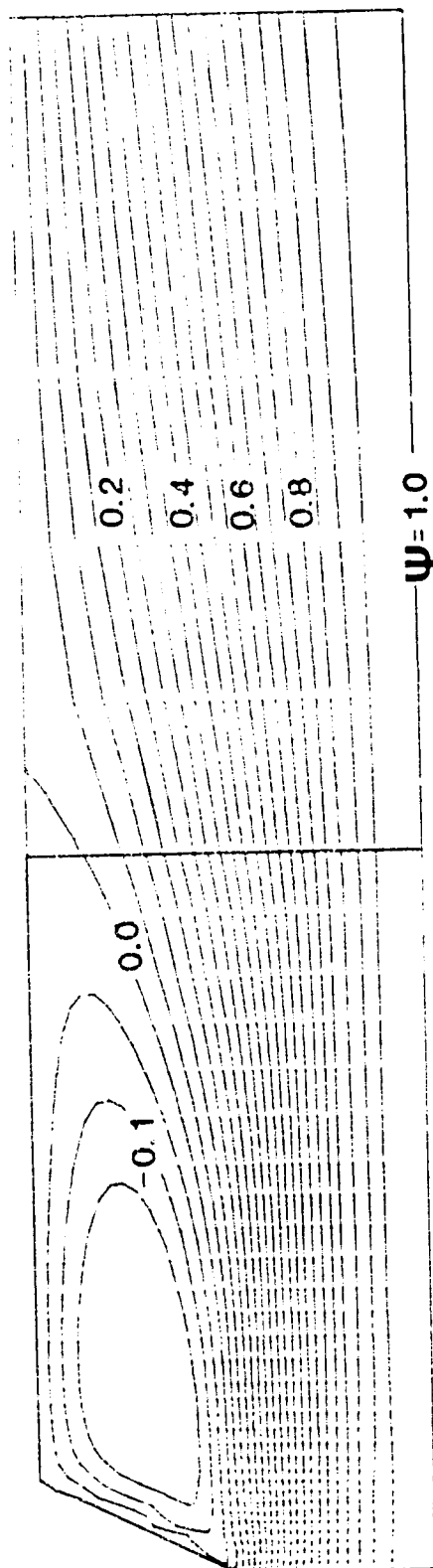
Figure 50. Streamlines of the flow in a 45° expansion combustor (zoned grid calculation)
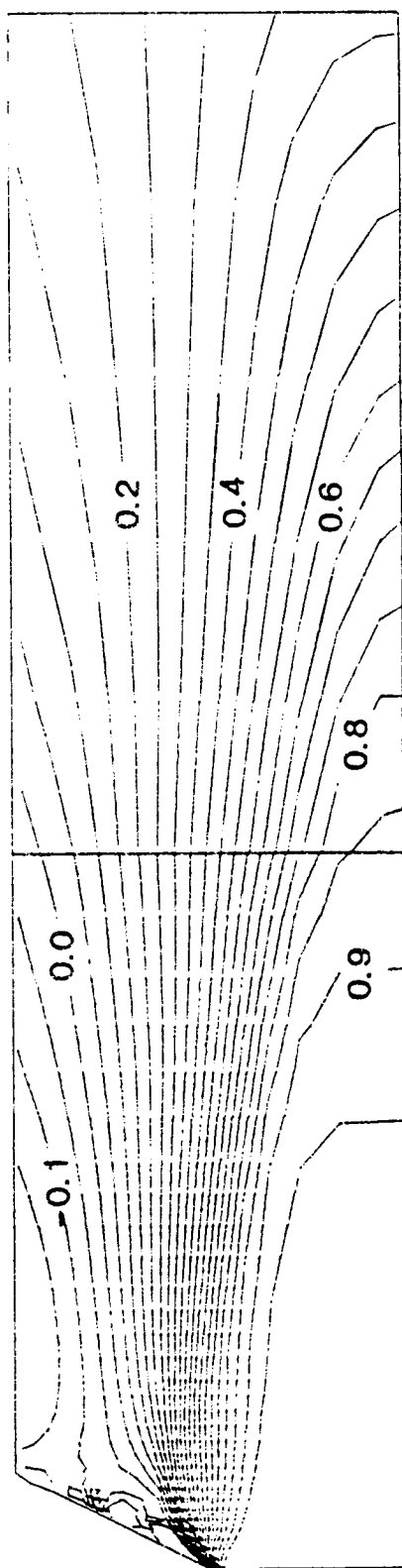
Figure 51. Axial velocity contours for flow in a 45° expansion combustor (zoned grid calculation)
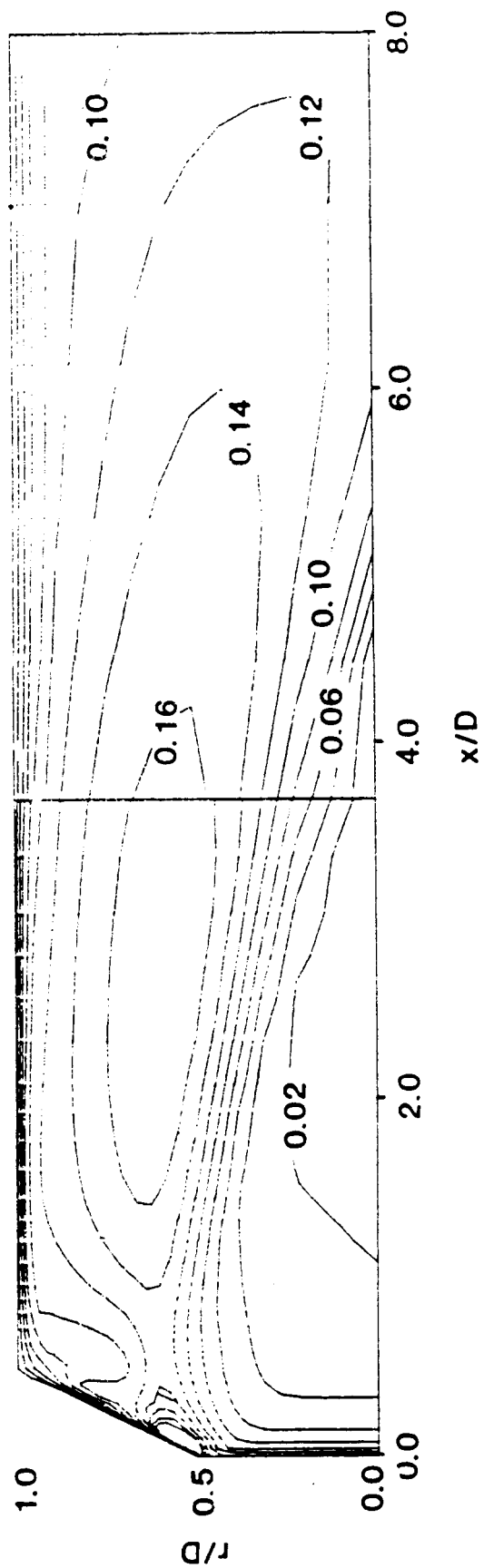
Figure 52. Turbulence intensity contours for flow in a 45°
expansion combustor (zoned grid calculation)
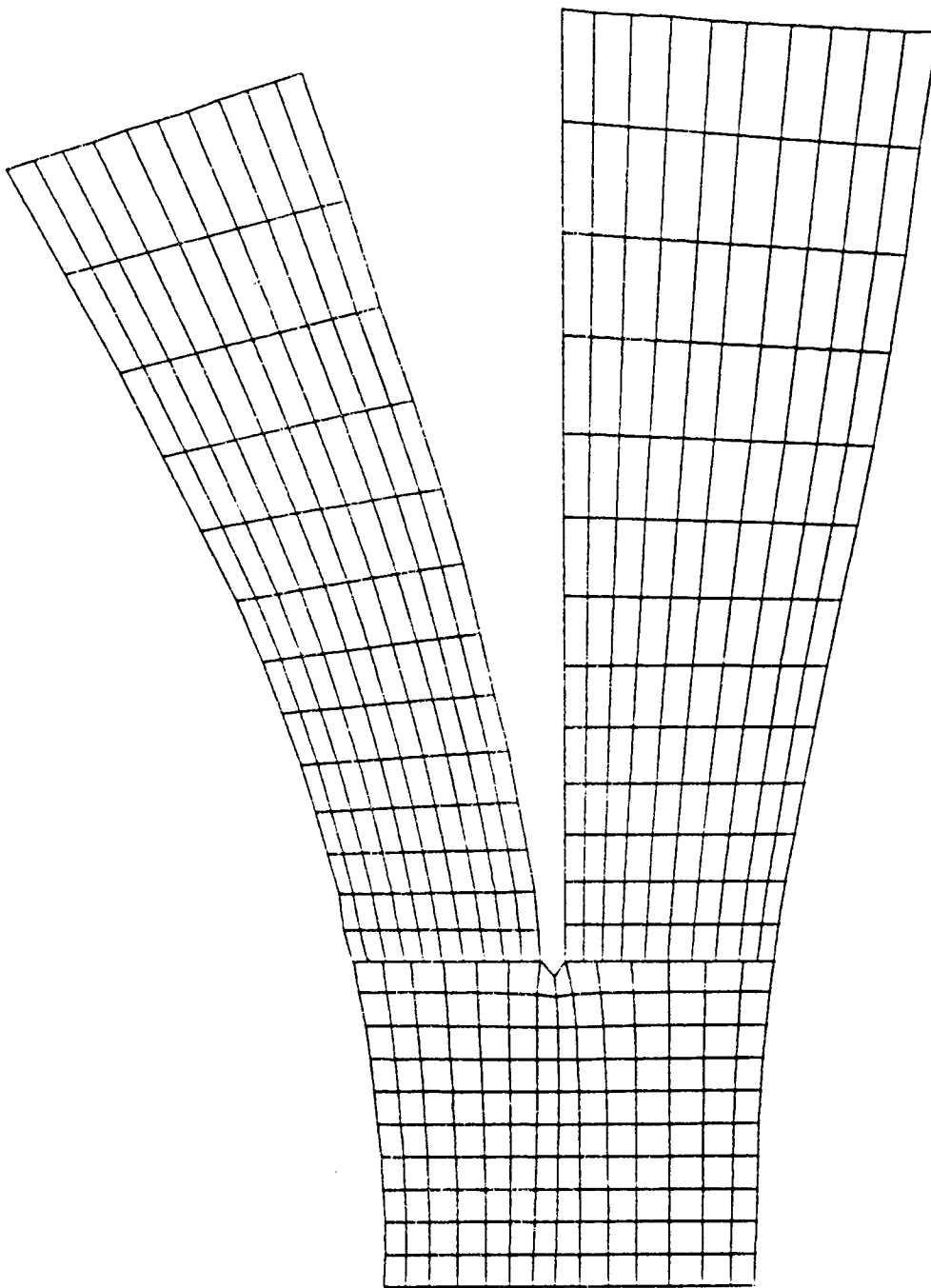
Figure 53. Zoned grid distribution for a bifurcated diffuser: with an 11x15 inlet grid and a 14x11 grid in each of the branches.

155
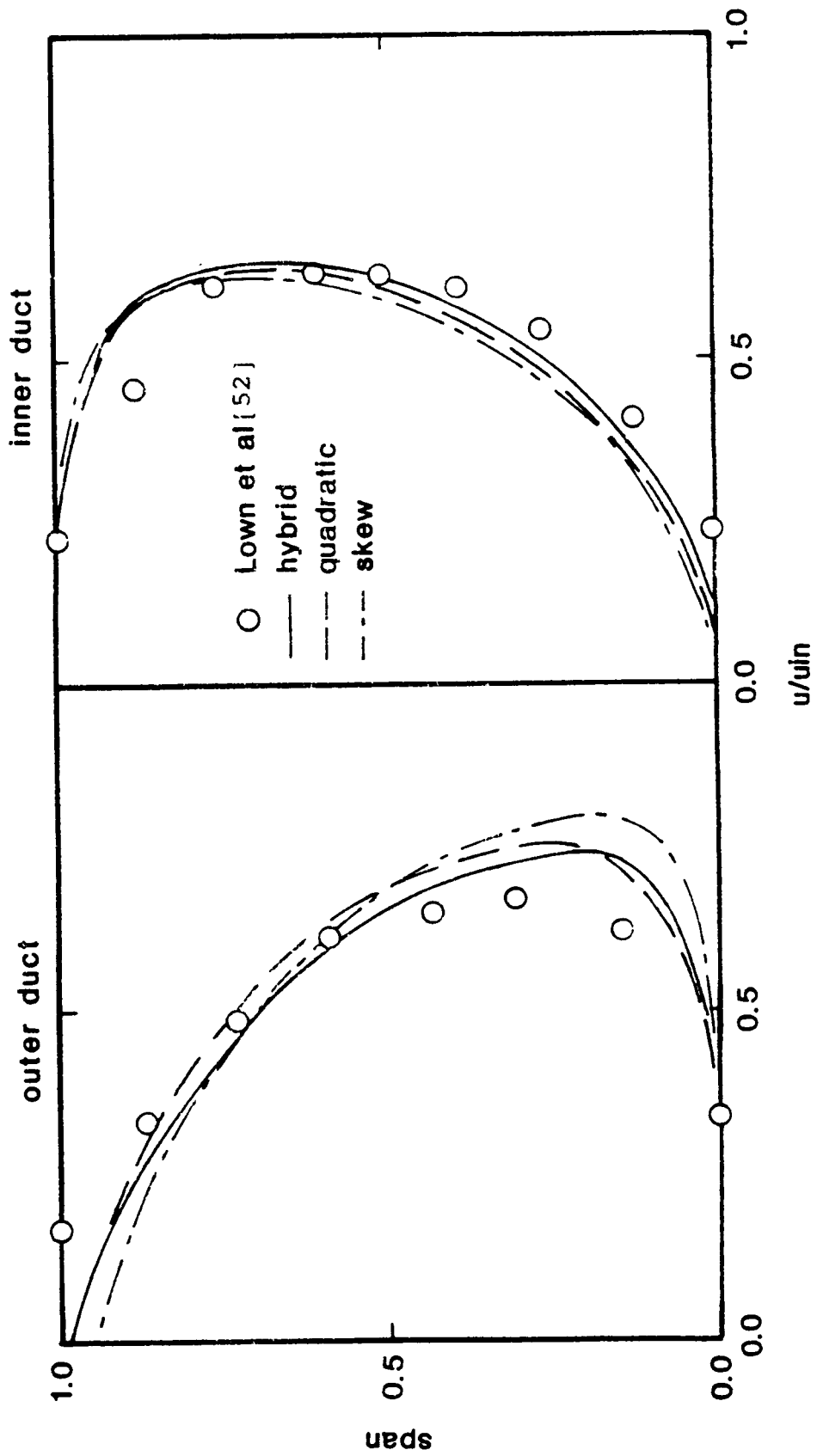
Figure 54. Velocity profiles at the outlet of a bifurcated diffuser, computed on a coarse zoned grid

Figure 55. Velocity profiles at the outlet of a bifurcated diffuser, computed on a fine zoned grid
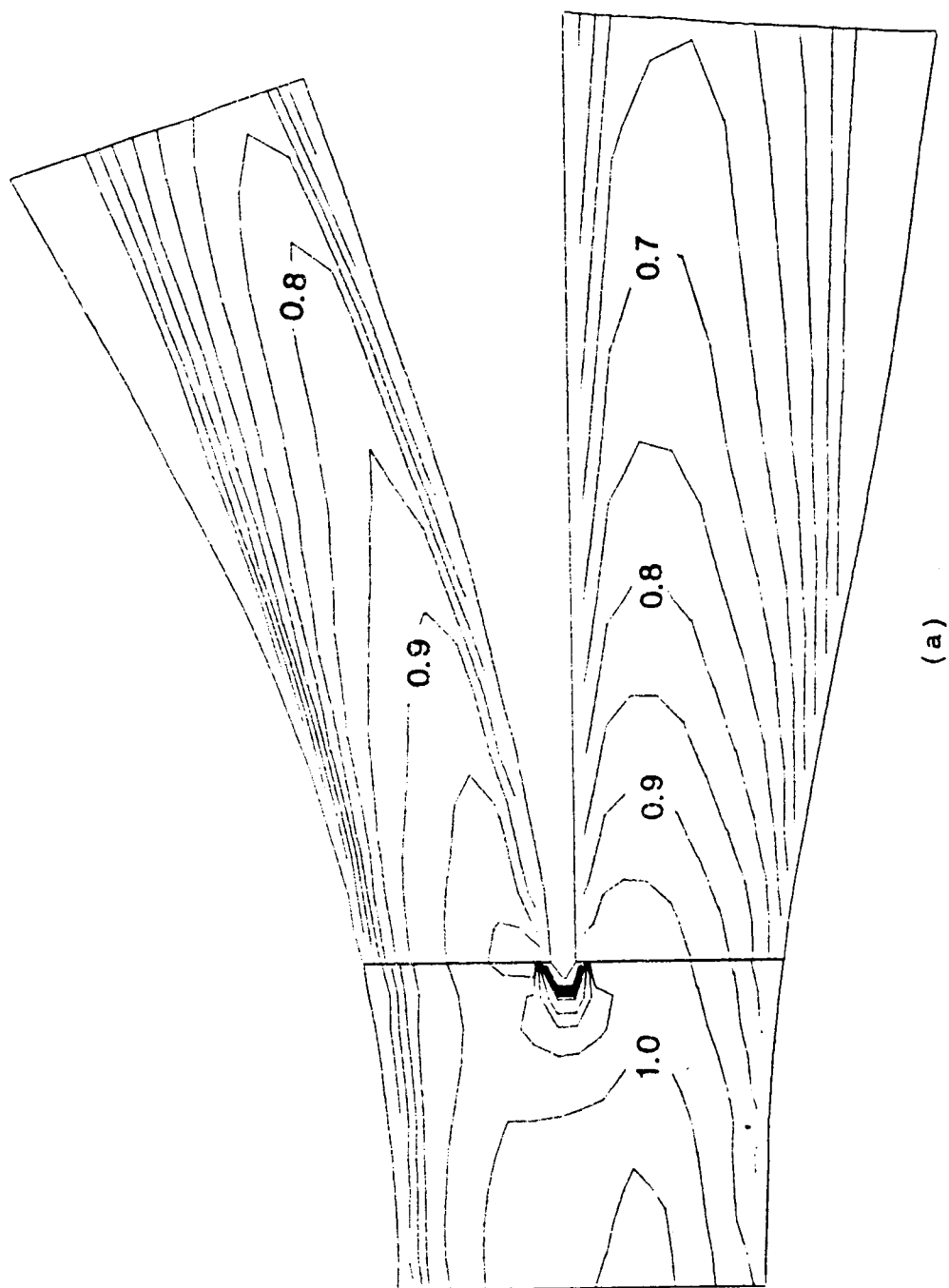
Figure 56. Velocity contours for flow in a bifurcated diffuser, computed on a coarse zoned grid: (a) hybrid scheme; (b) skew upwind scheme; (c) quadratic upwind scheme
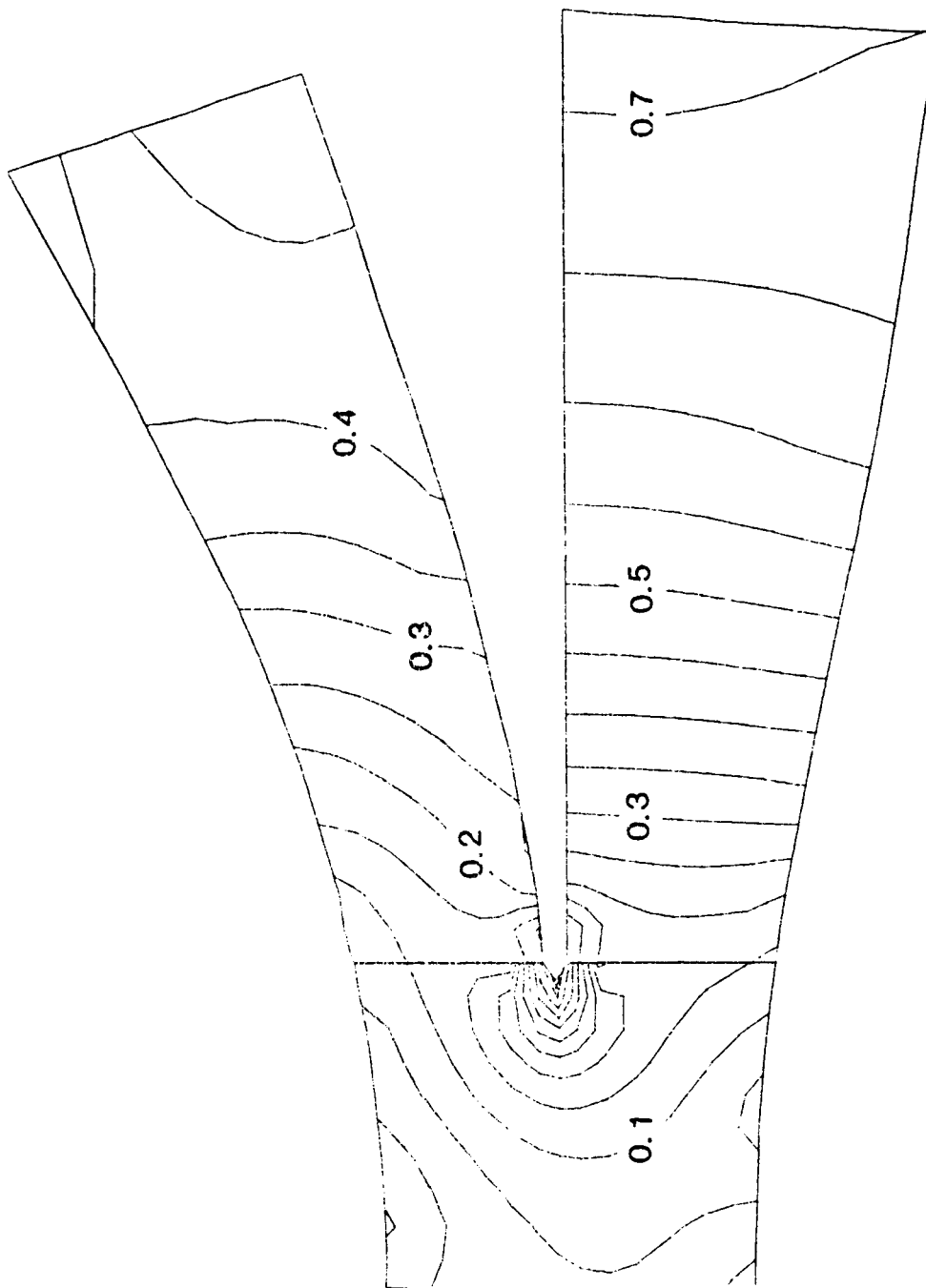
(a)
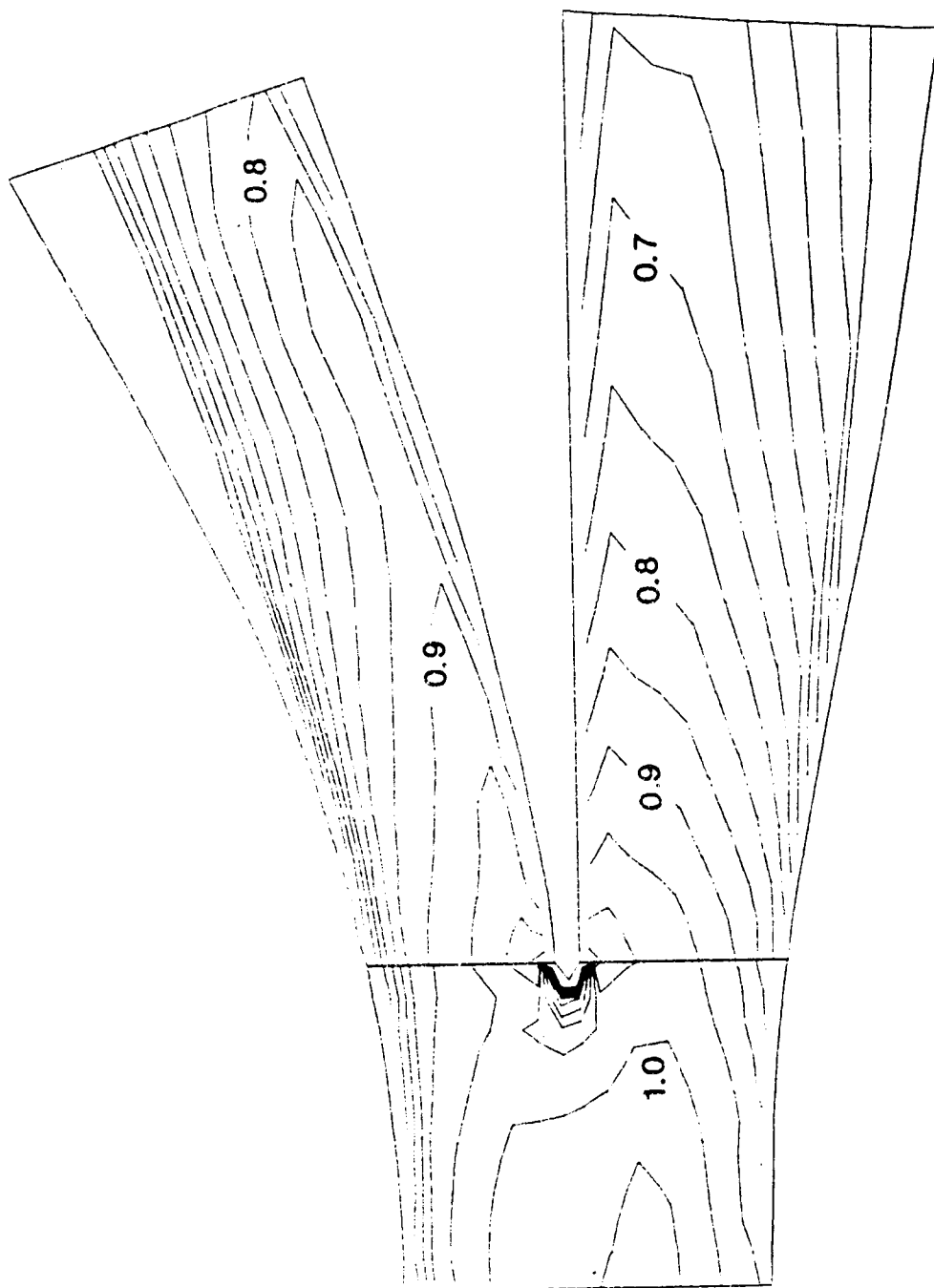
56(b)
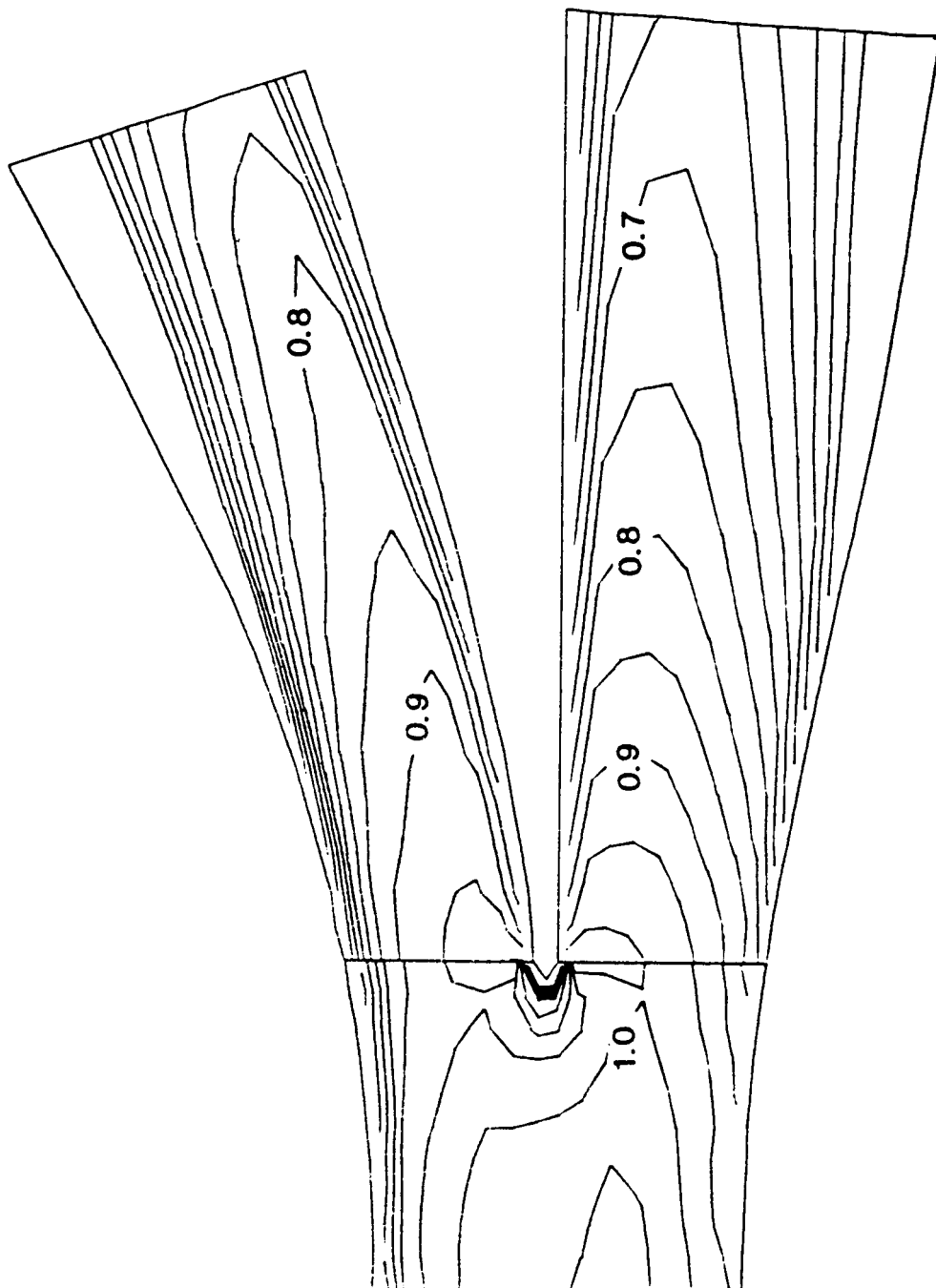
56(c)
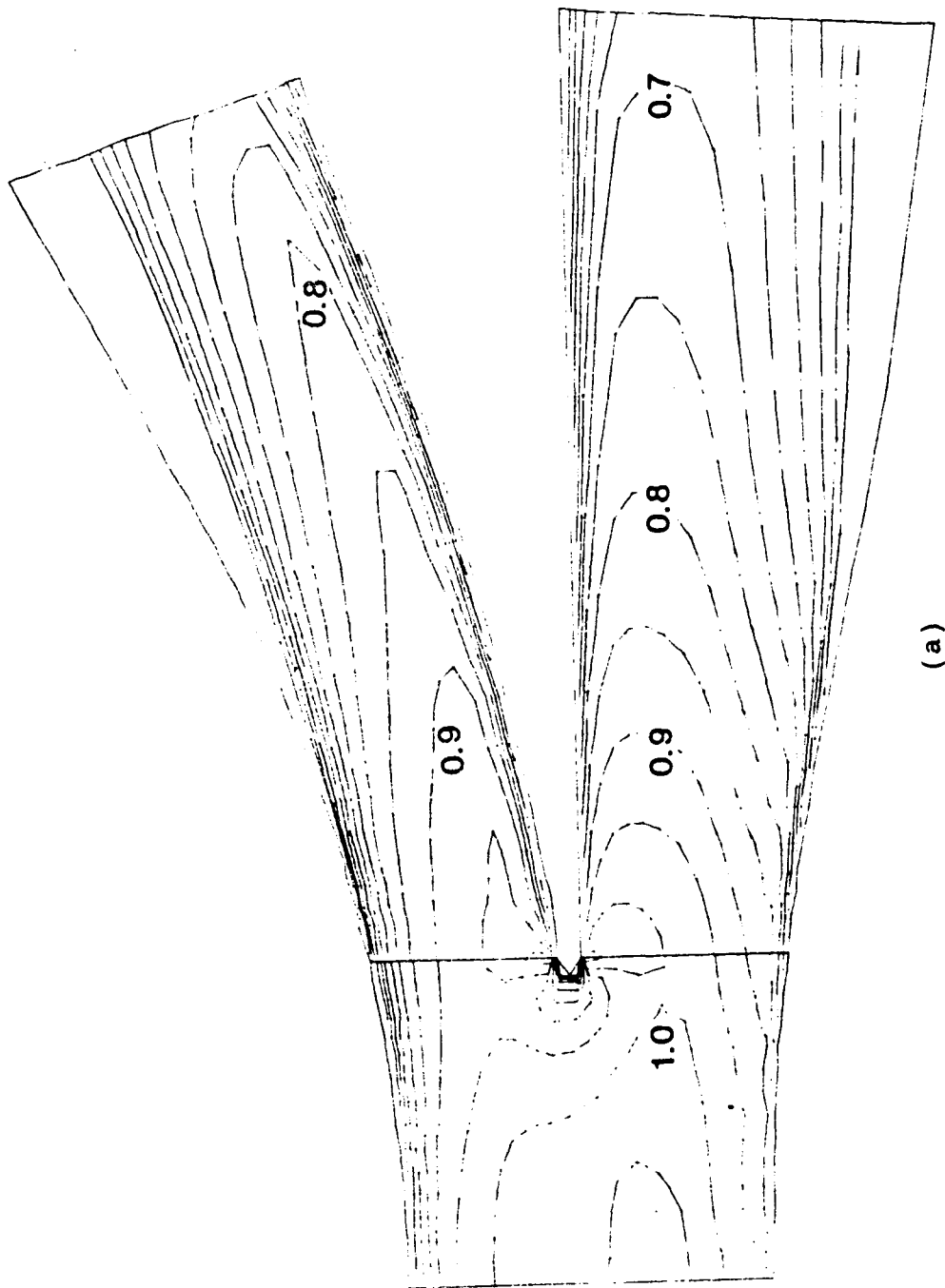
Figure 57. Velocity contours for flow in a bifurcated diffuser, computed on a fine zoned grid: (a) hybrid scheme; (b) skew upwind scheme; (c) quadratic upwind scheme
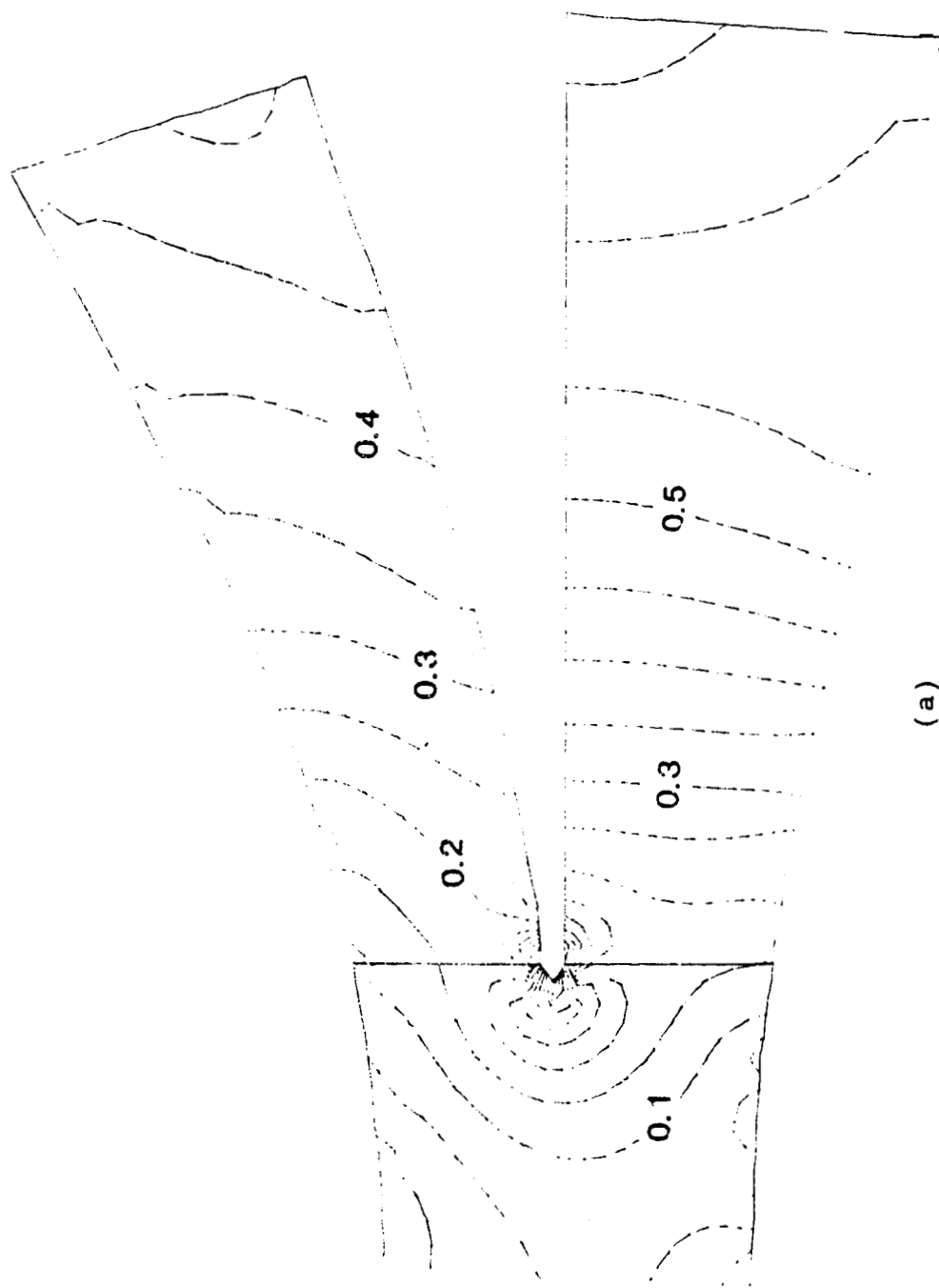
(a)
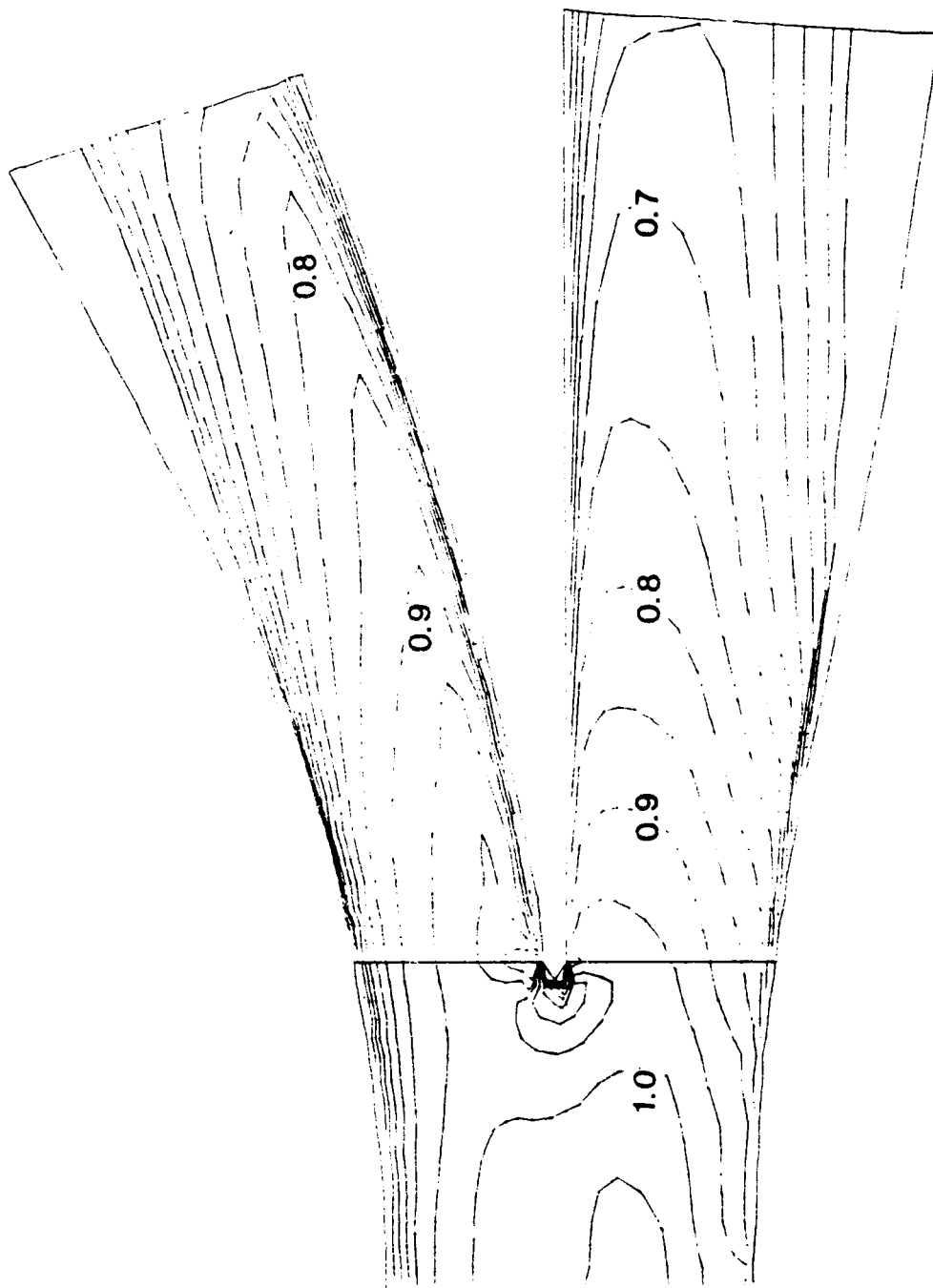
57(b)
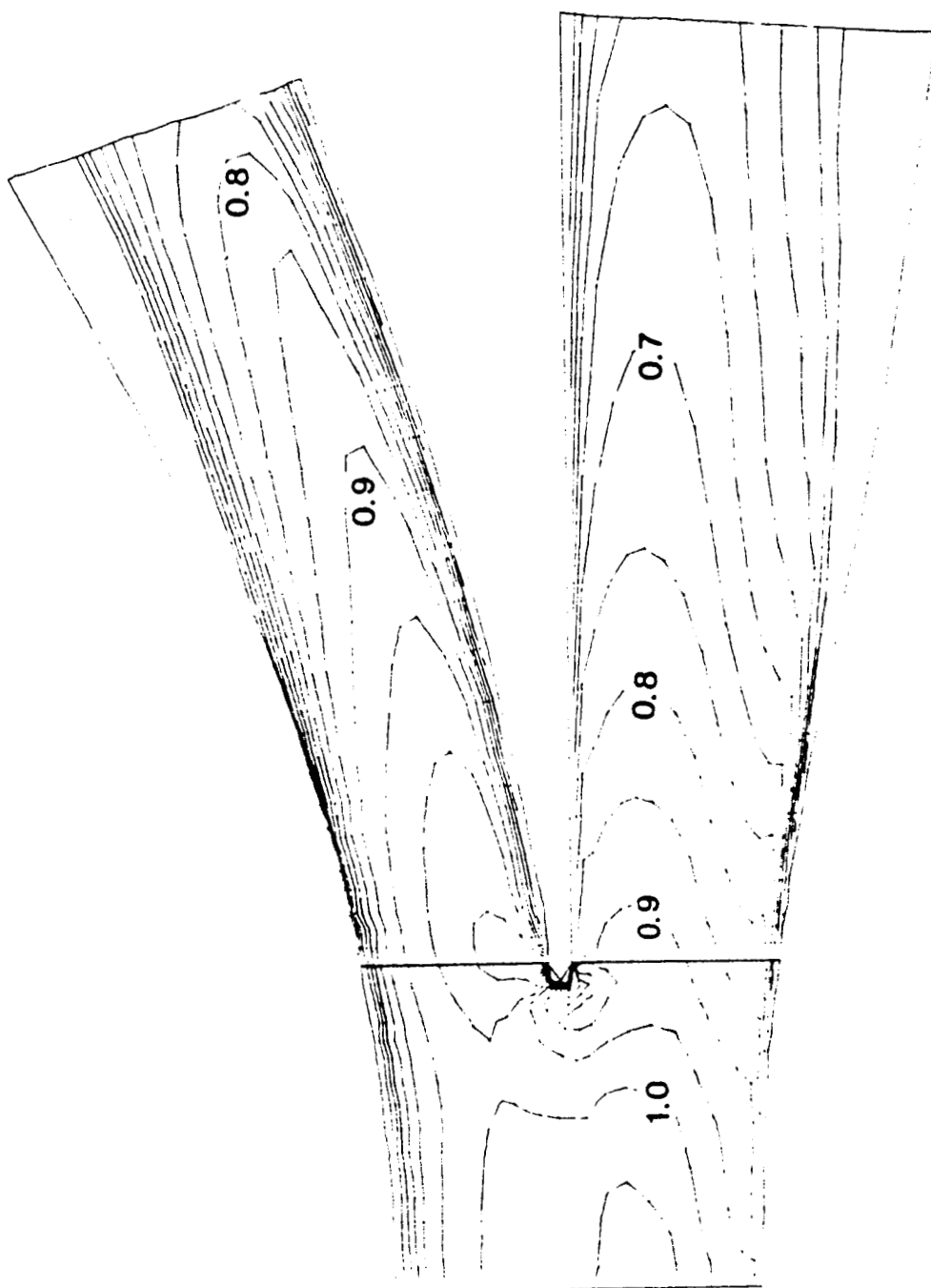
57(c)
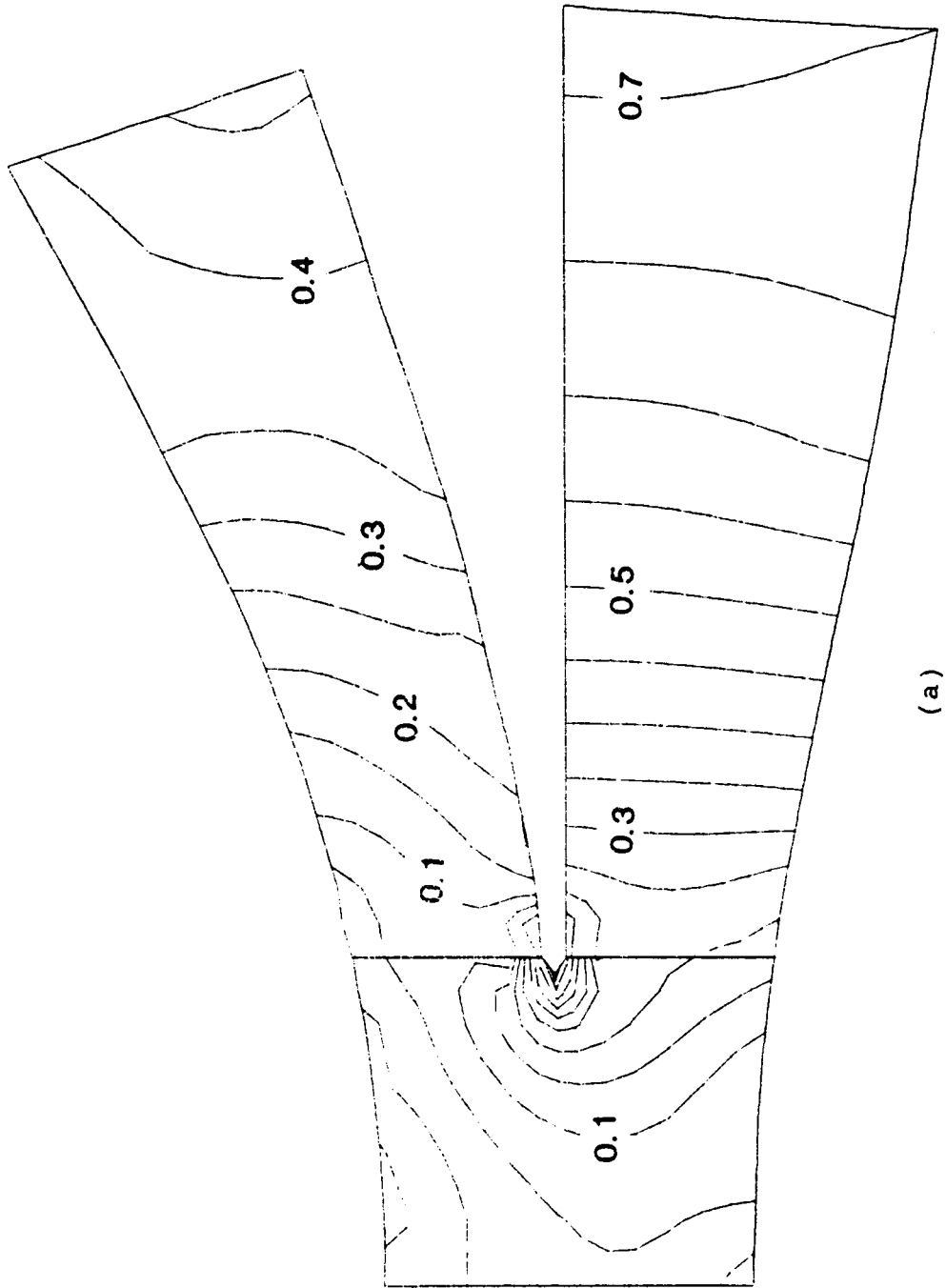
Figure 58. Pressure distribution in a bifurcated diffuser, computed on a coarse zoned grid: (a) hybrid scheme; (b) skew upwind scheme; (c) quadratic upwind scheme
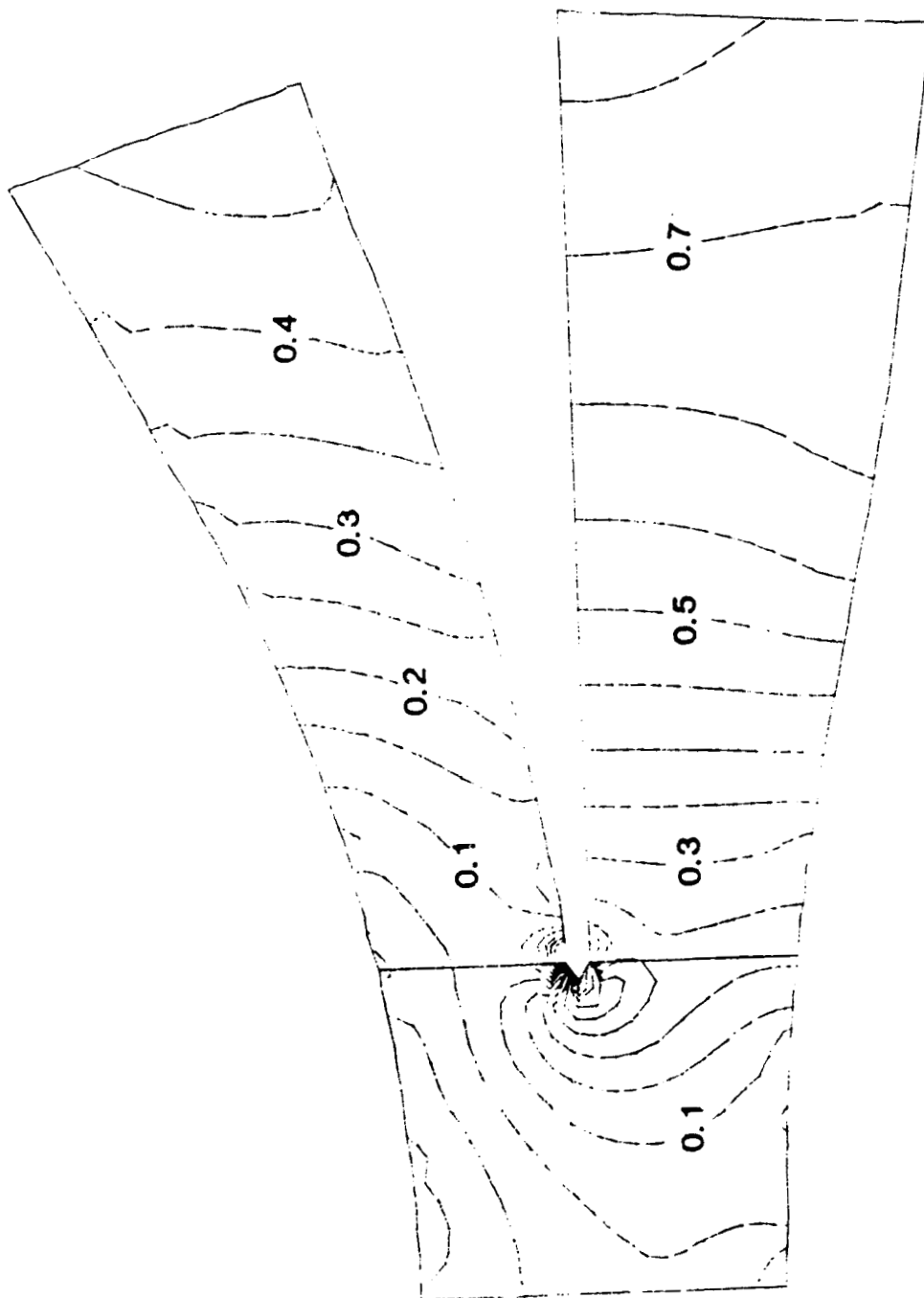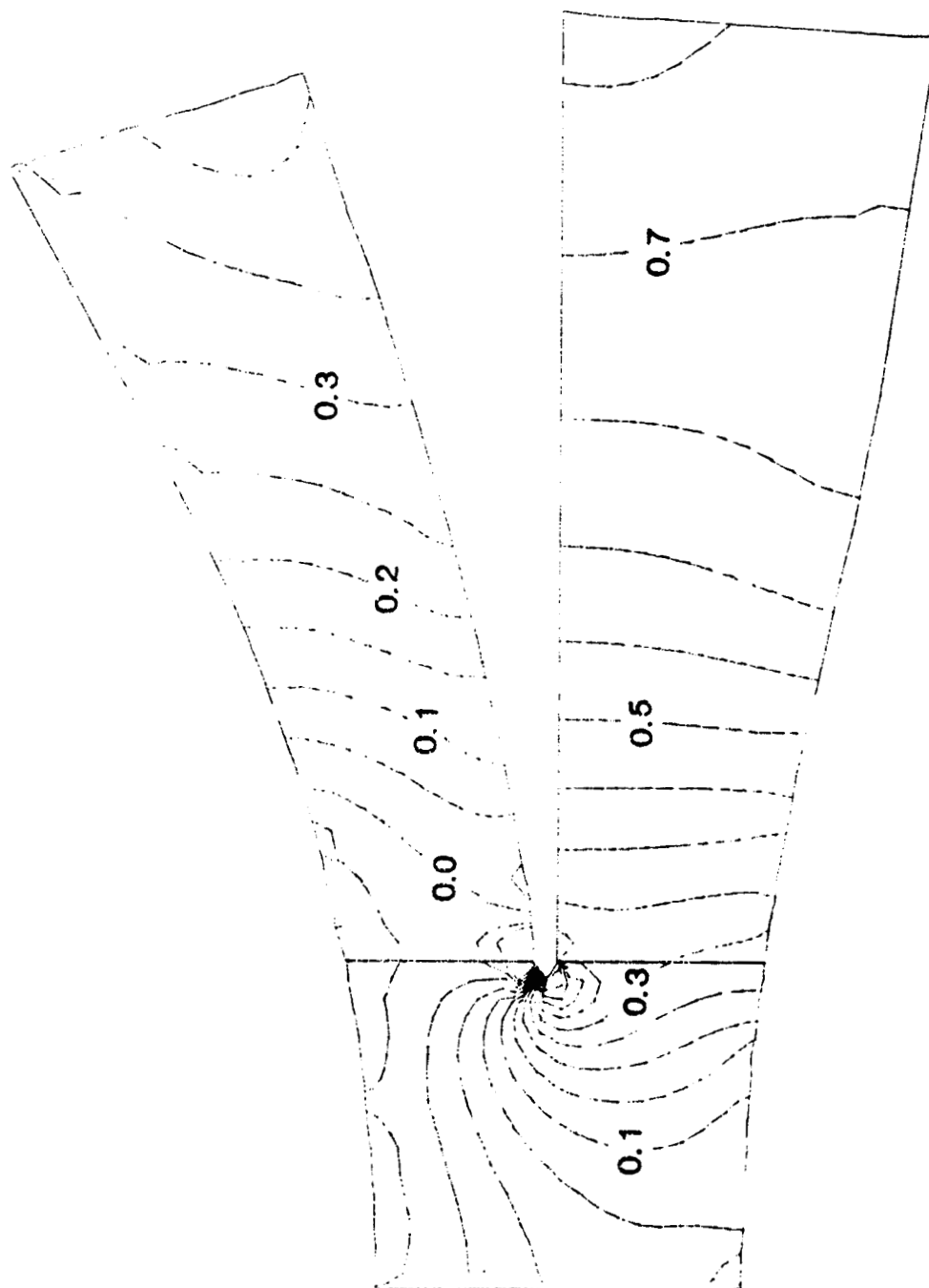
(a)

58(b)

58(c)
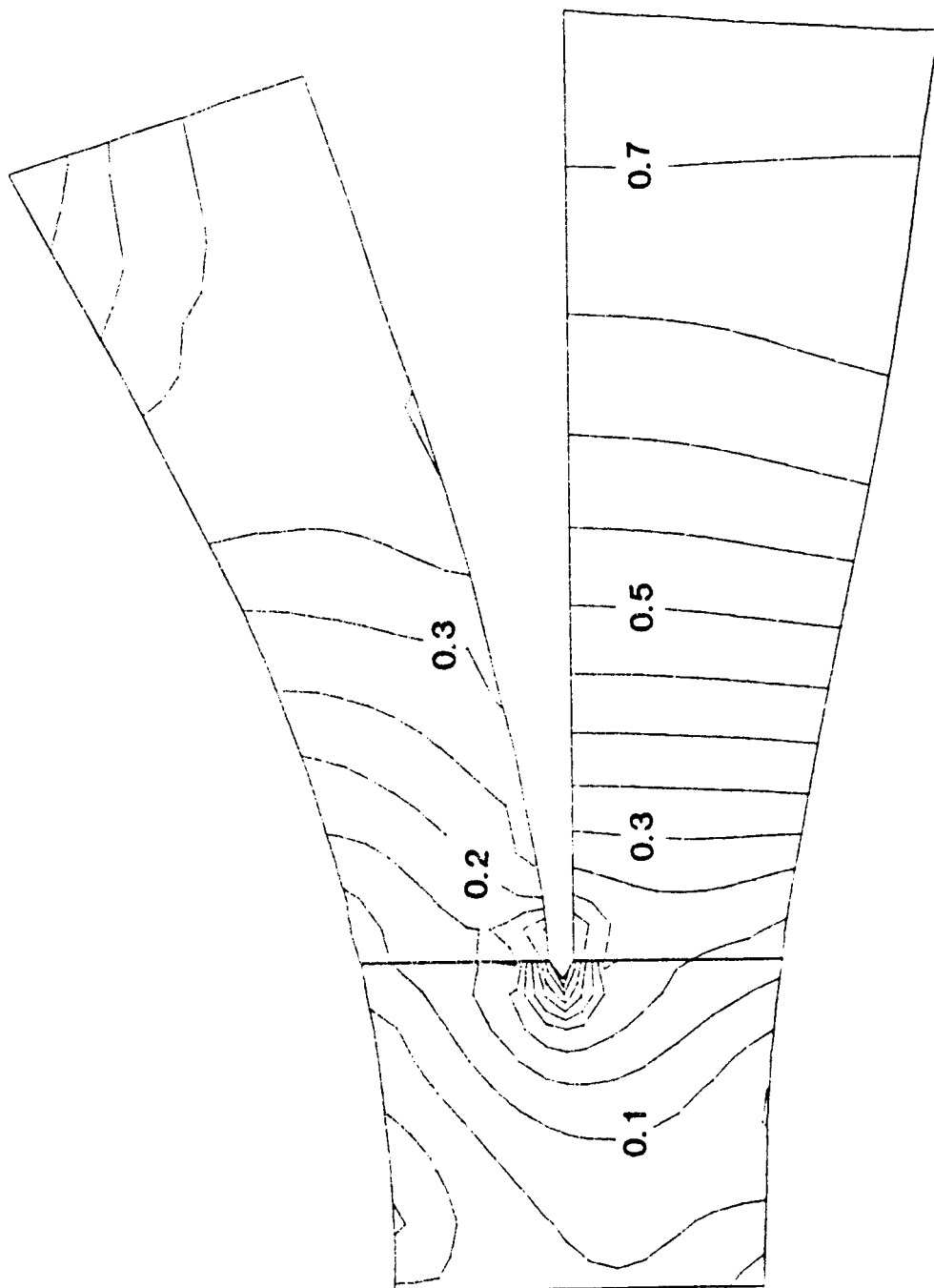
Figure 59. Pressure distribution in a bifurcated diffuser, computed on a fine zoned grid: (a) hybrid scheme; (b) skew upwind scheme; (c) quadratic upwind scheme

59(b)

168

59(c)

169

Report Documentation Page

1. Report No. NASA CR-4115	2. Government Accession No.	3. Recipient's Catalog No.
4. Title and Subtitle Numerical Simulation of Axisymmetric Turbulent Flow in Combustors and Diffusers		5. Report Date February 1988
		6. Performing Organization Code
7. Author(s) Chain Nan Yung		8. Performing Organization Report No. None (E-3853)
		10. Work Unit No. 505-62-21
9. Performing Organization Name and Address University of Toledo College of Engineering Toledo, Ohio 43606		11. Contract or Grant No. NAG3-355
12. Sponsoring Agency Name and Address National Aeronautics and Space Administration Lewis Research Center Cleveland, Ohio 44135-3191		13. Type of Report and Period Covered Contractor Report Final
		14. Sponsoring Agency Code

16. Abstract
    The purpose of this research was to develop a method for predicting turbulent flow in combustors and diffusers. The Navier-Stokes equations, incorporating a turbulence k-ε model equation, were solved in a nonorthogonal curvilinear coordinate system. The solution procedure applied the finite volume method to discretize the differential equations and utilized the SIMPLE algorithm iteratively to solve the differenced equations. A zonal grid method, wherein the flow field was divided into several subsections, was developed. This approach permited different computational schemes to be used in the various zones. In addition, grid generation was made a more simple task. However, treatment of the zonal boundaries required special handling. Boundary overlap and interpolating techniques were used and an adjustment of the flow variables was required to assure conservation of mass, momentum and energy fluxes. The numerical accuracy was assessed using different finite differencing methods, i.e., hybrid, quadratic upwind and skew upwind, to represent the convection terms. Flows in different geometries of combustors and diffusers were simulated and the results were compared with existing experimental data. In general, good agreement between predicted and measured values was obtained.

17. Key Words (Suggested by Author(s)) Diffuser, Teach code, Grid patching, Grid generation, Combustors, Computational fluid dynamics	18. Distribution Statement Unclassified - Unlimited Subject Category 02		
19. Security Classif. (of this report) Unclassified	20. Security Classif. (of this page) Unclassified	21. No of pages 176	22. Price* A09